

AD-A256 742

2

AFWAL-TR-85-3019



THE CHARACTERIZATION OF  
BORON/ALUMINUM COMPOSITE  
AS AN ORTHOTROPIC  
ELASTIC-PLASTIC MATERIAL

C. T. Sun, J. F. Doyle and D. Kenaga  
School of Aeronautics and Astronautics  
Purdue University  
West Lafayette, IN 47907

DTIC  
ELECTE  
OCT 20 1992  
S A D

June 1985

Interim Report for June 1982 to June 1985

Approved for public release; distribution unlimited

FLIGHT DYNAMICS LABORATORY  
AIR FORCE WRIGHT AERONAUTICAL LABORATORIES  
AIR FORCE SYSTEMS COMMAND  
WRIGHT-PATTERSON AIR FORCE BASE, OHIO 45433

291850

92-27451



11098

## NOTICE

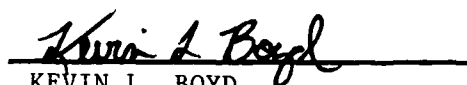
WHEN GOVERNMENT DRAWINGS, SPECIFICATIONS, OR OTHER DATA ARE USED FOR ANY PURPOSE OTHER THAN IN CONNECTION WITH A DEFINITELY GOVERNMENT-RELATED PROCUREMENT, THE UNITED STATES GOVERNMENT INCURS NO RESPONSIBILITY OR ANY OBLIGATION WHATSOEVER. THE FACT THAT THE GOVERNMENT MAY HAVE FORMULATED OR IN ANY WAY SUPPLIED THE SAID DRAWINGS, SPECIFICATIONS, OR OTHER DATA, IS NOT TO BE REGARDED BY IMPLICATION, OR OTHERWISE IN ANY MANNER CONSTRUED, AS LICENSING THE HOLDER, OR ANY OTHER PERSON OR CORPORATION; OR AS CONVEYING ANY RIGHTS OR PERMISSION TO MANUFACTURE, USE, OR SELL ANY PATENTED INVENTION THAT MAY IN ANY WAY BE RELATED THERETO.

THIS REPORT HAS BEEN REVIEWED BY THE OFFICE OF PUBLIC AFFAIRS (ASD/PA) AND IS RELEASABLE TO THE NATIONAL TECHNICAL INFORMATION SERVICE (NTIS). AT NTIS IT WILL BE AVAILABLE TO THE GENERAL PUBLIC INCLUDING FOREIGN NATIONS.

THIS TECHNICAL REPORT HAS BEEN REVIEWED AND IS APPROVED FOR PUBLICATION.

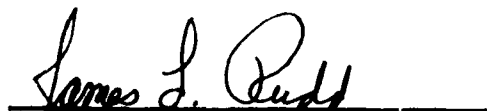
  
GEORGE P. SENDECKY

Aerospace Engineer  
Fatigue, Fracture and Reliability Group  
Structural Integrity Branch

  
KEVIN L. BOYD

Technical Manager  
Fatigue, Fracture and Reliability Group  
Structural Integrity Branch

FOR THE COMMANDER

  
JAMES L. RUDD

Chief  
Structural Integrity Branch  
Structures Division

IF YOUR ADDRESS HAS CHANGED, IF YOU WISH TO BE REMOVED FROM OUR MAILING LIST, OR IF THE ADDRESSEE IS NO LONGER EMPLOYED BY YOUR ORGANIZATION PLEASE NOTIFY WL/WIBEC, WRIGHT-PATTERSON AFB, OH 45433-6553 TO HELP MAINTAIN A CURRENT MAILING LIST.

COPIES OF THIS REPORT SHOULD NOT BE RETURNED UNLESS RETURN IS REQUIRED BY SECURITY CONSIDERATIONS, CONTRACTUAL OBLIGATIONS, OR NOTICE ON A SPECIFIC DOCUMENT.

UNCLASSIFIED

SECURITY CLASSIFICATION OF THIS PAGE

## REPORT DOCUMENTATION PAGE

1a. REPORT SECURITY CLASSIFICATION <b>UNCLASSIFIED</b>			1b. RESTRICTIVE MARKINGS <b>N/A</b>	
2a. SECURITY CLASSIFICATION AUTHORITY <b>N/A</b>			3. DISTRIBUTION/AVAILABILITY OF REPORT <b>APPROVED FOR PUBLIC RELEASE; DISTRIBUTION UNLIMITED</b>	
2b. DECLASSIFICATION/DOWNGRADING SCHEDULE <b>N/A</b>				
4. PERFORMING ORGANIZATION REPORT NUMBER(S)			5. MONITORING ORGANIZATION REPORT NUMBER(S) <b>AFWAL-TR-85-3019</b>	
6a. NAME OF PERFORMING ORGANIZATION <b>Purdue University</b>		6b. OFFICE SYMBOL (If applicable) <b>AFWAL/FIBEC</b>	7a. NAME OF MONITORING ORGANIZATION <b>Air Force Wright Aeronautical Laboratories AFWAL/FIBEC</b>	
6c. ADDRESS (City, State and ZIP Code) <b>West Lafayette, IN. 47907</b>			7b. ADDRESS (City, State and ZIP Code) <b>W-PAFB, OH. 45433-6553</b>	
8a. NAME OF FUNDING/SPONSORING ORGANIZATION <b>Flight Dynamics Laboratory</b>		8b. OFFICE SYMBOL (If applicable) <b>AFWAL/FIBEC</b>	9. PROCUREMENT INSTRUMENT IDENTIFICATION NUMBER <b>F33615-82-K-3218</b>	
8c. ADDRESS (City, State and ZIP Code) <b>W-PAFB, OH. 45433-6553</b>			10. SOURCE OF FUNDING NOS.	
			PROGRAM ELEMENT NO. <b>61102F</b>	PROJECT NO. <b>2307</b>
			TASK NO. <b>N1</b>	WORK UNIT NO. <b>20</b>
11. TITLE (Include Security Classification) <b>See block 16</b>				
12. PERSONAL AUTHOR(S) <b>C.T. Sun, J.F. Doyle, and D. Kenaga</b>				
13a. TYPE OF REPORT <b>Interim</b>		13b. TIME COVERED <b>FROM 6/1982 TO 6/1985</b>		14. DATE OF REPORT (Yr., Mo., Day) <b>June 1985</b>
15. PAGE COUNT <b>110</b>				
16. SUPPLEMENTARY NOTATION <b>THE CHARACTERIZATION OF BORON/ALUMINUM COMPOSITE AS AN ORTHOTROPIC ELASTIC-PLASTIC MATERIAL</b>				
17. COSATI CODES			18. SUBJECT TERMS (Continue on reverse if necessary and identify by block number)	
FIELD	GROUP	SUB. GR.	<b>METAL-MATRIX COMPOSITES, BORON-ALUMINUM, ELASTIC-PLASTIC BEHAVIOR, ORTHOTROPIC MATERIAL, PLASTIC ZONES, CRACKS</b>	
<b>11</b>	<b>04</b>			
19. ABSTRACT (Continue on reverse if necessary and identify by block number)				
<p>Preliminary testing showed that Boron/aluminum displayed nearly linear elastic behavior up to failure when stressed in the fiber direction, but proved to be quite ductile in off-axis tests. Further, fatigue cracks could not be grown through the fibers but would always propagate parallel to the fibers irrespective of the initial orientation of the crack.</p> <p>An in-depth study of the room temperature tensile behavior of boron/aluminum composite was conducted. This behavior was accurately described using an orthotropic elastic-plastic constitutive model.</p> <p>An investigation into the crack-tip plastic zones in boron/aluminum was conducted both experimentally and analytically, and the results help explain the fatigue growth pattern.</p>				
20. DISTRIBUTION/AVAILABILITY OF ABSTRACT <b>UNCLASSIFIED/UNLIMITED <input checked="" type="checkbox"/> SAME AS RPT. <input type="checkbox"/> OTIC USERS <input type="checkbox"/></b>			21. ABSTRACT SECURITY CLASSIFICATION <b>UNCLASSIFIED</b>	
22a. NAME OF RESPONSIBLE INDIVIDUAL <b>GEORGE P. SENDECKYJ</b>			22b. TELEPHONE NUMBER (Include Area Code) <b>(513) 255-6104</b>	22c. OFFICE SYMBOL <b>AFWAL/FIBEC</b>

## TABLE OF CONTENTS

	Page
INTRODUCTION. . . . .	1
Chapter 1    PRELIMINARY TESTS . . . . .	3
MATERIAL PROPERTIES. . . . .	3
Clip Gage . . . . .	4
0° Tests. . . . .	5
90° Tests . . . . .	7
10° Test. . . . .	7
FATIGUE TESTS. . . . .	9
90° Test. . . . .	10
0° Tests. . . . .	10
Off-Axis Test . . . . .	11
FRACTURE TESTS . . . . .	11
DISCUSSION . . . . .	12
Chapter 2    FORMULATION OF ORTHOTROPIC ELASTOPLASTICITY . . . . .	16
ELASTIC ORTHOTROPIC FORMULATION. . . . .	16
PLASTIC ORTHOTROPIC FORMULATION. . . . .	17
Three-Parameter Formulation . . . . .	19
Effective Stress and Strain . . . . .	20
Uniaxial Specimens. . . . .	21
EXPERIMENTAL TESTING AND ANALYSIS. . . . .	23
Elastic Characterization. . . . .	24
Plastic Characterization. . . . .	24
Limiting Values . . . . .	25
COMPUTER MODELING. . . . .	27
Parametric Study. . . . .	27
Chapter 3    MATERIAL CHARACTERIZATION . . . . .	30
TEST SPECIMENS AND DATA COLLECTION . . . . .	30
The Clip Gage . . . . .	31
Data Reduction. . . . .	31

ELASTIC ORTHOTROPIC ANALYSIS. . . . .	33
PLASTIC ORTHOTROPIC ANALYSIS. . . . .	33
DISCUSSION. . . . .	35
Chapter 4 STRESS ANALYSIS OF CRACKS. . . . .	37
EXPERIMENTAL STUDY. . . . .	37
Tapered Specimen . . . . .	37
Strain Gage Strips . . . . .	39
Study of Transverse Crack. . . . .	40
Study of Oblique Crack . . . . .	40
APPROXIMATE ELASTIC-PLASTIC ANALYSIS OF CRACKS. . . . .	41
A Crack in an Infinite Orthotropic Sheet . . . . .	41
Reconsidering the Strain Gage Results. . . . .	43
DISCUSSION OF PLASTICITY EFFECTS AND FATIGUE . . . . .	44
CONCLUSION . . . . .	45
LIST OF REFERENCES . . . . .	47

Accession For	
NTIS CRA&I	<input checked="" type="checkbox"/>
DTIC TAB	<input type="checkbox"/>
Unannounced	<input type="checkbox"/>
Justification	
By	
Distribution /	
Availability Codes	
Dist	Avail and/or Special
A-1	

ENCLOSURE 1

## LIST OF FIGURES

Figure	Page
1. Specimen cutting plan for B/A1 panel 1. A photograph of the magnified cross section shows the 11 ply thickness. The section was cut with a diamond saw and then polished. Note that several fibers have cracked ends. . . . .	53
2. Schematic for mechanical properties testing. Load versus strain histories were recorded on X-Y plotters. . . . .	54
3. Results of comparison test between strain gages and the clip gage. This data was taken from B/A1 specimen 5. . . . .	55
4. Typical stress-strain behavior obtained for B/A1 principal material directions . . . . .	56
5. Last eight load/unload cycles for B/A1 specimen 7. Each cycle is spaced apart for clarity. Note the lack of residual strain when unloaded. The specimen failure is indicated by the x-mark . . . . .	57
6. Stress-strain history of B/A1 specimen 8 with periodic unloadings. The specimen failure is indicated by the x-mark . . . . .	58
7. Elastic modulus versus plastic strain data taken from specimen 8. The modulus is observed to decrease substantially with increasing plastic strain. See Figure 6 . . . . .	59
8. Schematic for fatigue testing. A travelling microscope was used to observe and measure fatigue crack growth. . . . .	60
9. Schematic representation of cracks in B/A1 emanating from the notch tip and propagating parallel to the fibers. . . . .	61
10. Schematic of how the fiber angle is determined from the exposed specimen edge after cutting . . . . .	62
11. Normalized strain versus fiber orientation for a typical graphite/epoxy composite. The normalized shear strain peaks around 10° . . . . .	63

# LIST OF FIGURES (continued)

Figure	Page
12. Normalized strain versus fiber orientation for B/Al. The normalized shear strain peaks around 40° . . . . .	64
13. Illustration of a uniaxial specimen cut at an arbitrary angle to the principal material directions. . . . .	65
14. Stress-Strain curves for a hypothetical material with anisotropic elastic and isotropic plastic behavior, generated with the UNIAX.F program. . . . .	66
15. Transverse versus longitudinal strains for a hypothetical material with anisotropic elastic and isotropic plastic behavior, generated with the UNIAX.F program . . . . .	67
16. Stress-strain curves for a hypothetical material with isotropic elastic and anisotropic plastic behavior, generated with the UNIAX.F program. . . . .	68
17. Transverse versus longitudinal strains for a hypothetical material with isotropic elastic and anisotropic plastic behavior, generated with the UNIAX.F program . . . . .	69
18. Specimen cutting plan for B/Al panel 2. . . . .	70
19. Illustration of a typical coupon specimen used in the tests outlined in Chapter 3 . . . . .	71
20. Schematic of the test setup with data acquisition system. . . . .	72
21. Stress versus strain data for clip gage calibration for half-inch wide specimens. Calibration was conducted on an aluminum specimen with known material properties. . . . .	73
22. Clip gage strain versus strain gage strain data from Figure 21. This plot shows the linear relation between the two strains even in the post-yield region. The plot deviates from the expected 45° line, indicating that a calibration factor is required. . . . .	74
23. Stress versus longitudinal strain for various fiber orientations, B/Al. The solid lines indicate the computer modeling of the experimental data. . . . .	75
24. Stress versus longitudinal strain for various fiber orientations. (Same data as in Figure 23 shown on an expanded scale.) . . . . .	76

# LIST OF FIGURES (continued)

Figure	Page
25. Transverse versus longitudinal strain for various fiber orientations. The solid lines indicate the computer modeling of the experimental data. . . . .	77
26. Transverse versus longitudinal strain for various fiber orientations. (Same data as in Figure 25 shown on an expanded scale.). . . . .	78
27. Elastic Poisson's ratio data versus fiber angle. The solid line is the curve-fit for determining the s-values. . . . .	79
28. Elastic modulus versus fiber angle. The solid line is a least-squares curve-fit. The dashed line is the effective elastic modulus vs. fiber angle computed from the solid line curve-fit. . . . .	80
29. Plastic Poisson's ratio versus fiber angle. The dashed line is for the least-squares curve-fit. The solid line is the preferred curve-fit . . . . .	81
30. Effective stress versus effective plastic strain for the r-values found from the least-squares curve-fit. Note that the 0° data is not modeled well . . . . .	82
31. Effective stress versus effective plastic strain for the preferred curve-fit r-values. The solid line is the modeling curve . . . . .	83
32. Schematic of the tapered specimen with dimensions and strain gage locations. The specimen was cut using electric discharge machining. . . . .	84
33. Load versus strain data from the five longitudinal gages of the tapered specimen. The data shows a progression of yielding along the specimen length as the load increases . . . . .	85
34. The data presented in Figure 33 is presented here as net section stress versus strain. The data falls nearly along the same line. Data from the 45° coupon specimen and finite element modeling is included for comparison. . . . .	86
35. Schematic of specimen 26 for the transverse crack study. The strain gage strip was cut into two sections and positioned as shown. . . . .	87



## LIST OF FIGURES (continued)

Figure	Page
36. The data from gages 1, 3, 5, and the remote gage of specimen 26 is presented to emphasize the strain distribution at the crack tip. The data was taken during the 1.5 overload cycle. Note that gages 1, 3, and 5 appear to show yielding all at the same stress level. This indicates that the previous loading had yielded the material at each gage location. . . . .	88
37. Schematic of specimen 27 for the oblique crack study. The strain gage strip was cut into two sections and positioned as shown . . . . .	89
38. The data from gages 1, 3, 5, and the remote gage of specimen 27 is presented to emphasize the strain distribution at the crack tip. The data was taken during the 1.5 overload cycle. Note that the gages appear to show yielding at different load levels. This indicates that the gages have recorded an increase of the plastic zone size during the 1.5 overload. . . . .	90
39. Global coordinates convention for the study of cracks in Chapter 4. . . . .	91
40. Plastic zone shape at the crack tip generated with ELLPLAS.F program. Fibers are perpendicular to the crack, and loading is as shown. The crack length is .31" (crack shown not to scale with plastic zones) . . . . .	92
41. Plastic zone shape at the crack tip generated with ELLPLAS.F program. The fibers are parallel to the crack, and loading is as shown. The crack length is .31" (crack shown not to scale with plastic zones) . . . . .	92
42. Plastic zone shape at the crack tip generated with ELLPLAS.F program for an isotropic material. The crack length is .31" (crack shown not to scale with plastic zones). . . . .	93
43. Plastic zone shape at the crack tip generated with ELLPLAS.F program for fibers parallel to the crack and load angle at 90°. This figure is similar in nature to Figure 41. The crack length is .39" (crack shown no to scale with plastic zones) . . . . .	94
44. Plastic zone shape at the crack tip generated with ELLPLAS.F program. The fibers are parallel to the crack with the load angle at 120°. The crack length is .39" (crack shown not to scale with plastic zones). This crack geometry and loading is similar to that of specimen 27 . . . . .	94

# LIST OF FIGURES (continued)

Figure	Page
45. Plastic zone shape at the crack tip generated with ELLPLAS.F program. The fibers are parallel to the crack with the load angle at $150^\circ$ . The crack length is .39" (crack shown not to scale with plastic zones).	95
46. Effective stress along the X-axis for specimen 26. Note that the plastic zone boundary is determined by where the plot crosses the effective yield line. The gage locations along the axis are as shown.	96
47. Effective stress along the Y-axis for specimen 26. Note that the plastic zone boundary is determined by where the plot crosses the effective yield line. The gage locations along the axis are as shown.	97
48. Effective stress along the X-axis for specimen 27. Note that the plastic zone boundary is determined by where the plot crosses the effective yield line. The gage locations along the axis are as shown.	98
49. Effective stress along the Y-axis for specimen 27. Note that the plastic zone boundary is determined by where the plot crosses the effective yield line. The gage locations along the axis are as shown.	99

## LIST OF TABLES

Table		Page
1. A comprehensive listing of B/A1 specimens cut from panel 1 as shown in Figure 1. . . . .		48
2. Mechanical properties of B/A1 (tensile, room temperature). . . . .		49
3. A comprehensive listing of B/A1 specimens cut from panel 2 as shown in Figure 18 . . . . .		50
4. Mechanical properties of B/A1 (tensile, room temperature) obtained from tests outlined in Chapter 3 conducted on specimens 17 through 24. . . . .		51
5. A summary of the failure modes and ultimate longitudinal failure strains for specimens 17 through 24. . . . .		52

## INTRODUCTION

It is well known that plasticity plays an important role in crack growth in metals. Due to the pronounced plastic behavior in many of the matrix metals (e.g. aluminum or titanium) used in metal-matrix composites the same is expected to be true for these new materials also. Consequently, establishing the relation between the matrix plasticity and the overall fatigue properties of the composite will aid considerably in understanding the crack growth process.

One of the most important plasticity effects in fatigue is the retardation of the crack growth due to overloads. There have been extensive studies on the overload effects in homogeneous metals, but no research has been done on this aspect of the fatigue behavior in metal-matrix composites. The present research is part of a systematic study to obtain such information.

No meaningful study of retardation effects can be pursued without first performing an in-depth analysis of the elastic-plastic behavior of the material. Consequently, considerable effort was spent in this stage and the present report summarizes the results.

Chapter 1 describes some of the preliminary tests performed on the B/Al composite. It was concluded that this material appeared to behave like an orthotropic elastic-plastic material. Chapter 2 then proceeds to a proper formulation of anisotropic elastoplasticity plus a scheme for determining the relevant material properties. Chapter 3 shows the results of the experimental characterization. Finally, Chapter 4 considers the problem of determining experimentally the stress and strain fields surrounding the crack tip during fatigue loading.

The studies reported here form the foundation for the later experimental and numerical studies of the effects of plasticity on the fatigue crack propagation in B/Al metal-matrix composites.

## Chapter 1 PRELIMINARY TESTS

In order to make a decision as to how to proceed with the characterization of a metal-matrix material a working knowledge of its basic behavior had to be established. First, tensile tests were done to determine principal direction material properties. Additionally, some fatigue, fracture, and overload tests were also conducted to explore its major crack growth behavior.

### MATERIAL PROPERTIES

The two plates of boron/aluminum received from AMERCOM were nominally 12" x 24". These plates consisted of 11 plies of 5.6 mil boron fibers in a matrix of 6061 aluminum. The ply layup was unidirectional for both plates, the fibers running lengthwise. The nominal thickness of the plates was .077", and the fiber volume fraction was 47.5%. Both plates showed signs of being slightly warped across the direction perpendicular to the fibers.

The specimens were cut from the panel using a 6" diameter diamond wheel .04" in thickness, turning at 1335 RPM. Water cooling was employed to protect the material from frictional heating. The cutting machine had an automatic feed table to which the panel was clamped. The feed rate was approximately 5 inches per second back and forth, and the blade was slowly lowered through the thickness of the panel at a rate of approximately .001" per eight passes of the table. For cutting notches in the fatigue and fracture specimens, the same machine was employed with the edge of the specimen held perpendicular to the blade and with the table stationary.

Figure 1 shows the specimen cutting plan for the first of the two panels. Table 1 is a list of all specimens cut from panel 1, giving their dimensions and uses. Five specimens of nominal dimensions 9" x 1" x .077" were tested using the setup shown in Figure 2 to give the orthotropic material properties. Aluminum tabs were used on all specimens to protect the fibers from being crushed by the waffle pattern of the grips. The tabs were applied with cyanoacrylate glue (commonly referred to as "super-glue"). The strength of the glue is superior to that of epoxy, and much more convenient to use because it sets up in seconds rather than hours.

#### Clip Gage

The strains were taken from the specimens using a clip gage manufactured by Measurements Technology, Inc., and it allowed both longitudinal and transverse strains to be recorded simultaneously. Four arms ending in pins attach the gage to the specimen as shown in Figure 3. Two of the arms bend freely as the specimen elongates, and strain gages on these arms yield the longitudinal strain. As the specimen width is changed by the Poisson's contraction, the transverse strain is picked up by the gages on the spring which holds the pins onto the specimen. During testing, both longitudinal arms of the clip gage were wired into a Wheatstone bridge to complete a full-bridge. The single transverse arm of the gage was wired into a half-bridge. In all cases where the clip gage was used, a 10 volt bridge excitation was maintained. Averaging both longitudinal arm sensitivities, the bridge output voltage is converted to specimen strain by the factor  $1 \text{ mv} = 1155 \text{ } \mu\epsilon$ . For the transverse direction the strain conversion factor is  $1 \text{ mv} = 3650 \text{ } \mu\epsilon$ . (Note the lack of

sensitivity in the transverse direction.) Figure 3 shows a comparison of both strain gage and clip gage results. The data for this particular comparison comes from the test conducted on B/Al specimen 5 (10° off-axis specimen). The resistance gages and the clip gage both show essentially the same results. The clip gage has the advantage of measuring the strain of the middle surface and consequently will not pick up out-of-plane bending. This is significant since the panels exhibited some initial warping. Further, the clip gage is more reliable for obtaining the large strains after yielding. The particular clip gage used was calibrated at the factory and was shown to give linear output up to a strain of .025 in/in. The compliance of the clip gage was not a problem due to the relative stiffness of the material.

Combining the load voltage output from the MTS 810 control panel and the Wheatstone bridge outputs, X-Y plotters were used to record the load-strain histories. The following sections provide details of the five uniaxial specimen tests and the results obtained. A summary of the orthotropic material constants obtained from these tests is shown in Table 2. A plot of the typical principal material direction stress-strain curves obtained from these tests is shown in Figure 4. Note the ductility in the transverse direction and nearly brittle behavior in the longitudinal direction.

#### 0° Tests

Specimen 6 was loaded monotonically to failure, and only longitudinal strain data was taken. The material in this test displayed nearly linear behavior up to fracture. (Although the tests on specimens 6 and



7 were conducted with the MTS on load-control, later tests run under stroke-control gave identical results.) The ultimate stress was 222 ksi. The initial elastic modulus was found to be 30.3 ksi.

Specimen 7 was tested on two occasions; the first test was to obtain the elastic material constants (highest stress level of this test was 40 ksi) and the second test conducted was a series of loading and unloading to observe the cyclic hysteresis behavior. Up to a stress of 20 ksi the average slope of the stress-strain curve yielded a value of 32.6 ksi for Young's modulus. At a stress level of 40 ksi this value dropped to 29.5 ksi. In the second test the specimen was loaded in cycles of increasing maximum stress in order to observe whether there was any residual strain when unloaded. Despite the fact that the unloading curves never followed the loading curves, the strain always returned to zero; no residual strain was observed. In the first loading cycle, longitudinal and transverse strains yielded a value of .29 for Poisson's ratio ( $\nu_{12}$ ). For each loop, an average elastic modulus ( $E_1$ ) was calculated using the two reversal points for the slope. The test and results are summarized below:

9 cycles at maximum stress of 160 ksi  
Average modulus  $E = 29.4$  ksi

5 cycles at maximum stress of 190 ksi  
Average modulus  $E = 28.9$

1 cycle at maximum stress of 196 ksi  
Average modulus  $E = 28.5$  ksi

Cycle up to failure at stress of 204 ksi

Figure 5 shows a reproduction of the last eight cycles before failure of specimen 7 taken from the X-Y plotter. Each cycle was spaced apart for clarity.

### 90° Tests

Specimen 9 was loaded monotonically to failure. Extensive yielding was observed, with a failure strain of .0132 in/in and an ultimate load of 27.0 ksi. Yielding was first observed at a stress of 14.5 ksi. Using a .05% yield criterion, the yield stress was 16.8 ksi. The failure stress of this specimen was 26.5 ksi. A value of  $\nu_{21} = .37$  was calculated from the transverse strain data in the linear region.

Specimen 8 was loaded to failure but with intermittent unloadings to observe the residual strains associated with the yielding. Figure 6 is a reproduction of the plotted data. From the elastic loading slope the value of Young's modulus was calculated to be 20.3 msi while a value of .21 was calculated for  $\nu_{21}$ . The onset of yielding occurred earlier than it did in specimen 9 at a stress of 10.3 ksi. According to the .05% yield criterion, the yield stress was 15.6 ksi. Similar to the cyclic test of specimen 7, the unloading paths were different than the loading curves. This time, of course, residual strains were observed. For each unloading cycle a value of average modulus was calculated (again using the two reversal points) and these values were plotted against the plastic strain at which they occurred. The plot of this data can be seen in Figure 7. Note that the material appears to soften with progressing strain. This softening is probably due to fiber/matrix debonding.

### 10° Test

The purpose of doing an off-axis test was to obtain a value of the elastic shear modulus and an approximate value for the ultimate shear stress. The idea for a 10° specimen was obtained from Reference [1].

This paper recommends that the  $10^\circ$  off-axis tensile specimen be considered as a possible standard for characterization of inplane shear of unidirectional fiber composites. The method requires strain data from a gage rosette to calculate the inplane shear strain, while the inplane shear stress is found from the stress transformation equation. The slope of the resulting shear stress-strain curve yields the shear modulus  $G_{12}$ . The necessary equations for this reduction are

$$\begin{aligned}
 e_x &= e_1 & e_1 &= 0^\circ \text{ gage} \\
 e_y &= (2e_2 + 2e_3 - e_1)/3 & e_2 &= 120^\circ \text{ gage} \\
 e_{xy} &= 2(e_3 - e_2)/\sqrt{3} & e_3 &= 240^\circ \text{ gage} \\
 e_{12} &= (e_y - e_x)\sin 2\theta + e_{xy}\cos 2\theta & \text{and } \theta &= 10^\circ \\
 \sigma_{12} &= \frac{1}{2}\sigma_x \sin 2\theta
 \end{aligned} \tag{1.1}$$

The value of the elastic shear modulus obtained by this method from specimen 5 was 7.55 msi. The shear modulus was also calculated from the equation of the apparent elastic modulus for an orthotropic lamina stressed in a nonprincipal material direction. The equation for the apparent elastic modulus, which is good only for uniaxial stress, is

$$\begin{aligned}
 1/E_\theta &= \cos^4 \theta / E_1 + \sin^4 \theta / E_2 + \\
 &\quad (1/G_{12} - 2\nu_{12}/E_1)\sin^2 \theta \cos^2 \theta
 \end{aligned} \tag{1.2}$$

Solving for  $G_{12}$ , the value of the elastic shear modulus obtained by this method was 7.65 msi, which compares favorably with the value from the slope of the stress-strain curve. A parametric study of the above equation reveals, however, that the value of  $G_{12}$  calculated is very sensitive to the values of  $E_\theta$  and  $E_1$  used.

The value of the intralaminar shear stress  $\sigma_{12}$  was calculated to

be 19.4 ksi at specimen failure. Figure 4 does not show the failure point of the shear curve because it is off the graph at approximately .083 in/in shear strain.

#### FATIGUE TESTS

All fatigue tests were performed using the setup shown in Figure 8. The microscope used was made by the Precision Tool and Instrument Co. Ltd. and gave an approximate x7 magnification. Cross hairs in the eyepiece were used to locate the crack tip and the relative movement of the crack was read off the vernier scales of the microscope. Each test was run with a constant amplitude sinusoidal load cycle, tension-tension ( $\sigma_{\min} \approx 0$ ), at a frequency of 10 Hz at room temperature.

To aid visualization of the crack tip, Spotcheck dye penetrant made by Magnaflux was applied, along with a developer. Tests on regular aluminum specimens were conducted with and without the Spotcheck penetrant to determine whether it had any effect on the crack growth rate. In the low cycle fatigue range typical of these tests there was no indication that the penetrant had any effect on the crack growth rate.

Crack measurements were made with the machine stopped. These measurements were taken only on one side of the specimen which had been polished prior to cycling with 600 grit paper and finished with tripoli buffing compound.

Note that the notches cut into the specimens to initiate the fatigue cracks were at least .04" wide (the width of the diamond blade). The notch roots were not quite square but were somewhat rounded.

### 90° Test

For specimen 10, the crack initiated from the notch root and propagated parallel to the fibers (perpendicular to the loading direction). The results are similar in nature to what would be expected from a crack growing transverse to the load in a homogeneous material.

### 0° Tests

For the specimens with a notch cut perpendicular to the fibers it was found to be impossible to initiate a transverse fatigue crack. Specimen 1 was given a .166" notch and cycled at a maximum stress of 22 ksi, which was not sufficient to grow a crack through the fibers. Figure 9 shows in schematic form how the cracks propagated along the fibers in a mode II fashion. The notch was then cut deeper into the specimen (from .166" to .315") and again a transverse crack could not be initiated. Cutting the notch back even further (from .315" to .74") and cycling at a maximum stress of 15.2 ksi, the cracks were again observed to only grow parallel to the fibers. From this point on, the nominal width of 3" for the specimens was thought to be wasteful for the 0° specimens. Specimen 1 itself was cut into two pieces to perform two tests: Specimen 1a with a .74" notch and the longitudinal fatigue cracks still in it was loaded to failure to observe the failure mode, and specimen 1b was given a notch of .122". The results of the test on specimen 1a are given in the following section of fracture tests. Specimen 1b was cycled at a maximum stress of 37.1 ksi and the cracks that initiated at the notch root again grew parallel to the fibers. The load was increased at this point, but even up to the cyclic load of 79.3 ksi the cracks did not turn but grew rapidly along the fibers. The notch was

cut deeper (from .122" to .281") and given an initial cyclic load of 61.7 ksi. Again the cracks initiated from the notch tip and traveled parallel to the fibers.

In addition to providing crack growth data specimen 15 was used to provide information on the relative load levels required to propagate cracks in mode II. For the specimen geometry given in Table 1, the fatigue threshold was found to be approximately 8.5 ksi, where  $da/dN$  was calculated to be nearly  $300 \times 10^{-9}$  in/cycle.

#### Off-Axis Fatigue Test

To confirm that the fatigue cracks in boron/aluminum will always propagate parallel to the fibers, a 15° off-axis specimen (Specimen 2) was machined so that the notch was perpendicular to the load (and 75° to the fibers). Once again the crack grew parallel to the fibers when a cyclic stress of 10.8 ksi was applied.

#### FRACTURE TESTS

The fracture loads for the material at different fiber orientations were required in order to know how much of an overload could be applied to the fatigue specimens.

The fracture test conducted on specimen 1a showed that a 0° specimen with pre-grown cracks (parallel to the fibers) still has considerable strength. A load of 8230 lbs. was required to break specimen 1a. This corresponds to a remote stress of 55.7 ksi, or a net section stress of 90.6 ksi. The fatigue cracks in the specimen were observed to extend only a small amount before the specimen ruptured. The fracture surface ran perpendicular to the fibers. Since no cracks could be initiated

through the fibers in the  $0^\circ$  direction, all that could be done was a fracture test of a notched specimen without fatigue cracks. This was done on specimen 14. The notch radius was approximately .025 inch. The fracture load was 8775 lbs., corresponding to a remote stress of 74 ksi.

Fracture occurred in specimen 13 while attempting to apply an overload of 2.0 times the maximum cyclic stress. The crack length had grown to .301 inch when the overload was attempted. The maximum load achieved was 4150 lbs. (17.56 ksi remote stress).

#### DISCUSSION

Concerning the cutting of the materials, because of the relative brittleness of the boron fibers it is possible that the diamond saw may have caused local damage to the fibers. Since the cutting was water cooled, heating of the specimen was not a problem. An altogether different method of cutting the material with electric discharge machining is introduced in Chapter 4.

Since the panels delivered had rough edges, it was not possible to determine the exact fiber orientation in the plate when laying out the cutting lines. It was fortunate that in the manufacturing process the fibers caused a ridged pattern to be formed on the surface of the plates by which the fiber orientation could be found. To check the accuracy of the cutting, the following analysis was performed: Close-up photographs of the edges of the specimens exposed by the cut were taken. The pictures showed a light and dark contrast between the matrix and the fibers. The fibers, which appeared as dark patches, formed ellipses when cut at an angle. By taking measurements from the photographs of the length-to-width ratios of the exposed fiber face, the angle of the

cut could be determined as shown in Figure 10. Note that the scale of the photograph was not important since the dimensions were ratioed. Also note that this analysis is only accurate for shallow angles (i.e. for specimens with fiber orientations about  $10^\circ$ ). The results obtained indicated that the cutting was accurate to within a one degree tolerance.

During the course of testing, certain advantages and disadvantages were observed when using the clip gage in comparison with strain gages. These are summarized below

Advantages

- measure strain of neutral surface
- two longitudinal arms average inplane bending
- ease and speed of gaging specimens
- reliable for measuring high strain values

Disadvantages

- lack of sufficient sensitivity in transverse direction
- difficult to mount if specimen is too thin
- can only measure longitudinal and transverse strains

Concerning the off-axis specimens used to calculate the inplane shear characteristics: The  $10^\circ$  specimen was convenient in that it did not use up an excess of material, but it was found that for the metal-matrix composite analyzed here the angle of  $10^\circ$  was not optimum for obtaining the shear values. According to Reference [1], for a  $10^\circ$  specimen to be an adequate means of characterizing the inplane shear in a uniaxial composite, the shear stress  $\sigma_{12}$  must be the only component of stress near its critical value, and at failure the fracture must occur at the  $10^\circ$  plane when  $\sigma_{12}$  reaches this critical value. Figure 11 is a plot of the normalized strain versus fiber angle for a typical graphite epoxy material. As can be seen, the normalized intralaminar



shear strain is a maximum at about the  $10^\circ$  orientation, which is a desirable feature for this test method. The orientation at which the normalized shear strain reaches a maximum is a function of the orthotropy of the material. The paper cites results for three materials with  $E_1/E_2$  ratios of 31.2, 16.5, and 3.5; for the latter material the normalized shear strain reached its peak around  $15^\circ$ . For the boron/aluminum material, on the other hand, the ratio of principal elastic moduli is 1.5, and the peak is reached near  $40^\circ$  as can be seen in Figure 12. It can be concluded that for unidirectional composites with low orthotropy as exhibited in these two metal-matrix composites, the  $10^\circ$  off-axis specimen is not ideal for characterization of inplane shear characteristics.

Table 2 includes values of the material constants which have been reported in other literature [Ref. 2]. Most values compare favorably, although the values of Poisson's ratios do not agree as well. Note that for the values found here, and even for values reported elsewhere, the reciprocal relation  $\nu_{12}/E_1 = \nu_{21}/E_2$  for orthotropic materials is not satisfied. This indicates that either the material is not strictly orthotropic or the reported values are not precise.

Finally, the unloading tests performed confirm that this metal-matrix composite exhibits plasticity in the classical sense. That is, the unloading is elastic with a slope nearly that of the initial Young's modulus. Further, the reloading curve is elastic up to the previous maximum stress and then after yielding work-hardening occurs at about the previous rate. This plasticity, however, is very different at different fiber orientations, being nearly zero for the longitudinal specimen.

Thus, it appears that the nonlinear behavior of boron/aluminum metal-matrix composites can be modeled in terms of anisotropic plasticity with work-hardening.

## Chapter 2 FORMULATION OF ORTHOTROPIC ELASTOPLASTICITY

The elastoplastic description of the orthotropic material behavior is broken into two parts, the elastic modeling and the plastic modeling.

### ELASTIC ORTHOTROPIC FORMULATION

The analysis begins with the generalized Hooke's law for anisotropic materials with its fourth order compliance tensor

$$e_{ij} = S_{ijkl} \sigma_{kl} \quad (2.1)$$

where  $e_{ij}$  is the strain tensor,  $\sigma_{kl}$  is the stress tensor and  $S_{ijkl}$  is the compliance. This relation in contracted form is reduced to the three by three matrix equation given below for the case of an orthotropic material under plane stress

$$\begin{Bmatrix} e_{11} \\ e_{22} \\ 2e_{12} \end{Bmatrix} = \begin{bmatrix} S_{11} & S_{12} & 0 \\ S_{12} & S_{22} & 0 \\ 0 & 0 & S_{66} \end{bmatrix} \begin{Bmatrix} \sigma_{11} \\ \sigma_{22} \\ \sigma_{12} \end{Bmatrix} \quad (2.2)$$

The subscripts 1,2 denote principal material directions. (See Reference [3] for more details). We now define the following two new terms: the effective strain  $\bar{e}$  and the effective stress  $\bar{\sigma}$ . These factors are introduced, along with new s-terms, by dividing the equations through by  $S_{22}$  to yield the new equations as shown

$$\begin{Bmatrix} e_{11} \\ e_{22} \\ 2e_{12} \end{Bmatrix} = \begin{bmatrix} s_{11} & s_{12} & 0 \\ s_{12} & 1 & 0 \\ 0 & 0 & 2s_{66} \end{bmatrix} \begin{Bmatrix} \sigma_{11} \\ \sigma_{22} \\ \sigma_{12} \end{Bmatrix} \quad (d\bar{e}/d\bar{\sigma})$$

$$\begin{aligned}
\text{where } s_{11} &\equiv E_2/E_1 & d\bar{e}/d\bar{\sigma} &\equiv s_{22} = 1/E_2 \\
2s_{66} &\equiv E_2/G_{12} & s_{12} &\equiv -\nu_{12}E_2/E_1 = -\nu_{21}
\end{aligned} \tag{2.3}$$

By using the transformation equations for stress and strain for arbitrarily oriented uniaxial specimens (See Figure 13) the following equation is derived for the effective elastic modulus  $\bar{E}$

$$\begin{aligned}
\bar{E} \equiv d\bar{\sigma}/d\bar{e} &= [s_{11}\cos^4\theta + \sin^4\theta \\
&+ 2(s_{66} + s_{12})\sin^2\theta\cos^2\theta](d\bar{\sigma}_\theta/d\bar{e}_\theta)
\end{aligned} \tag{2.4}$$

where  $d\bar{\sigma}_\theta/d\bar{e}_\theta = E_\theta$  is the Young's modulus for the specimen. Similarly, the expression for Poisson's ratio can be found in terms of the  $s$ -values as

$$-\nu_\theta = \frac{d\bar{e}_{T\theta}}{d\bar{e}_\theta} = \frac{(s_{11} + 1 - 2s_{66})\sin^2\theta\cos^2\theta + s_{12}(\sin^4\theta + \cos^4\theta)}{s_{11}\cos^4\theta + \sin^4\theta + 2(s_{12} + s_{66})\sin^2\theta\cos^2\theta} \tag{2.5}$$

The reason for defining the  $s$ -values will become apparent in the following section for the plastic orthotropic formulation.

#### PLASTIC ORTHOTROPIC FORMULATION

The derivation of the orthotropic plasticity relations begins with the statement of the flow rule for plasticity [4] as

$$d\bar{e}_{ij}^p = \partial g / \partial \sigma_{ij} d\lambda^* \tag{2.6}$$

Note that the superscript 'p' indicates plasticity. The plastic flow function  $g$  is assumed quadratic in  $\sigma_{ij}$  as

$$\begin{aligned}
g &= c^p_{ijkl} \sigma_{ij} \sigma_{kl} \\
de^p_{ij} &= \{c^p_{ijkl} \sigma_{kl} + c^p_{mnij} \sigma_{mn}\} d\lambda^* \\
&= 2c^p_{ijkl} \sigma_{kl} d\lambda^*
\end{aligned} \tag{2.7}$$

This can be written in matrix form as

$$\begin{Bmatrix} de_{11} \\ de_{22} \\ de_{33} \\ de_{31} \\ de_{23} \\ de_{12} \end{Bmatrix}^p = \begin{bmatrix} c_{11} & c_{12} & \dots & c_{16} \\ c_{21} & c_{22} & \dots & \\ c_{31} & \dots & \dots & \\ \dots & \dots & \dots & \\ \dots & \dots & \dots & \\ c_{61} & \dots & \dots & c_{66} \end{bmatrix}^p \begin{Bmatrix} \sigma_{11} \\ \sigma_{22} \\ \sigma_{33} \\ c_{31} \\ \sigma_{23} \\ c_{12} \end{Bmatrix} d\lambda^* \tag{2.8}$$

where  $c^p_{ij}$  is symmetric (i.e. it contains 21 independent coefficients all of which may be functions of strain). If the material is plastically orthotropic (that is to say, if the body has three mutually perpendicular planes of material symmetry) then the matrix  $c^p_{ij}$  will exhibit certain additional symmetries. The matrix becomes

$$[c^p] = \begin{bmatrix} c^p_{11} & c^p_{12} & c^p_{13} & 0 & 0 & 0 \\ c^p_{12} & c^p_{22} & c^p_{23} & 0 & 0 & 0 \\ c^p_{13} & c^p_{23} & c^p_{33} & 0 & 0 & 0 \\ 0 & 0 & 0 & c^p_{44} & 0 & 0 \\ 0 & 0 & 0 & 0 & c^p_{55} & 0 \\ 0 & 0 & 0 & 0 & 0 & c^p_{66} \end{bmatrix} \tag{2.9}$$

showing that to describe orthotropic plastic flow only nine independent coefficients are needed. For plane stress situations where  $\sigma_{33} = 0$ ,

$\sigma_{13} = 0$ , and  $\sigma_{23} = 0$  the incremental relations further simplify to

$$\begin{Bmatrix} de_{11}^p \\ de_{22}^p \\ de_{12}^p \end{Bmatrix} = \begin{Bmatrix} c_{11}^p \sigma_{11} + c_{12}^p \sigma_{22} \\ c_{12}^p \sigma_{11} + c_{22}^p \sigma_{22} \\ c_{66}^p \sigma_{12} \end{Bmatrix} d\lambda^* \quad (2.10)$$

Note that the above equations are over-specified with the four  $c$ -values and  $d\lambda^*$ . The  $d\lambda^*$  is retained so that the formulation resembles classical plasticity.

It is noted that the change of volume in the body due to plasticity is given by the expression (for plane stress)

$$\begin{aligned} dv &= e_{11}^p + e_{22}^p + e_{33}^p \\ &= (c_{11}^p + c_{12}^p + c_{13}^p) \sigma_{11} + (c_{12}^p + c_{22}^p + c_{23}^p) \sigma_{22} \end{aligned} \quad (2.11)$$

The change of volume will not be considered further because that would involve the coefficient  $c_{13}^p$ ,  $c_{23}^p$ ,  $c_{33}^p$  which do not occur in the incremental flow rule (2.10).

### Three-Parameter Formulation

Let the following definitions be introduced:

$$\begin{aligned} r_{11} &\equiv c_{11}^p / c_{22}^p \\ r_{66} &\equiv c_{66}^p / c_{22}^p & d\lambda &\equiv c_{22}^p d\lambda^* \\ r_{12} &\equiv c_{12}^p / c_{22}^p \end{aligned} \quad (2.12)$$

Then the new incremental expressions are

$$\begin{Bmatrix} de^p_{11} \\ de^p_{22} \\ de^p_{12} \end{Bmatrix} = \begin{Bmatrix} r_{11}\sigma_{11} + r_{12}\sigma_{22} \\ r_{12}\sigma_{11} + \sigma_{22} \\ r_{66}\sigma_{12} \end{Bmatrix} d\lambda \quad (2.13)$$

The factor of proportionality  $d\lambda$  is solved for from work considerations. Parenthetically this flow rule could have been derived directly by taking the flow function  $g$  as

$$g = \frac{1}{2}[r_{11}\sigma_{11}^2 + \sigma_{22}^2 + 2r_{66}\sigma_{12}^2 + 2r_{12}\sigma_{11}\sigma_{22}]$$

#### Effective Stress and Strain

In general, the plastic work increment is

$$dW^p = \sigma_{ij} de^p_{ij} \quad (2.14)$$

For plane stress conditions this expands to

$$dW^p = \sigma_{11} de^p_{11} + \sigma_{22} de^p_{22} + 2\sigma_{12} de^p_{12} \quad (2.15)$$

Substituting for the incremental strains in terms of the stresses from equation (2.13), the work increment can be rewritten in the form

$$\begin{aligned} dW^p &= \{r_{11}\sigma_{11}^2 + \sigma_{22}^2 + 2r_{66}\sigma_{12}^2 + 2r_{12}\sigma_{11}\sigma_{22}\}d\lambda \\ &= 2gd\lambda \end{aligned} \quad (2.16)$$

Let the effective stress and effective plastic strain be defined such that

$$\overline{\sigma} d\overline{e}^p \equiv dW^p = 2gd\lambda \quad (2.17)$$

Further, define the effective stress as

$$\begin{aligned} \frac{2}{3} \overline{\sigma}^2 &\equiv r_{11}\sigma_{11}^2 + \sigma_{22}^2 + 2r_{66}\sigma_{12}^2 + 2r_{12}\sigma_{11}\sigma_{22} \\ &= 2g \end{aligned} \quad (2.18)$$

Therefore

$$\begin{aligned} \bar{\sigma} d\bar{\epsilon}^p &= \frac{2}{3} \bar{\sigma}^2 d\lambda \\ \text{or} \quad d\lambda &= \frac{3}{2} (d\bar{\epsilon}^p / \bar{\sigma}) = \frac{3}{2} (d\bar{\epsilon}^p / d\bar{\sigma}) (d\bar{\sigma} / \bar{\sigma}) \end{aligned} \quad (2.19)$$

The effective plastic strain consistent with the above definition of effective stress is

$$\begin{aligned} d\bar{\epsilon}^p &= \frac{2}{3} \bar{\sigma} d\lambda \\ \text{or} \quad [d\bar{\epsilon}^p]^2 &= \frac{2}{3} \bar{\sigma} d\bar{\epsilon}^p d\lambda = \frac{2}{3} 2g d\lambda^2 = \frac{4}{9} \bar{\sigma}^2 d\lambda^2 \end{aligned} \quad (2.20)$$

Substituting into  $\bar{\sigma}$  for  $\sigma_{11}$ ,  $\sigma_{22}$ , and  $\sigma_{12}$  in terms of the plastic strains gives

$$\begin{aligned} [d\bar{\epsilon}^p]^2 &= \frac{2}{3} (r_{11} - r_{12}^2)^{-2} [d\epsilon_{11}^p{}^2 + r_{11} d\epsilon_{22}^p{}^2 \\ &\quad - 2r_{12} d\epsilon_{11}^p d\epsilon_{22}^p + 2(r_{11} - r_{12}^2) d\epsilon_{12}^p{}^2 / r_{66}] \end{aligned} \quad (2.21)$$

Note that for the special cases of uniaxial stress applied in the principal material directions there is no shear term  $\sigma_{12}$  and the expression for the effective strain and stress reduces to

$$\begin{aligned} \sigma_{11} \neq 0, \sigma_{22} = 0, \sigma_{12} = 0 &\rightarrow d\bar{\epsilon}^p = (\sqrt{2/3} / r_{11}) d\epsilon_{11}^p, \bar{\sigma} = (\sqrt{\frac{3}{2} r_{11}}) \sigma_{11} \\ \sigma_{22} \neq 0, \sigma_{11} = 0, \sigma_{12} = 0 &\rightarrow d\bar{\epsilon}^p = (\sqrt{2/3}) d\epsilon_{22}^p, \bar{\sigma} = (\sqrt{3/2}) \sigma_{22} \end{aligned} \quad (2.22)$$

The case for 1-D stress at an arbitrary orientation is dealt with below.

### Uniaxial Specimens

For a uniaxial specimen cut from an orthotropic material at an arbitrary orientation to the principal axes, the state of stress is



transformed back to the material directions as follows

$$\begin{aligned}\sigma_{11} &= \sigma_{\theta} \cos^2 \theta \\ \sigma_{22} &= \sigma_{\theta} \sin^2 \theta \\ \sigma_{12} &= \sigma_{\theta} \sin \theta \cos \theta\end{aligned}\tag{2.23}$$

(See Figure 13 for an illustration of the typical uniaxial specimen.)

The incremental strains in the loading direction and in the transverse direction are

$$\begin{aligned}de_{\theta}^p &= de_{11}^p \cos^2 \theta + de_{22}^p \sin^2 \theta + 2de_{12}^p \sin \theta \cos \theta \\ &= [r_{11} \cos^4 \theta + 2r_{12} \cos^2 \theta \sin^2 \theta \\ &\quad + \sin^4 \theta + 2r_{66} \sin^2 \theta \cos^2 \theta] d\lambda \sigma_{\theta}\end{aligned}\tag{2.24}$$

$$\begin{aligned}de_{t\theta}^p &= de_{11}^p \sin^2 \theta + de_{22}^p \cos^2 \theta - 2de_{12}^p \cos \theta \sin \theta \\ &= [r_{11} + 1 - 2r_{66}) \sin^2 \theta \cos^2 \theta \\ &\quad + r_{12} (\sin^4 \theta + \cos^4 \theta)] d\lambda \sigma_{\theta}\end{aligned}$$

The effective stress and the incremental effective plastic strain are found to be

$$\begin{aligned}\bar{\sigma} &= \sqrt{\frac{3}{2} [r_{11} \cos^4 \theta + \sin^4 \theta + 2(r_{66} + r_{12}) \sin^2 \theta \cos^2 \theta]} \sigma_{\theta} \\ d\bar{\epsilon}^p &= de_{\theta}^p / \sqrt{\frac{3}{2} [r_{11} \cos^4 \theta + \sin^4 \theta + 2(r_{66} + r_{12}) \sin^2 \theta \cos^2 \theta]}\end{aligned}\tag{2.25}$$

The ratio  $d\bar{\sigma}/d\bar{\epsilon}^p$  can be derived from the expression for  $d\lambda$ . Substituting the expressions for  $\bar{\sigma}$  and  $d\bar{\epsilon}_{\theta}^p$  to obtain

$$\begin{aligned}
d\lambda &= \frac{3}{2} (d\bar{e}^P/d\bar{\sigma}) (d\bar{\sigma}/\bar{\sigma}) \\
&= \frac{1}{r_{11}\cos^4\theta + \sin^4\theta + 2(r_{66} + r_{12})\sin^2\theta\cos^2\theta} \frac{de_{\theta}^P}{d\sigma_{\theta}} \frac{d\sigma_{\theta}}{\sigma_{\theta}} \quad (2.26)
\end{aligned}$$

Hence obtain

$$\begin{aligned}
d\bar{\sigma}/d\bar{e}^P &= \frac{3}{2} [r_{11}\cos^4\theta + \sin^4\theta \\
&\quad + 2(r_{66} + r_{12})\sin^2\theta\cos^2\theta] (d\sigma_{\theta}/de_{\theta}^P) \quad (2.27)
\end{aligned}$$

The plastic Poisson's ratio effect is defined as  $v_{\theta}^P$ , and takes the form

$$-v_{\theta}^P \equiv \frac{de_{t\theta}^P}{de_{\theta}^P} = \frac{(r_{11} + 1 - 2r_{66})\sin^2\theta\cos^2\theta + r_{12}(\sin^4\theta + \cos^4\theta)}{r_{11}\cos^4\theta + \sin^4\theta + 2(r_{12} + r_{66})\sin^2\theta\cos^2\theta} \quad (2.28)$$

Note that for various orientations the sine or cosine terms are zero and the expression for  $v_{\theta}^P$  simplifies, i.e.

$$\begin{aligned}
\theta = 0^\circ &: -v_0^P = r_{12}/r_{11} \\
\theta = 90^\circ &: -v_{90}^P = r_{12} \\
\theta = 45^\circ &: -v_{45}^P = \frac{r_{11} - 2r_{66} + 2r_{12}}{r_{11} + 2r_{66} + 2r_{12}} \quad (2.29)
\end{aligned}$$

These relations are useful because they give a general idea of how the  $v_{\theta}^P$  versus  $\theta$  plot will look depending on the r-values.

#### EXPERIMENTAL TESTING AND ANALYSIS

By testing uniaxial specimens cut at various angle to the fibers, two relevant sets of data are taken versus the applied stress, i.e., longitudinal strain and transverse strain. The total strains must then be separated into elastic and plastic components.

### Elastic Characterization

The  $s$ -values are solved for by curve-fitting a plot of the elastic Poisson's ratios versus the fiber orientation. Note that in order to determine the three  $s$ -values, at least three data points are required. These values do not serve to characterize the material alone; as was stated before,  $E_2 = d\bar{\sigma}/d\bar{e} = \bar{E}$ , and with the  $s$ -values already calculated the relationship exists to reduce the collected  $E_\theta$  values into the effective elastic modulus,  $\bar{E}$ . Therefore, at least one value of  $E_\theta$  is required to calculate  $\bar{E}$ . Once  $E_2$  is obtained, the other principal direction elastic constants can be obtained from the  $s$ -values using the relations given in equation (2.3).

Note that it is perhaps just as effective to determine  $E_1$ ,  $E_2$ ,  $G_{12}$ , and  $\nu_{12}$  from experimental testing as described in Reference [1]. However, such tests presuppose that the material is orthotropic, while reducing experimental data with the analysis described in this chapter effectively checks for material orthotropy.

### Plastic Characterization

The plastic data collected is organized into two forms. We have:

$$E_\theta^P \equiv d\sigma_\theta/de_\theta^P \qquad -\nu_\theta^P \equiv de_{t\theta}^P/de_\theta^P$$

Observe that  $E_\theta^P$  is essentially similar to an elastic modulus, while  $\nu_\theta^P$  is the plastic Poisson's ratio. It should be noted that both  $E_\theta^P$  and  $\nu_\theta^P$  may be nonlinear functions of strain.

Once the  $r$ -values have been obtained, it is then possible to reduce the stress versus plastic strain data into effective stress versus effective plastic strain. If the  $r$ -values are good, the results of this

reduction will tend to collapse the stress-strain data together so as to form a single curve. This effective stress-strain curve is then curve-fitted as appropriate. The curve-fit should be one which allows for a derivative to be easily taken. It is this derivative ( $d\bar{\sigma}/d\bar{e}^P$ ) which is necessary to complete the analysis. The final form for the orthotropic plastic characterization is given below

$$\begin{Bmatrix} d\bar{e}_{11}^P \\ d\bar{e}_{22}^P \\ 2d\bar{e}_{12}^P \end{Bmatrix} = \begin{bmatrix} r_{11} & r_{12} & 0 \\ r_{12} & 1 & 0 \\ 0 & 0 & 2r_{66} \end{bmatrix} \begin{Bmatrix} \sigma_{11} \\ \sigma_{22} \\ \sigma_{12} \end{Bmatrix} \cdot \frac{3}{2} (d\bar{e}^P/d\bar{\sigma}) (d\bar{\sigma}/\bar{\sigma}) \quad (2.30)$$

where  $d\bar{e}^P/d\bar{\sigma}$  is found from the curve-fit

$$\bar{\sigma} \equiv \frac{3}{2} \sqrt{r_{11}\sigma_{11}^2 + \sigma_{22}^2 + 2r_{12}\sigma_{11}\sigma_{22} + 2r_{66}\sigma_{12}^2}$$

$$d\bar{\sigma} = \frac{3}{2} (1/\bar{\sigma}) [(r_{11}\sigma_{11} + r_{12}\sigma_{22})d\sigma_{11} + (r_{12}\sigma_{11} + \sigma_{22})d\sigma_{22} + 2r_{66}\sigma_{12}d\sigma_{12}]$$

The values of  $r_{11}$ ,  $r_{12}$ ,  $r_{66}$  are found from the curve-fit of the  $v_\theta^P$  versus  $\theta$  data. Note that again three values of  $v_\theta^P$  are required in order to determine the three r-values, and at least one set of  $\bar{\sigma}$  versus  $\bar{e}^P$  data is required to find  $d\bar{e}^P/d\bar{\sigma}$ .

### Limiting Values

Reference [3] gives several expressions which describe limiting values of the elastic orthotropic material constants. The expressions are derived from work considerations and the symmetry of the compliance matrix. Such restrictions are used to check experimental data to see if they are consistent within the framework of the elasticity model.

Similar limiting cases can be derived for the  $r$ -values determined in the plastic analysis.

From equation (2.24), the incremental relation for uniaxial stress is

$$de^p_{\theta} = [r_{11}\cos^4\theta + \sin^4\theta + 2(r_{12} + r_{66})\sin^2\theta\cos^2\theta]\sigma_{\theta}d\lambda$$

Since  $de^p_{\theta}$  must always be positive for a positive  $\sigma_{\theta}$ , then

$$\begin{aligned} r_{11}\cos^4\theta + \sin^4\theta + 2(r_{12} + r_{66})\sin^2\theta\cos^2\theta &\geq 0 \\ \text{or} \quad r_{11} &\geq 0 \quad \text{and} \quad r_{12} + r_{66} \geq 0 \end{aligned} \quad (2.31)$$

Now we let  $r_{11} = 0$  to obtain the following

$$\begin{aligned} de^p_{t\theta} &= [(r_{11} + 1 - 2r_{66})\sin^2\theta\cos^2\theta \\ &\quad + r_{12}(\sin^4\theta + \cos^4\theta)]\sigma_{\theta}d\lambda \\ &= [(1 - 2r_{66})\sin^2\theta\cos^2\theta \\ &\quad + r_{12}(\sin^4\theta + \cos^4\theta)]\sigma_{\theta}d\lambda \end{aligned} \quad (2.23)$$

In order to avoid having a width expansion under a tensile load, then

$$\begin{aligned} r_{12} &\leq 0 \\ \text{and} \quad 1 - 2r_{66} &\leq 0 \quad \text{or} \quad r_{66} \geq .5 \\ \text{hence} \quad r_{12} &\geq -.5 \end{aligned}$$

In summary, we have these limiting conditions which the experimental data should obey

$$\begin{aligned} r_{11} &\geq 0 \\ r_{12} &\geq -.5 \quad \text{and} \quad r_{12} \leq 0 \\ r_{66} &\geq .5 \end{aligned} \quad (2.33)$$

For an isotropic material it is evident from the definitions of the r-values that

$$r_{11} = 1 \quad r_{12} = -.5 \quad r_{66} = 1.5$$

Therefore the r-values for the isotropic case are within the limitations of the mathematical modeling of the plasticity. In Chapter 3 the r-values obtained from the analysis on the experimental data will be checked against these limiting conditions as well.

#### COMPUTER MODELING

The equations for the elastoplastic characterization were put into a program to generate the stress-strain curves of a uniaxial specimen at an arbitrary orientation. The program reads in the material properties and fiber orientation, calculates material stresses by an angle transformation, then calculates elastic strains. A yield criterion based on the effective stress is used, and if the specimen has yielded the work hardening model is employed to calculate the plastic strains. The sum of the elastic strain and plastic strain is output versus the uniaxial stress, for both longitudinal and transverse strain. The work hardening model used is the expression chosen to curve-fit the effective stress-strain curve of the experimental data. The program is called UNIAX.F

#### Parametric Study

Example runs were conducted to gain an understanding of orthotropic plasticity. The work hardening curve used was a simple three-parameter model as given below:

$$\bar{\epsilon}^p = \begin{cases} 0 & : \bar{\sigma} \leq \bar{\sigma}_y \\ (\bar{\sigma}/A)^B - (\bar{\sigma}_y/A)^B & : \bar{\sigma} > \bar{\sigma}_y \end{cases} \quad (2.34)$$

The values used for the parameters were fixed at  $A = 50000$  psi,  $B = 5$ , and  $\bar{\sigma}_y = 20000$  psi. Note that it is this value of  $\bar{\sigma}_y$  which is also used in the yield criterion.

The study focused on two areas; isotropic versus anisotropic and elastic versus plastic. Three orientations were used in each case:  $0^\circ$ ,  $45^\circ$ , and  $90^\circ$ . Obviously, for the isotropic elastic and isotropic plastic case, the stress-strain history is expected to be invariant with respect to specimen orientation. The program proved capable of generating this trivial case.

The next case was to check for anisotropic elastic and isotropic plastic behavior. To accomplish this, the following values were used:

$$\begin{aligned} E_1 &= 20 \text{ msi} & E_2 &= 2 \text{ msi} & G_{12} &= .5 \text{ msi} & \nu_{12} &= .4 \\ r_{11} &= 1 & r_{12} &= -.5 & r_{66} &= 1.5 \end{aligned}$$

The plots of stress versus longitudinal strain and transverse strain versus longitudinal strain are shown in Figures 23 and 24 respectively. The points to observe in Figure 23 are that the elastic slopes are indeed dependent on the fiber angle, and the yield is independent of the fiber angle. It is not obvious from this plot that the work hardening curves obey the same law for each orientation, but it is true in this case. Note that the material yields at a value less than  $\sigma_y = 20000$  psi. This is due to the definition of the effective stress which is used in the yield criterion. The true value of yield is  $\sigma_y = \sqrt{\frac{2}{3}} \bar{\sigma}_y = 16330$  psi for an isotropic plastic material.

In contrast to the previous case, the parameters for an isotropic elastic and anisotropic plastic material were input. (Again, r-values were chosen which were within the limiting conditions for an orthotropic

material.) These values were

$$E_1 = 20 \text{ msi} \quad E_2 = 20 \text{ msi} \quad G_{12} = 7.6923 \text{ msi} \quad \nu_{12} = .3$$

$$r_{11} = .1 \quad r_{12} = -.1 \quad r_{66} = 2.0$$

The plots for this case are shown in Figures 16 and 17. Note that the elastic curves are all independent of the load angle except that for each orientation the yield point is different. Indeed, the  $0^\circ$  specimen has not yielded on this plot. This variation of yield with fiber direction is a product of the anisotropic  $r$ -values. Although it is not obvious from Figure 16, the work hardening curves are also different for each orientation.

Combining the above two cases into an anisotropic elastic and anisotropic plastic case incorporates the features of elastic slopes, yield points, and work hardening curves which vary with fiber orientation.



### Chapter 3 MATERIAL CHARACTERIZATION

The following experimental tests for the characterization of the elastic and plastic orthotropy were designed according to the requirements set forth in Chapter 2.

The tests were intended primarily to obtain the work hardening curves i.e. designed for large strains, but elastic properties obtained were of sufficient quality to perform the elastic characterization.

#### TEST SPECIMENS AND DATA COLLECTION

The tensile specimens for the testing were cut from a second boron/aluminum panel of identical manufacture to the first. The cutting scheme for specimens 17 through 24 appears in Figure 18. Figure 19 shows the typical test specimen. Each specimen was nominally nine inches long with aluminum tabs applied with cyanoacrylate glue, leaving a test section of nominally six inches. The specimen widths were all approximately one-half inch. This gave a length-to-width ratio of 12 which was considered to be adequate for the fiber orientations chosen. The exact dimensions and the fiber orientations for the specimens are summarized in Table 3. Loading was uniaxial tension, with fixed-grip end conditions. To measure the longitudinal and transverse strains the clip gage described in Chapter 1 was used. The output from this gage was digitized and stored on floppy disk. The schematic for the test setup and the data acquisition system is shown in Figure 20. The MTS was operated under head-displacement control to observe the extended yielding of the specimens. Loading was controlled manually, and after each increment the Daytronics was cycled to record the strains and load simultaneously. The data was

stored on the Apple III computer by means of a small program which read from the RS232 port of the Daytronics and wrote directly to disk.

### The Clip Gage

Both longitudinal arms of the clip gage were wired into one channel to complete a full-bridge, and the transverse strain arm was wired in as a half-bridge. A variable potentiometer circuit was constructed to step down the load voltage from the MTS machine. Care was taken not to have a mismatch of impedance when designing the potentiometer. The resulting circuit was capable of reducing the output voltage by a factor of one thousand so that the Daytronics could accept the load voltage into one of the strain conditioners.

Since the clip gage was designed for one-inch wide specimens, a recalibration of it for the narrow specimens was conducted. Figures 21 and 22 show the comparison run on a half-inch wide piece of aluminum with well known material properties. Two strain gages (front and back) were mounted on the specimen to provide a standard to which the clip gage was compared. The deviations of the data from the 45° line as shown in Figure 22 was due to the extended pins used on the clip gage to secure it to the narrow specimen. These longer pins caused an increased moment arm which twisted the gage arm, effectively decreasing the observed strain. A calibration factor of 1.5504 was used for all subsequent tests on half-inch wide specimens.

### Data Reduction

The results of the tensile tests are shown grouped together in Figures 23 through 26. Each plot combines the data for all orientations.

Because of the different orders of magnitude of ultimate stresses and ultimate strains between them, little detail can be seen in Figures 23 and 25. For this reason Figures 24 and 26 give an enlarged view of the yield curves. As can be seen from these plots, the tests give similar results for the 0°, 10°, and 90° orientations as compared with the results presented in Chapter 1. More accurate information concerning the transverse strain was recorded in these tests, however. As seen best in Figure 26 the elastic and plastic Poisson's ratios range from very low in the 90° specimen to very high in the 10° and 20° specimens. The elastic and plastic constants calculated from these tests are tabulated for each orientation in Table 4.

For each orientation the first step was to obtain the elastic modulus. With this value the elastic strains were subtracted from the total strains to give the plastic strains as

$$e_{\theta}^p \equiv e_{\theta} - \sigma_{\theta}/E_{\theta} \quad e_{t\theta}^p \equiv e_{t\theta} - \nu_{\theta}\sigma_{\theta}/E_{\theta} \quad (3.1)$$

These two steps were accomplished with one computer program. Input into the program was the stress versus total strain file along with the number of data points selected to represent the total extent of the elastic (or linear) portion of the curve. The program output the Young's modulus and the elastic Poisson's ratio. It then subtracted the elastic strains according to the above equations and wrote the plastic strain data into a file. A second program was then used to obtain the plastic Poisson's ratios from these files of plastic longitudinal strain versus plastic transverse strain.

## ELASTIC ORTHOTROPIC ANALYSIS

A plot of elastic Poisson's ratio versus fiber orientation is given in Figure 27. (Note that the data reported from Chapter 1 shows considerable scatter. Also, the value of Poisson's ratio obtained from the 65° specimen is considered to be in error.) This data was curve-fit to obtain the values of  $s_{11}$ ,  $s_{12}$  and  $s_{66}$  for boron/aluminum.

Figure 28 is a plot of the elastic moduli versus fiber orientation. The solid line is a least-squares fit of the data. The s-values obtained from Figure 27 were used to reduce both the data points and the curve-fit into effective elastic moduli values. The dashed line is the reduced curve-fit, and it is a constant with fiber direction as expected, with a value of 19.1 msi. Hence, the following values were obtained for the principal material directions

$$\begin{aligned} E_1 &= 29.4 \text{ msi} & E_2 &= 19.1 \text{ msi} \\ \nu_{12} &= .169 & G_{12} &= 7.49 \text{ msi} \end{aligned}$$

These values compare favorably with those reported in other literature.

## PLASTIC ORTHOTROPIC ANALYSIS

Figure 29 shows the plot of the plastic Poisson's ratio values obtained for the various orientations. The figure also shows two curve-fit lines for the data. The dashed line is a least-squares curve fit which, incidently, intercepts the y-axis at a value of  $\nu_{\theta}^p = 4.5$ . The r-values obtained from this curve-fit were used to calculate effective stress and effective strain plots from the plastic data and are plotted together as shown in Figure 30. The effect of missing the 0° data with the curve-fit can be seen quite clearly. All other data sets fall

fairly close together. As was stated in Chapter 2, obtaining this master curve was the primary goal of the analysis so that it may be curve-fit to model the material behavior. Because of the large error bounds on the plastic Poisson's ratio data (perhaps as much as  $\pm .1$ ) it was questionable whether the  $r$ -values given by the least-squares method were optimal for obtaining a master curve of effective stress and strain. A small program was written which allowed the  $r$ -values to be input manually to observe how the resulting output modeled the data. Working by trial and error the solid line curve shown in Figure 29 was obtained for the following  $r$ -values

$$\begin{aligned} r_{11} &= .017 \\ r_{12} &= -.01 \\ r_{66} &= 1.8 \end{aligned} \tag{3.2}$$

Observe that these values are within the limiting conditions stated in Chapter 2. Perhaps these values are not optimal either, but the resulting master curve is superior to the one obtained from the least-square  $r$ -values. For the  $r$ -values given in (3.2) the master curve in Figure 31 was obtained. This plot also shows the parametric curve which was used to fit the data. It was found that the functional form from (2.34) was sufficient for modeling the data,

$$\bar{e}^p = \begin{cases} 0 & : \bar{\sigma} \leq \bar{\sigma}_y \\ (\bar{\sigma}/A)^B - (\bar{\sigma}_y/A)^B & : \bar{\sigma} \geq \bar{\sigma}_y \end{cases}$$

$$A = 64000 \text{ psi} \quad B = 5.8 \quad \bar{\sigma}_y = 14500 \text{ psi} \tag{3.3}$$

This is the functional form of the work hardening model which is incorporated into the computer programs, along with its derivative which is

easily obtained. Using this master curve, the stress versus plastic strain curves for any orientation can be generated.

Combining the elastic and plastic strains, the complete stress-strain histories for any fiber orientation can be produced. Figures 23 through 26 are plots of the generated stress-strain curves superimposed on the actual experimental data. It can be observed that the generated plots capture the essence of the material behavior.

#### DISCUSSION

It is obvious from the figures of the stress-strain data collected that some specimens displayed considerable plastic strain while others failed at relatively low values of plastic strain. This gives rise to the question of damaged specimens. While damage due to cutting is of concern especially as the specimens become thinner, this is only a secondary consideration compared to the damage which may be caused by gripping the tab ends with too much pressure. Specimen 16 for example, which was the first half-inch wide specimen tested, failed at a stress of 141 ksi, not nearly the 200 ksi as expected. When the specimen was removed from the MTS grips it was observed that the material under the tabs had been deformed by excessive grip pressure. Specimen 21 was cut to perform the test over; its data and not that from specimen 16 was used in the analysis. More care was taken in subsequent tests to avoid end damage, yet several of the specimens fractured near the tab ends regardless. A summary of the fracture modes and the ultimate strains from the specimens is presented in Table 5. Under Failure Mode, the term 'end' means that the specimen fractured at the tab,

and 'middle' indicates that the fracture occurred away from the tab. From this table, it is obvious that there is a correspondence between low values of longitudinal failure strains and the fractures which occurred at the tab ends.

Concerning the analysis, it should be noted that the material at a  $0^\circ$  orientation behaves in a singular manner. All other orientations yielded stress-strain curves typical of most ductile metals. Only the  $0^\circ$  specimens behaved as a brittle material. Because it was noted that the specimens showed no residual strain even when stressed nearly to failure, the material in this orientation could be considered linear elastic up to failure. In this case, there would be no plastic strain data and consequently an indeterminate plastic Poisson's ratio for the  $0^\circ$  specimen. The modeling parameters as used here will predict some plasticity for a  $0^\circ$  specimen. However, this is thought to be of little consequence since in a multiaxial stress state the other components of stress will dominate the yielding.

## Chapter 4 STRESS ANALYSIS OF CRACKS

Determining the stress and strain distribution around the crack tip is of primary importance in this chapter. This will be done experimentally by mounting very small strain gages close to the crack. An approximate analysis will be done based on an elastic analysis of a crack in an infinite orthotropic sheet.

### EXPERIMENTAL STUDY

In order to examine the plastic zone at the crack tip in boron/aluminum, experiments were run with strain gages mounted at the crack tip. One test was on a crack along the fibers perpendicular to the load, and the other for a crack along the fibers at a  $60^\circ$  angle to the load. The data collected was reduced to the form of applied remote stress versus strain. The objective of this series of tests was to examine the plastic zone sizes and to observe the plastic zone growth during a 1.5 overload cycle.

### Tapered Specimens

A simple case of plastic zone growth was designed in the form of a tapered specimen (specimen 25) to test the setup and material modeling. Figure 48 shows the dimensions and the gage locations on the specimen. Quarter-inch grid strain gages were used for this test. The data acquisition setup is the same as shown in Figure 20.

Because of the special geometry required of the specimen, the diamond saw could not be used. The specimen was cut by electric discharge machining (EDM). The cut edge was found to be of superior quality to



that of the saw cut edge. However, although the specimen is immersed in oil during cutting, it is questionable whether or not the material edges are subject to excessive heating during the electric discharge machining.

The data from the tapered specimen can be found in Figures 33 and 34, for the longitudinal gages only. The data in Figure 33 is arranged as applied tensile load versus strain. As expected, the gage at the narrow end (gage 1) shows signs of yielding first, and the gage at the wider end (gage 6) displays yielding last. Thus, a progression of plastic zone is observed. (Gages 5 and 7 were placed front and back in the same location to check for bending. Both gages show similar strains.) The data was also reduced to the form of net section stress versus strain to see if the data generally collapsed onto the same line. Figure 34 shows the plot of this data, as well as results from a finite element modeling. The model data predicts larger strains for a given stress level or conversely, the tapered specimen appears to be more constrained than either the uniaxial specimen or the finite element model. The reason for the discrepancy appears to be due to the long high strength fibers extending from the elastic region into the plastic region. The main effect of these fibers is to inhibit the shear plastic flow and this is corroborated by Figure 34 which also shows a finite element modeling but with the shear coefficient changed from 1.8 to 1.5, and the agreement is very close.

The above result is important when considering the modeling of the crack tip in the orthotropic material because there is a substantial elastic constraint on the strains in the region of local yielding.

In other words, the yielded material is not allowed to flow as freely due to the strong fibers protruding into the plastic zone. It is clear that in order to account for this constraining effect either a finite element program which models the actual fibers is required, or some testing scheme for obtaining the 'r' parameters under constrained conditions be devised. The former seems too cumbersome, but the latter has potential if a tapered specimen is used in the fundamental test.

### Strain Gage Strips

The choice of resistance gages for measuring the strains at the crack tip was based on the need for ease and reliability of data acquisition. It was understood that the strain gages would be operating under the worst of circumstances: A steep strain gradient and the size of the plastic zone required very small gages, whereas normally the inhomogeneity would require large gages to average out the strains over a greater area. The gages purchased from Micro-Measurements, Inc. were in the form of a strip of ten gages, of alternating grid directions, type EA-13-031MH-120. The grid sizes of the gages were each .031" across, and the entire strip was on the order of only .7" long. The strip was cut into two sections, one of six gages and one of four gages. For each of the two tests these strips were placed on the X and Y axes relative to the crack tip. The sequence for mounting the gages was to first initiate a crack, then the gages were mounted a short distance away from the crack tip. The specimen was fatigued under a constant amplitude cyclic stress until the tip was close to the first gage grid. (Note that it aided the positioning of the gages to know that the crack would consistently travel in the fiber direction.)

### Study of Transverse Crack

Specimen 26 was prepared such that the applied stress would be perpendicular to the crack. The strain gages were mounted as shown in Figure 35 and the crack was grown into position so that during the overload cycle the gages were at the (X,Y) coordinates given.

The plots for gages 1, 3, 5, and the remote gage are shown together in Figure 36. (Note that gage 1, being right next to the crack tip, failed during the test.) The amount of plasticity recorded corresponds to the distance from the crack tip. It is expected that the yield stress at each gage should also correspond to the distance from the crack tip. Since it is evident that the apparent yield stresses for gages 1, 3, and 5 are all at 9400 psi (which is the maximum cyclic stress prior to the overload), it can be concluded that the material at these locations yielded prior to the 1.5 overload. Observe also that the remote gage shows some residual strains following the overload cycle. This indicates that the entire specimen has yielded in post overload to a small degree.

### Study of Oblique Crack

Specimen 27 was cut so that the crack would be at an angle of  $60^\circ$  to the applied stress. Figure 37 is a schematic of the specimen, giving geometry and (X,Y) gage coordinates prior to the 1.5 overload application.

Figure 38 shows the data for gages 1, 3, 5, and the remote gage. The maximum stress of the constant amplitude cycling was made lower for this test to avoid yielding the entire specimen as in the previous test. It can be observed from the remote gage that there is very little residual strain after the overload. Again, as expected, the amount of residual strains in gages 1, 3, and 5 correspond to the distance from the crack tip.

This time, however, the apparent yielding occurs at higher stresses the further the gage is from the crack tip. This indicates that the gages have recorded an expansion of the plastic zone during the overload.

#### APPROXIMATE ELASTIC-PLASTIC ANALYSIS OF CRACKS

A computer program was developed in order to obtain an estimate of the stresses around the crack tip in B/A1. This program was used to predict plastic zone shapes and sizes, and to give stress and strain predictions at arbitrary points around the crack tip.

##### A Crack in an Infinite Orthotropic Sheet

For an approximate crack analysis, a program was written which made use of the solutions for the elastic stresses (mode I and mode II) in an orthotropic sheet. Incorporated in the program is the effective stress yield criterion and the work hardening model. The expressions for the stresses were derived from the elastic solution of the stress distribution around an elliptical hole [Reference 5]. The tractions at the surface of the ellipse are required to be zero and the stresses at infinity are required to be the applied stress. The total stresses are the sums of two solutions, as shown.

$$\begin{aligned}\sigma_x &= \sigma_x' + \sigma_\infty \cos^2 \psi \\ \sigma_y &= \sigma_y' + \sigma_\infty \sin^2 \psi \\ \sigma_{xy} &= \sigma_{xy}' + \sigma_\infty \sin \psi \cos \psi\end{aligned}\tag{4.1}$$

where the sign convention and notations are shown in Figure 39.

The values  $\sigma_x'$ ,  $\sigma_y'$ , and  $\sigma_{xy}'$  are stresses resulting from the tractions on the ellipse. The crack solution is obtained by letting the minor axis

of the ellipse be equal to zero. In this limit, the stresses are related to the stress functions  $\phi_1$  and  $\phi_2$  by the equations

$$\sigma_x' = 2\text{Re}\{\mu_1^2 \phi_1 + \mu_2^2 \phi_2\}$$

$$\sigma_y' = 2\text{Re}\{\phi_1 + \phi_2\}$$

$$\sigma_{xy}' = -2\text{Re}\{\mu_1 \phi_1 + \mu_2 \phi_2\}$$

where  $\phi_1 = -A_{11}/\sqrt{z_1^2 - a^2}(1/\rho_1)$

$$\phi_2 = -A_{21}/\sqrt{z_2^2 - a^2}(1/\rho_2)$$

and  $A_{11} = \frac{\sigma_\infty}{2\Delta} \{a \sin \Psi (\cos \Psi + \mu_2 \sin \Psi)\}$

$$A_{21} = -\frac{\sigma_\infty}{2\Delta} \{a \sin \Psi (\cos \Psi + \mu_1 \sin \Psi)\}$$

and  $z_k = x + \mu_k y$   $\rho_k = (z_k \pm \sqrt{z_k^2 - a^2})/a$   $\Delta = \mu_1 - \mu_2$  (4.2)

The singular stresses could be derived from these expressions by taking the limit of the distance from the crack tip to be much less than the crack length ( $r \ll a$ ). In this case,  $\rho_k \rightarrow 1$  and

$$z_k = x + \mu_k y = a + r \cos \theta + \mu_k r \sin \theta$$

so that  $\sqrt{z_k^2 - a^2} \rightarrow \sqrt{ar(\cos \theta + \mu_k \sin \theta)}$

This gives the near-tip solution with  $\sqrt{r}$  singular stresses at the crack tip for mode I and mode II. The program, however, does not make this approximation, and will be referred to as ELLPLAS.F.

Using the  $r$ -values and the elastic constants obtained for boron/aluminum, the plastic zone shapes were plotted for fibers running parallel to the crack and perpendicular to the crack. These plots are found in Figures 40 and 41. By comparison, the program was also made to

output the plastic zone shape for an isotropic material as shown in Figure 42. Each zone was calculated for the same remote stress (applied perpendicular to the crack) and the same crack length. The zone shape resulting from the fibers being perpendicular to the crack is worth noting.

The effect of changing the loading angle with respect to the crack can be observed in Figures 43 through 45. In each plot the fibers are parallel to the crack. Starting with the load perpendicular to the crack, it is shifted to  $60^\circ$  and then to  $30^\circ$ . The zone shape changes as mode II becomes predominant, and the size of the zone shrinks as the load approaches  $0^\circ$  (parallel to the crack) where no singular stresses would be observed.

#### Reconsidering the Strain Gage Results

An estimate of the plastic zone corresponding to the transverse crack test can be seen in Figure 41. The correct crack length of .31" was used, and of the two remote load levels, the 9400 psi zone size corresponds to the maximum cyclic stress. The load level of 14100 psi corresponding to the peak overload stress was not used to give a zone size because it was found to yield the entire specimen. To better illustrate the problem, the same program was used to plot the effective stress versus the distance from the crack tip. Figures 46 and 47 are for the X and Y axes respectively, and each plot also shows the locations of the strain gages. Where the effective stress line crosses the effective yield stress line is the boundary for the plastic zone. From the figures it can be observed that only half of the strain gages are predicted to be in the plastic zone for the stress level prior to the overload. This indicates that the approximation underestimates the plastic zone size,

since the experimental results show that the material at each gage location has yielded before the overload cycle. The prediction of a smaller zone size is to be expected, since the approximation only gives an elastic solution; a redistribution of the stresses due to the yielded material would result in larger predicted zone sizes. This effect is enhanced further since the real specimen has a finite width. For the peak overload stress the approximation predicts that the whole specimen yields, as can be seen in the two figures.

An estimate of the plastic zones for the oblique crack test is shown in Figure 44. Again, to better illustrate the effective stress distribution, Figures 48 and 49 were produced similar to Figures 46 and 47. Unlike the previous test, the plastic zone has a finite size for the peak overload stress, yet the estimates show that each gage should have detected some yielding during the overload cycle.

#### DISCUSSION OF PLASTICITY EFFECTS AND FATIGUE

The major point observed in the fatigue tests mentioned in Chapter 1 are the tendency for the crack to always grow along the fibers. The tests conducted in this chapter offer some insight into these phenomena.

Regarding the crack growth direction, the plastic zone shapes predicted by the approximate analysis give an indication of why it was found to be difficult to grow fatigue cracks through the fibers in B/A1. Figure 40, which shows the plastic zone extending primarily perpendicular to the crack tip, indicates that the crack would be prone to turning and travelling along the fibers.

## CONCLUSIONS

The clip gage used in this work was found to be a good way to determine the longitudinal and transverse strains in a coupon specimen, but it is recommended that specimen dimensions be confined to those for which the gage is designed to avoid recalibration inaccuracies.

For cutting the specimens the diamond saw was adequate as long as the cuts were straight and the specimens were not required to have sharp notch cuts. The electric discharge machining (EDM) technique is capable of cutting any shape of specimen providing an electrode of that shape can be made. The cutting is relatively fast and flawless, although not necessarily as accurate with regard to specimen fiber orientation.

Off-axis specimens should be cut with sufficient length-to-width ratios to avoid end effects if uniaxial testing is intended. As the angle between the loading direction and the fiber direction becomes smaller, there is a need for larger length-to-width ratios. A ratio of 12 was found to be adequate up to an angle of  $20^\circ$ . At  $10^\circ$  the end effects begin to be noticed, as indicated by the data presented in Figure 28. The elastic moduli measured for the  $10^\circ$  specimens (both specimen 5 and specimen 22) were consistently higher than the moduli calculated for the  $0^\circ$  specimens. In Reference [1] it is stated that a length-to-width ratio of 14 or higher be used at a fiber orientation of  $10^\circ$ .

From the discussion in Chapter 1 it was found that the  $10^\circ$  off-axis tensile specimen is not optimal for determining the intralaminar shear of a mildly orthotropic material such as boron/aluminum. The elastic orthotropic characterization given in Chapter 2 requires several tests (4 at least). It is recommended that a specimen of



suitable orientation (determined from the normalized strain versus fiber angle curve) be used if an off-axis test is to be performed.

Without doubt, the uniaxial behavior of boron/aluminum can be described within an anisotropic elastic plastic formulation. Two crucial questions remain to be answered. First, what is the behavior of the material under complex loading (including compressive stresses.) Secondly, (and perhaps more importantly) to what extent does the inhomogeneity of the material affect the plastic flow in situations of constrained yielding? Both of these questions can be clarified only after more complicated testing. And to design such tests will require a finite element program capable of solving orthotropic elastic plastic problems.

The application of strain gage strips to determining the plastic strain behavior in the vicinity of cracks appears very promising.

#### LIST OF REFERENCES

- [1] Chamis, C. and Sinclair, J.H., "Ten-deg Off-axis Test for Shear Properties in Fiber Composites", *Exp. Mech.*, pp. 339-346, September 1977.
- [2] Schoutens, J.E. and Tempo, K., Introduction to Metal Matrix Composite Materials, DOD Metal Matrix Composite Information Analysis Center, MMC No. 272, pp. 7-22, 1982.
- [3] Jones, R.M., Mechanics of Composite Materials, Scripta Book Company, Washington, D.C., pp. 32-54, 1975.
- [4] Kackanov, L.M., Fundamentals of the Theory of Plasticity, Mir Publishers, Moscow, pp. 60-97, 1974.
- [5] Lekhnitskii, S.G., Theory of Elasticity of an Anisotropic Body, Mir Publishers, Moscow, pp. 139-179, 1981.

Table 1. A comprehensive listing of B/A1 specimens cut from panel 1 as shown in Figure 1.

Specimen and Fiber Angle		Dimensions in inches (t x w x l)	Notch Cut, (in)	Use
1	0°	.077 x 3.0 x 9.5	.166 .315 .74	Fatigue
1a	0°	.077 x 1.92 x 9.5	.74	Fatigue
1b	0°	.077 x 1.05 x 9.5	.122 .281	Fatigue
2	15°	.077 x 1.65 x 10.	.465	Fatigue
3	0°	.077 x 1.517 x 9.5	.612	Fatigue + 1.5 Overload
4	0°	.077 x 1.51 x 9.5	.598	Fatigue + 1.5 Overload
5	10°	.077 x 1.005 x 8.6	----	
6	0°	.077 x 1.00 x 6.5	----	
7	0°	.077 x 1.011 x 10.	----	Material
8	90°	.0775 x 1.00 x 9.8	----	Properties
9	90°	.0775 x 1.006 x 9.8	----	
10	90°	.077 x 3.08 x 9.5	.148	Fatigue
11	90°	.077 x 3.08 x 9.5	.150	Fatigue + 1.5 Overload
12	90°	.077 x 3.061 x 9.7	.136	Fatigue + 1.5 Overload
13	90°	.077 x 3.07 x 9.7	.142	Fatigue + Fracture
14	0°	.078 x 1.52 x 9.5	.290	Fracture
15	0°	.077 x 1.51 x 9.5	.571	Fatigue Threshold

Table 2. Mechanical properties of B/Al (tensile, room temperature).

EXPERIMENTAL		REPORTED [Ref. 2]
<u>Elastic Constants</u>		
$E_1$	30.3 ksi, 32.6 ksi	31 ksi
$E_2$	20.3 ksi, 20.8 ksi	20 ksi
$G_{12}$	7.55 ksi	6 ksi
$\nu_{12}$	.29	.23
$\nu_{21}$	.21, .37	.13
<u>Ultimate Stresses</u>		
$\sigma_1$	204 ksi, 222 ksi	216 ksi
$\sigma_2$	26.5 ksi, 27.0 ksi	20 ksi
<u>Yield Stresses, Observed Yielding</u>		
$\sigma_1$	none	
$\sigma_2$	14.5 ksi, 15.6 ksi	
<u>Yield Stresses, .05% criterion</u>		
$\sigma_1$	170 ksi	
$\sigma_2$	15.6 ksi, 16.8 ksi	

Table 3. A comprehensive listing of B/A1 specimens cut from panel 2 as shown in Figure 27.

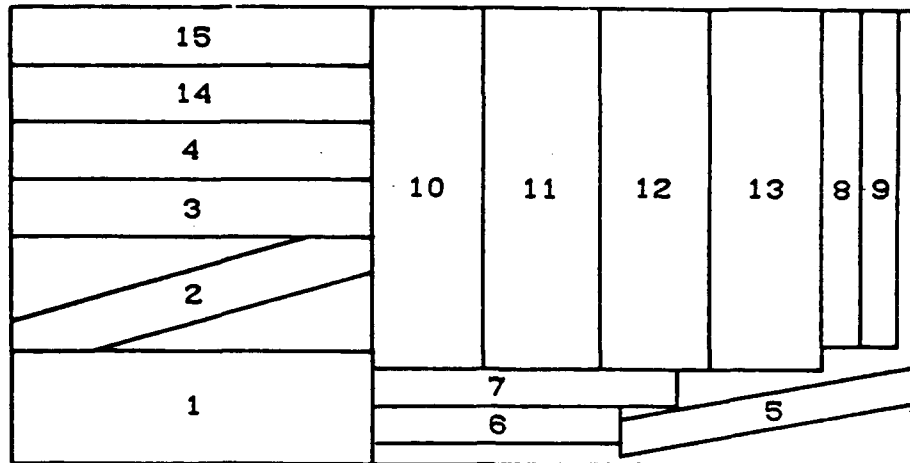
Specimen and Fiber Angle		Dimensions in inches (t x w x l)	Notch Cut, (in)	Use
16	0°	.0760 x .521 x 9.0	----	
17	30°	.0780 x .502 x 10.0	----	
18	45°	.0780 x .527 x 9.0	----	
19	60°	.0780 x .524 x 9.0	----	
20	90°	.0780 x .538 x 9.3	----	Elastoplastic Characterization
21	0°	.0775 x .500 x 9.0	----	
22	10°	.0770 x .443 x 9.0	----	
23	20°	.0780 x .465 x 8.0	----	
24	65°	.0780 x .481 x 9.0	----	
25	45°	.0780 tapered specimen	----	Preliminary plastic zone test
26	90°	.0775 x 2.950 x 9.8	.163	Plastic zone Measurements
27	60°	.0775 x 2.950 x 9.5	.312 at 60°	Plastic zone Measurements

Table 4. Mechanical properties of B/Al (tensile, room temperature) obtained from tests outlined in Chapter 3 conducted on specimens 17 through 24.

Fiber Angle	Elastic Modulus (msi)	Elastic Poisson's Ratio	Plastic Poisson's Ratio	Ultimate Stress (ksi)	Yield Stress (ksi)
0°	27.05	.232	.577	202.1	none
10°	31.54	.213	.832	70.4	36.1
20°	26.96	.278	.757	51.6	19.7
30°	20.86	.287	.700	34.2	12.1
45°	15.99	.260	.646	25.2	12.7
60°	19.18	.164	.400	17.6	9.0
65°	20.77	.656	.393	16.8	11.7
90°	18.22	.157	.004	22.2	10.9

Table 5. A summary of the failure modes and ultimate longitudinal failure strains for specimens 17 through 24.

<u>Specimen Orientation</u>	<u>Failure Mode</u>	<u>Failure Strain</u>
0°	middle	.0068
10°	end	.0060
20°	middle	.0617
30°	middle	.0333
45°	middle	.0336
60°	end	.0078
65°	end	.0039
90°	middle	.0105



FIBER DIRECTION

SIZE: 12" x 24" x .077"

MATRIX / FILAMENT: 6061 Al / 5.6 B

11 PLIES, UNIDIRECTIONAL

VOLUME FRACTION: 47.5% Fibers

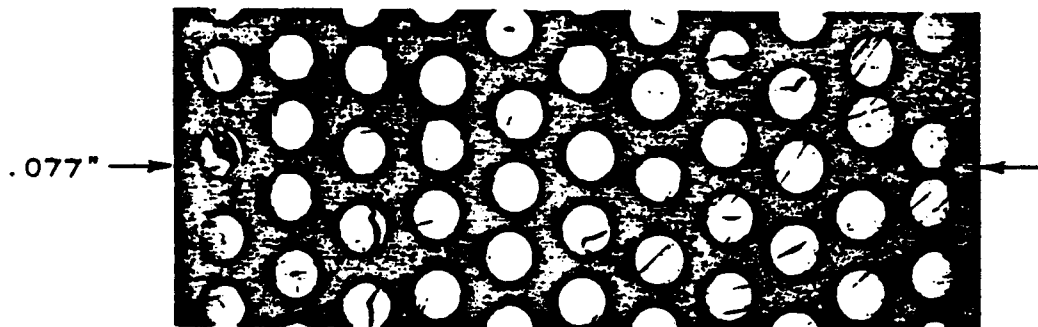


Figure 1. Specimen cutting plan for B/A1 panel 1. A photograph of the magnified cross section shows the 11 ply thickness. The section was cut with a diamond saw and then polished. Note that several fibers have cracked ends.



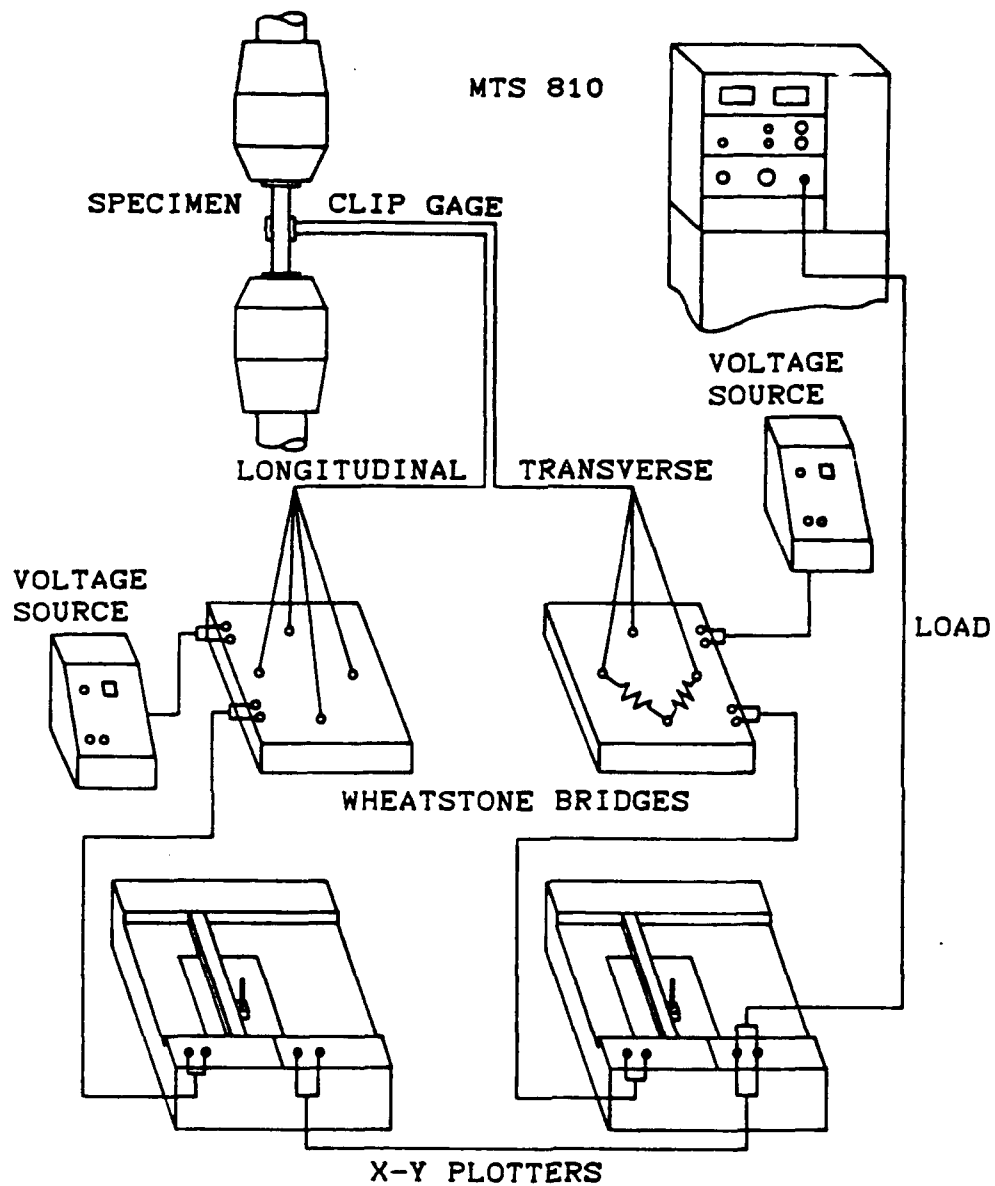


Figure 2. Schematic for mechanical properties testing. Load versus strain histories were recorded on X-Y plotters.

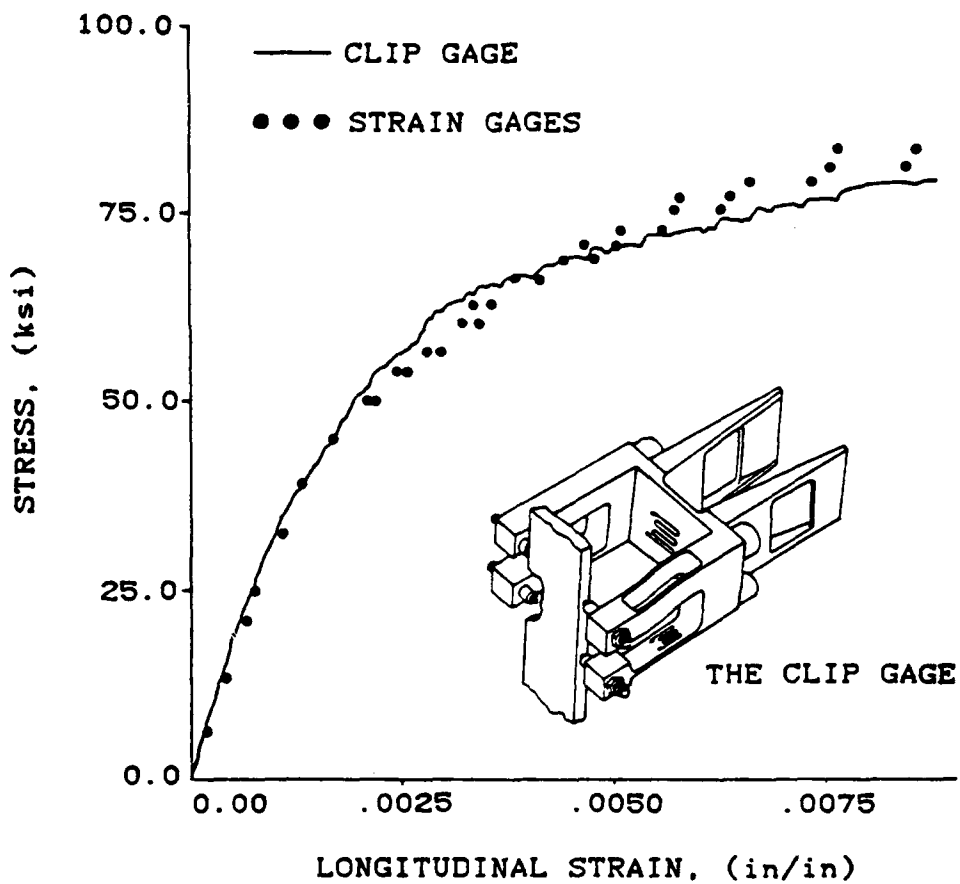


Figure 3. Results of comparison test between strain gages and the clip gage. This data was taken from B/A1 specimen 5.

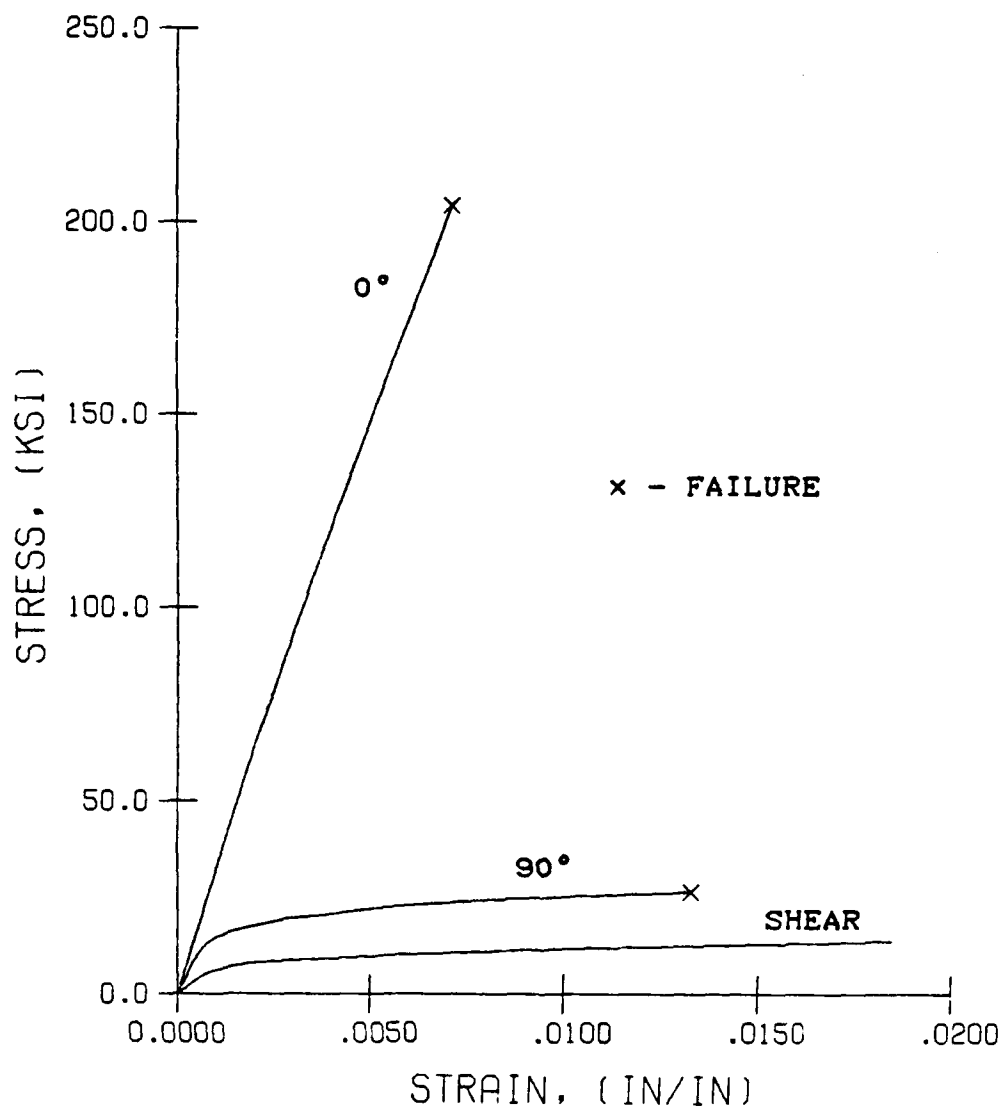


Figure 4. Typical stress-strain behavior obtained for B/Al principal material directions .

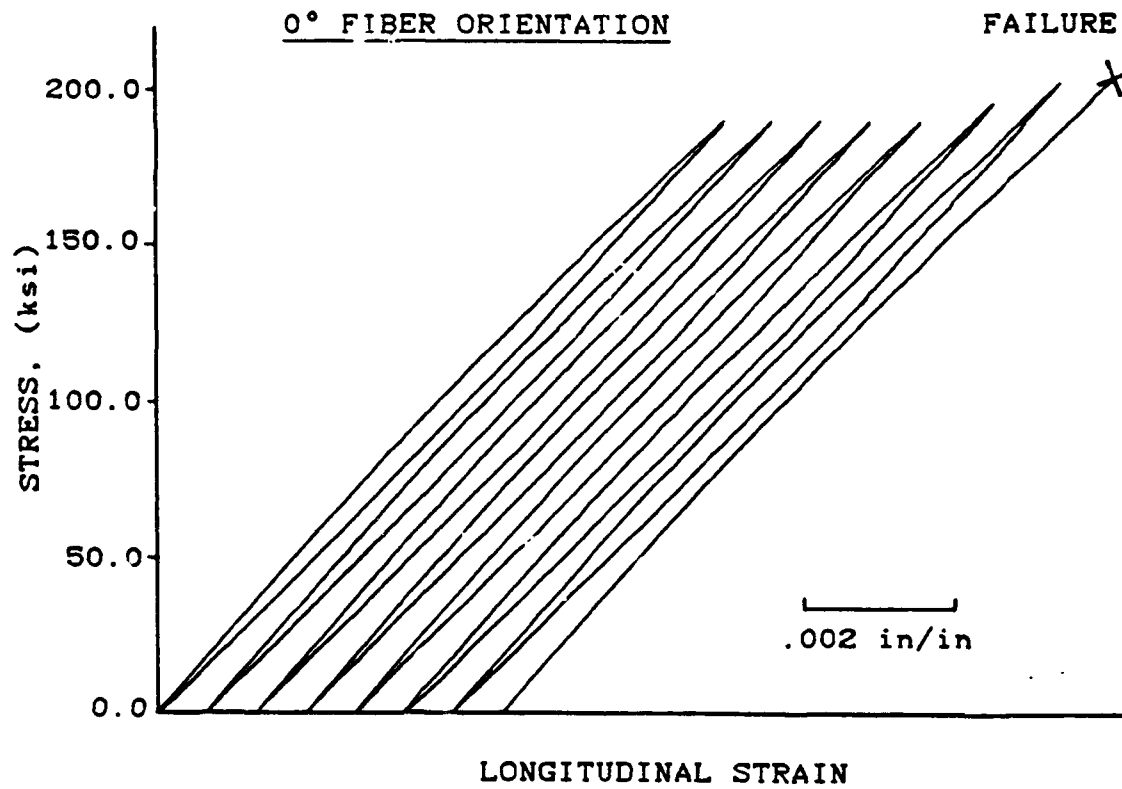


Figure 5. Last eight load/unload cycles for B/A1 specimen 7. Each cycle is spaced apart for clarity. Note the lack of residual strain when unloaded. The specimen failure is indicated by the x-mark

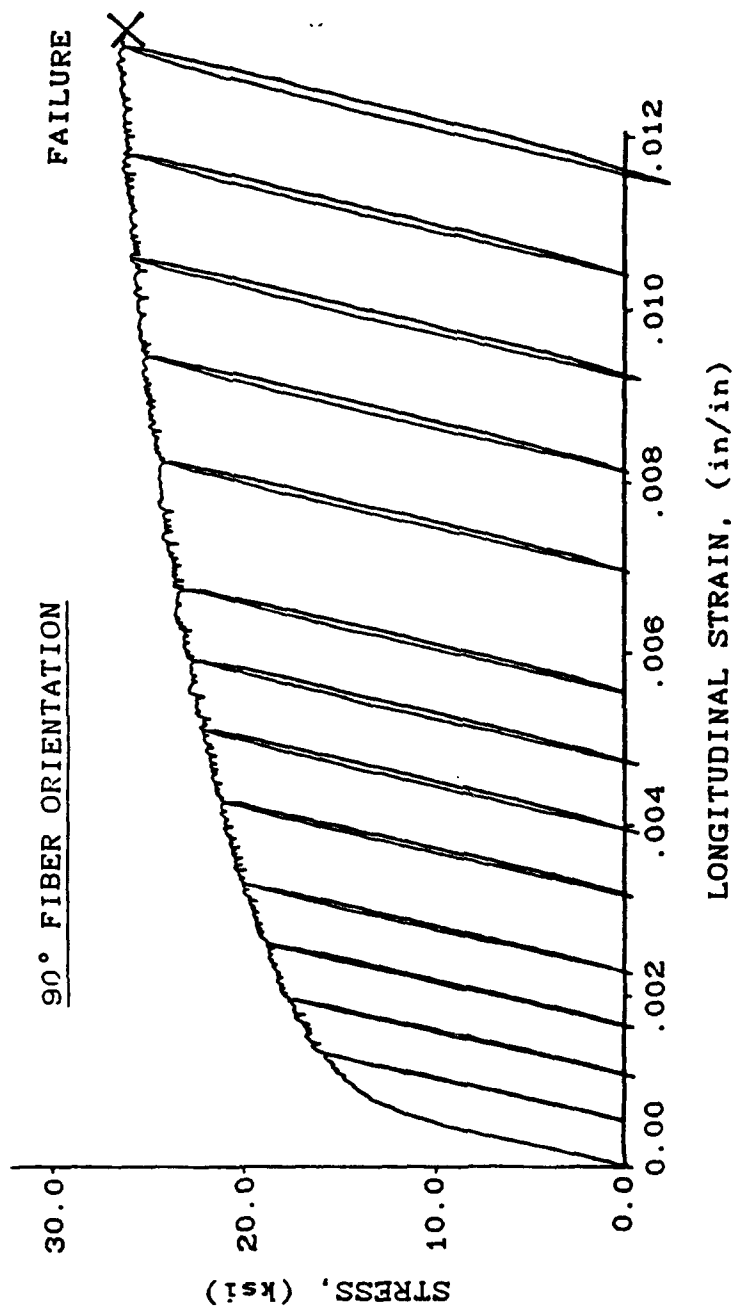


Figure 6. Stress-strain history of B/A1 specimen 8 with periodic unloadings. The specimen failure is indicated by the x-mark

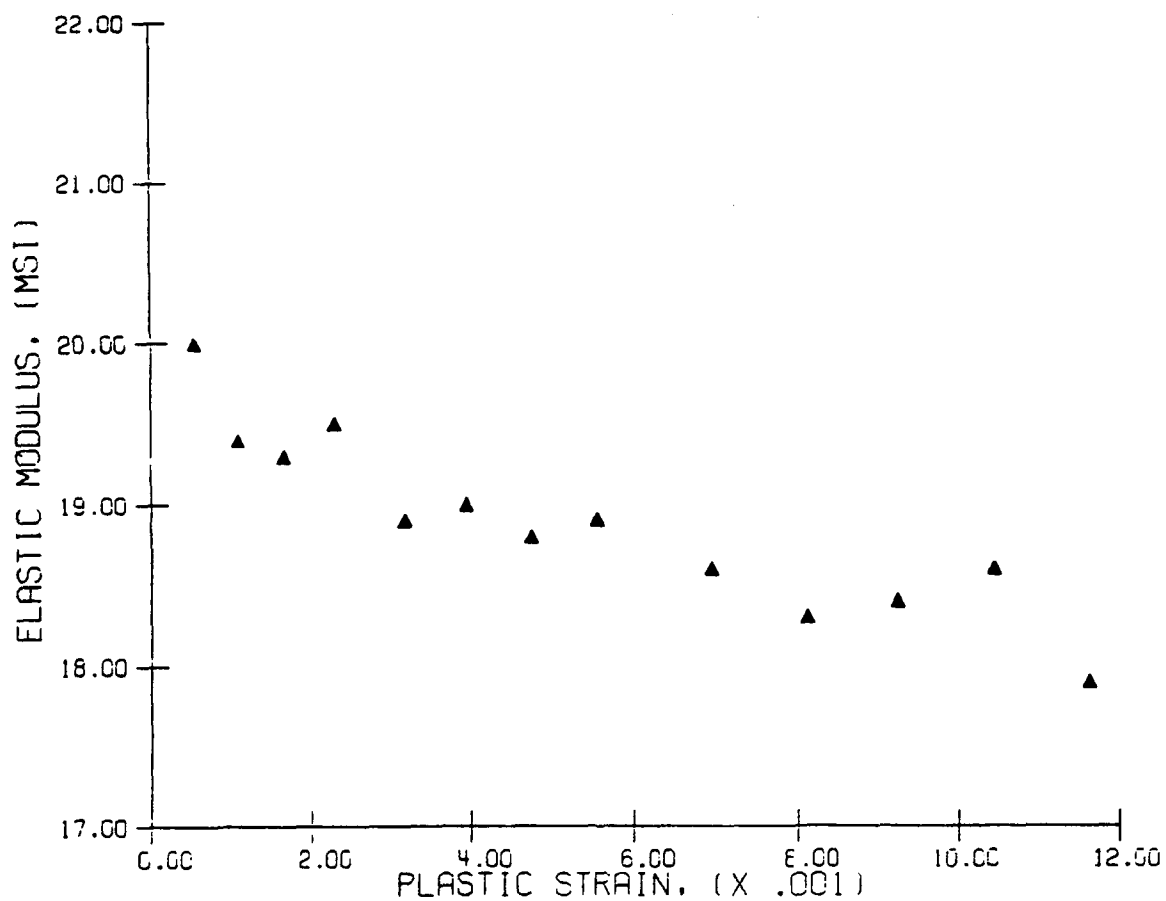


Figure 7. Elastic modulus versus plastic strain data taken from specimen 8. The modulus is observed to decrease substantially with increasing plastic strain. See Figure 6

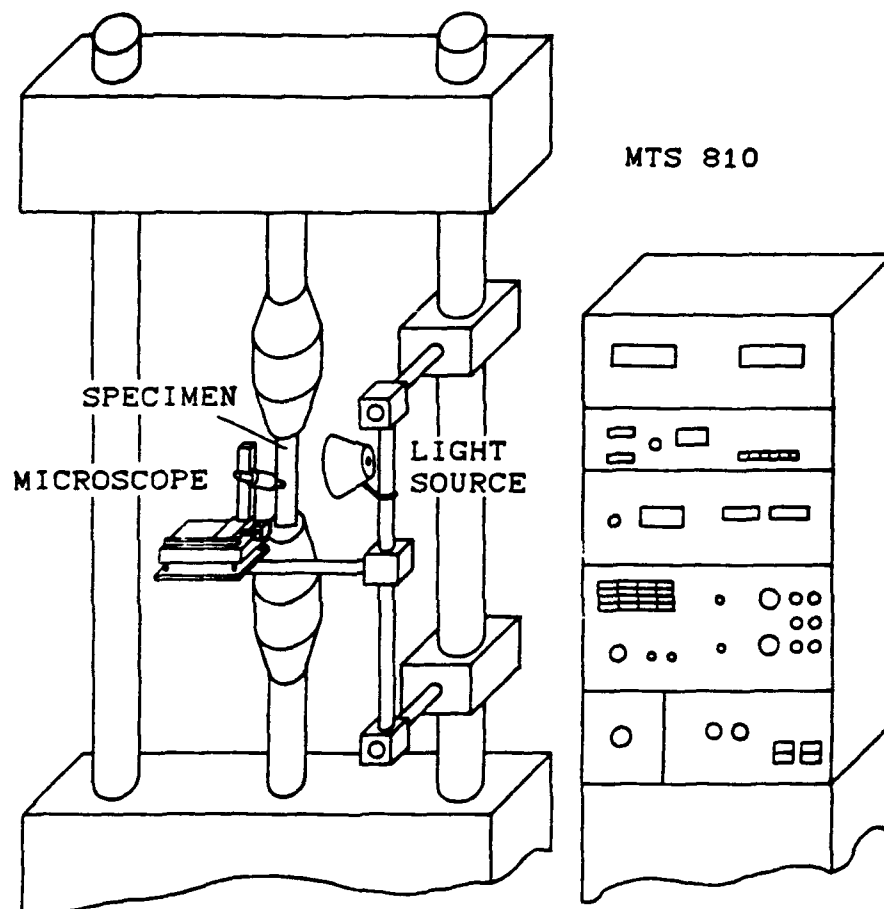


Figure 8. Schematic for fatigue testing. A travelling microscope was used to observe and measure fatigue crack growth.

# CRACK INITIATION IN SPECIMEN 1

0° B/Al 3.0" Wide Notch cut: .166"

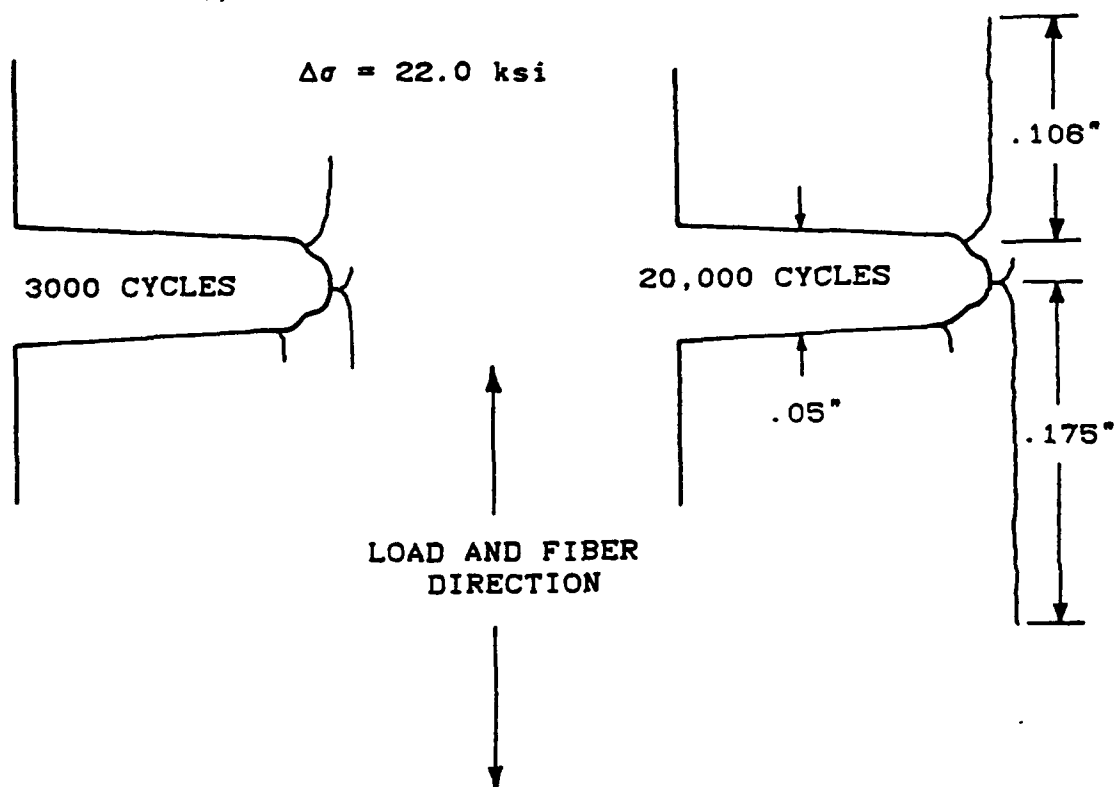


Figure 9. Schematic representation of cracks in B/Al emanating from the notch tip and propagating parallel to the fibers.



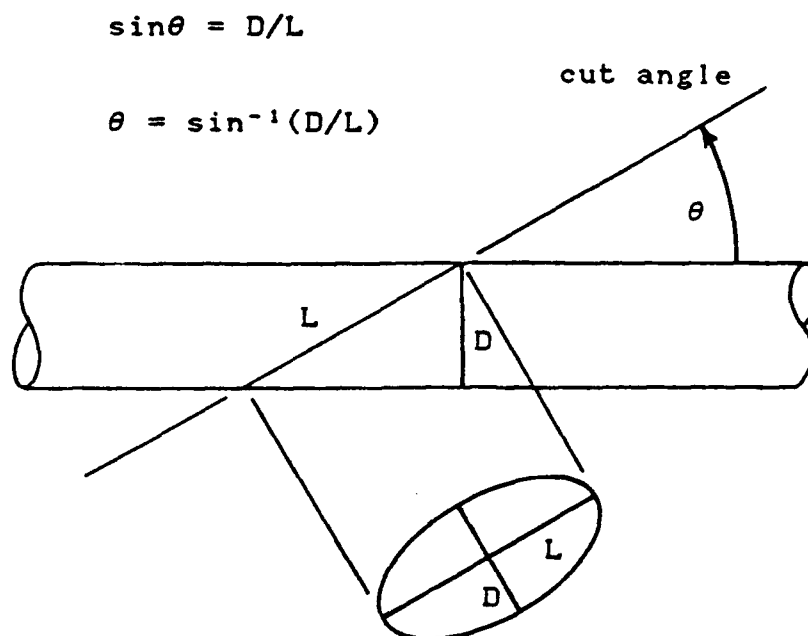


Figure 10. Schematic of how the fiber angle is determined from the exposed specimen edge after cutting

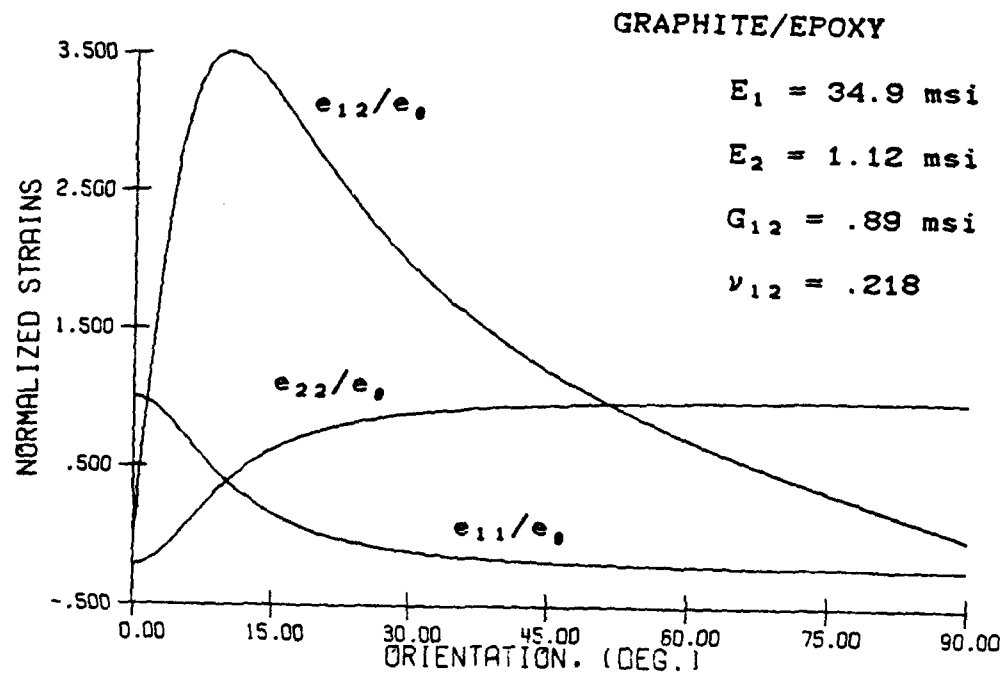


Figure 11. Normalized strain versus fiber orientation for a typical graphite/epoxy composite. The normalized shear strain peaks around  $10^\circ$ .

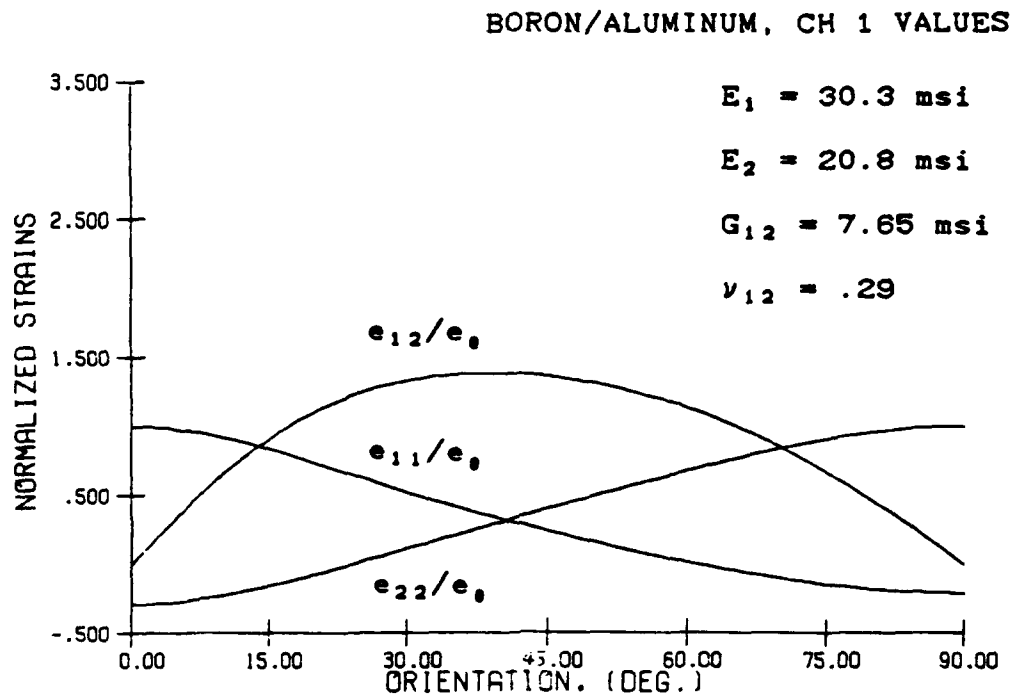


Figure 12. Normalized strain versus fiber orientation for B/Al.  
The normalized shear strain peaks around 40°.

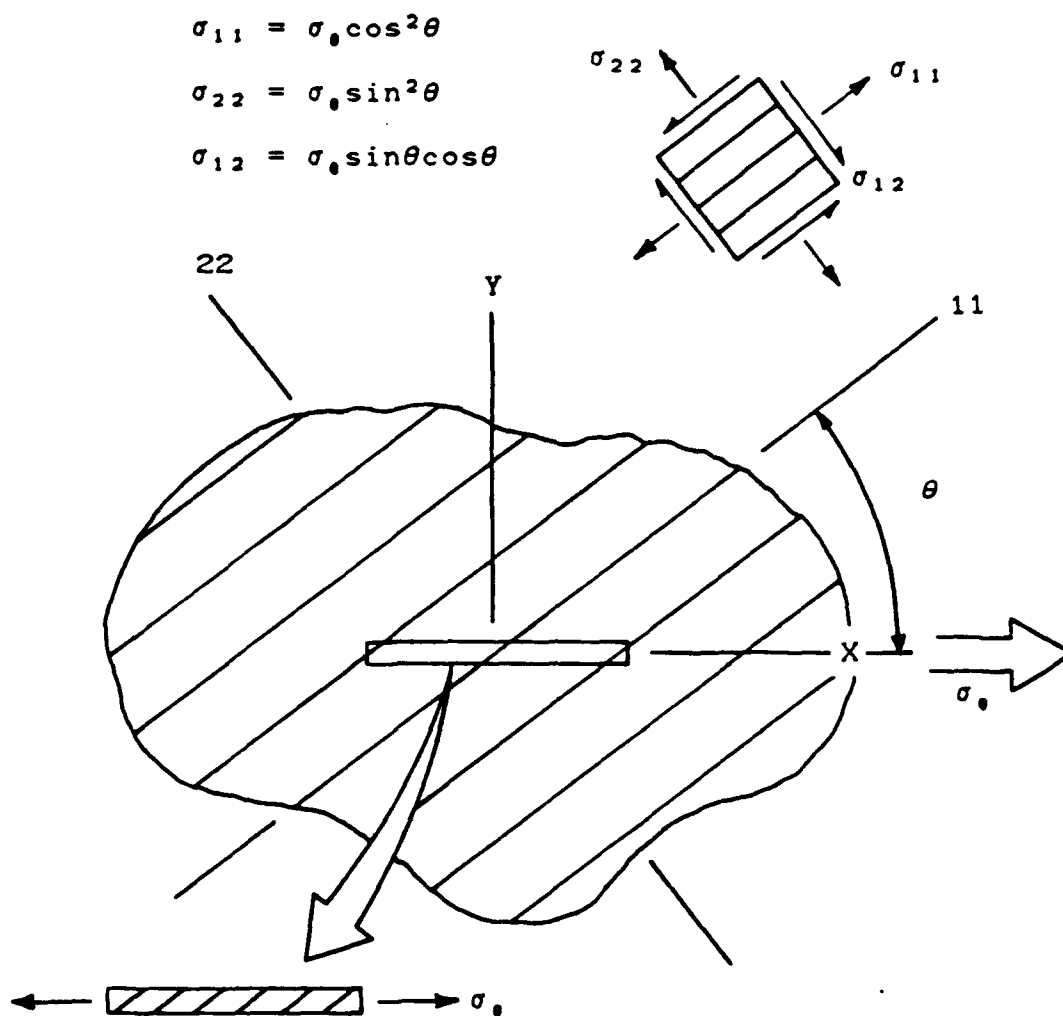


Figure 13. Illustration of a uniaxial specimen cut at an arbitrary angle to the principal material directions.

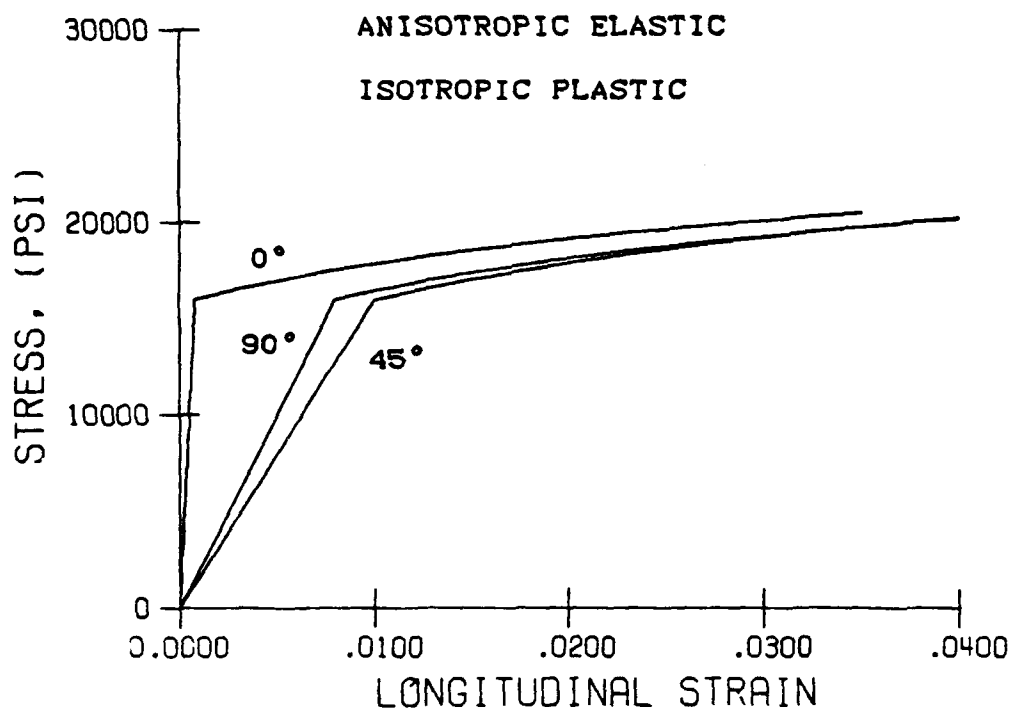


Figure 14. Stress-Strain curves for a hypothetical material with anisotropic elastic and isotropic plastic behavior, generated with the UNIAX.F program.

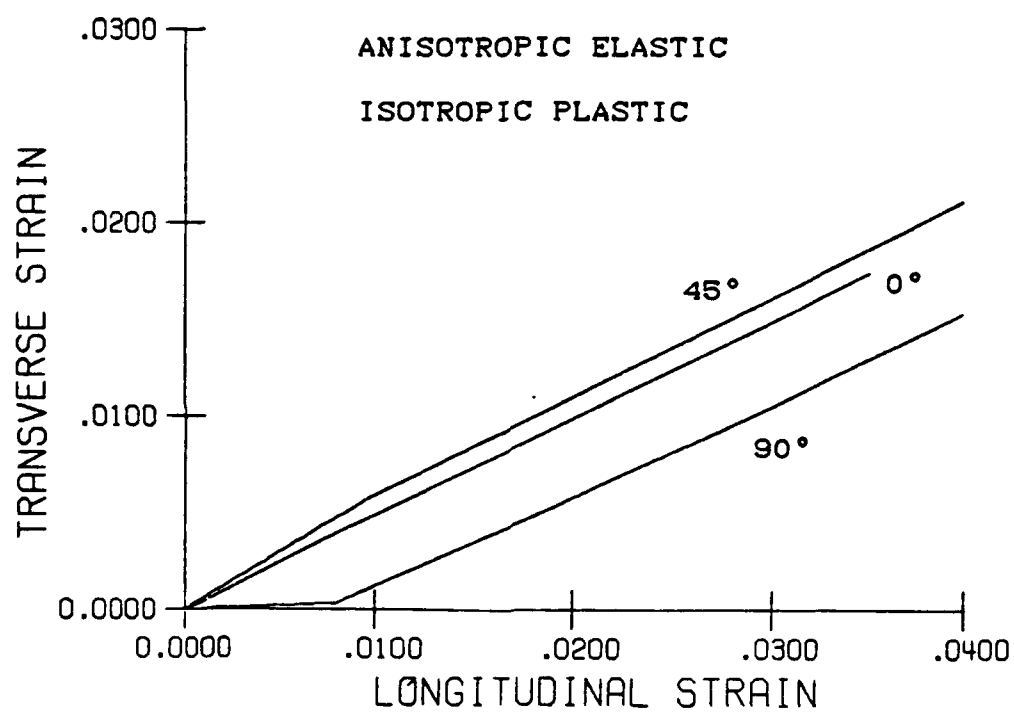


Figure 15. Transverse versus longitudinal strains for a hypothetical material with anisotropic elastic and isotropic plastic behavior, generated with the UNIAX.F program

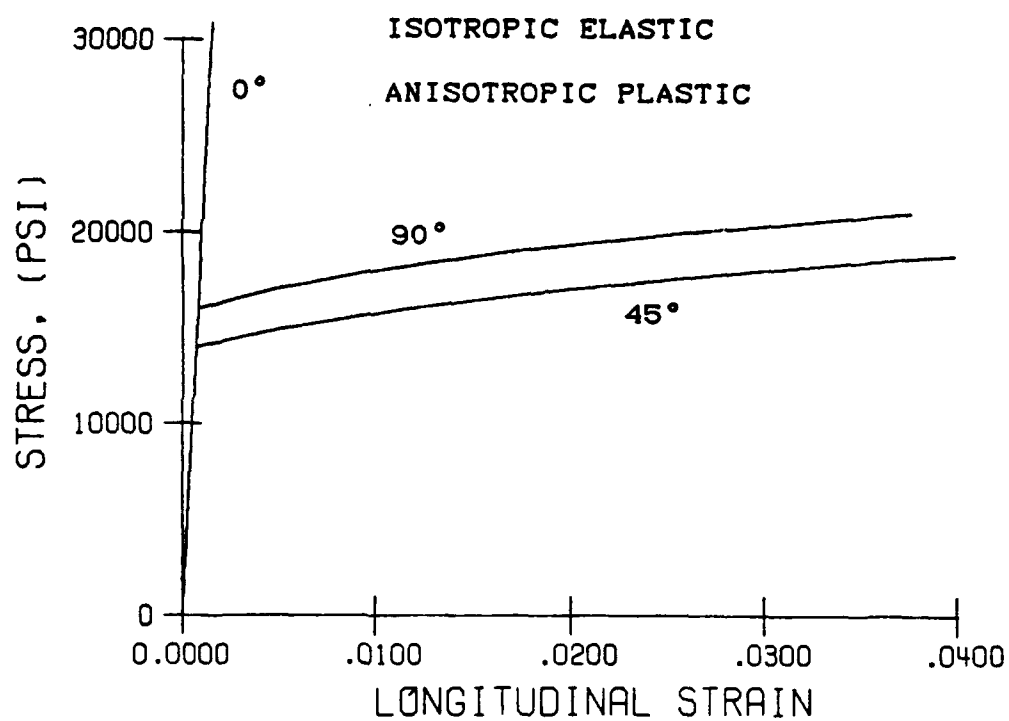


Figure 16. Stress-strain curves for a hypothetical material with isotropic elastic and anisotropic plastic behavior, generated with the UNIAX.F program.

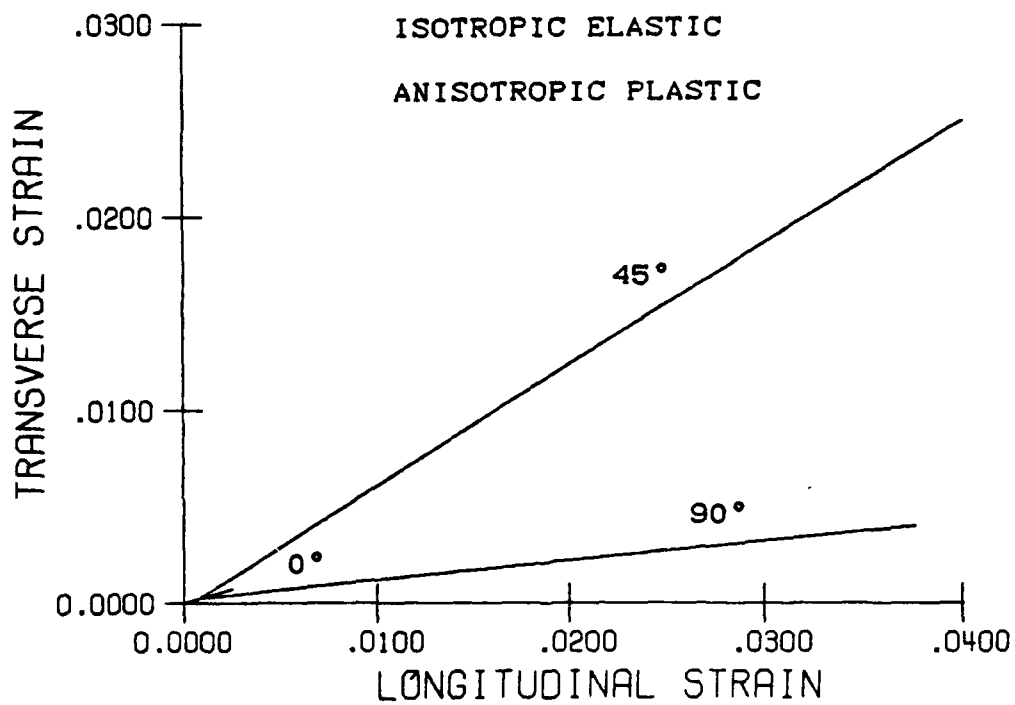
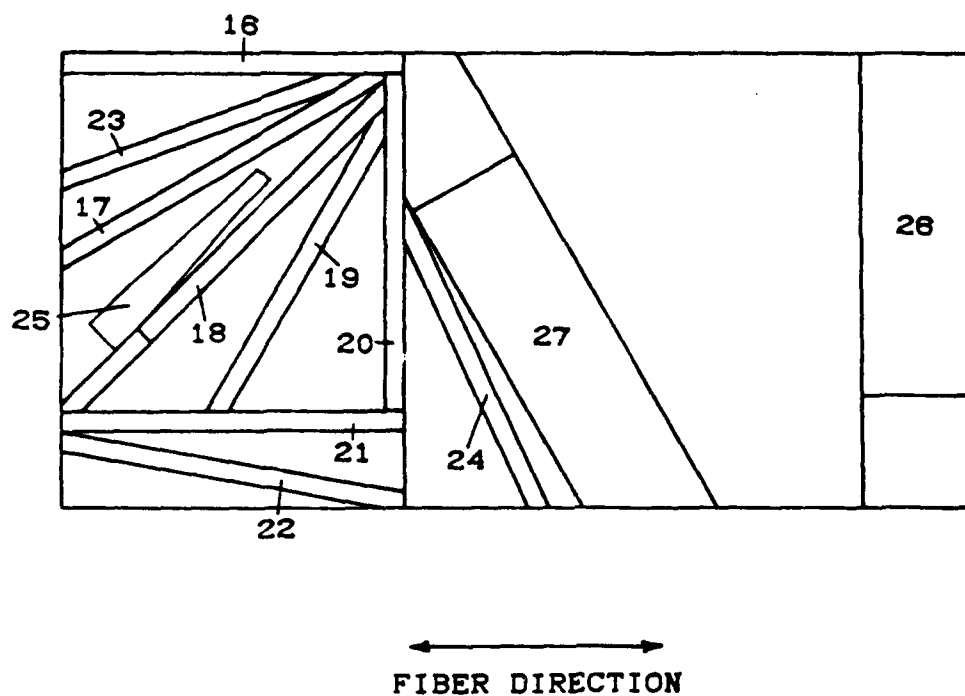


Figure 17. Transverse versus longitudinal strains for a hypothetical material with isotropic elastic and anisotropic plastic behavior, generated with the UNIAX.F program.





SIZE: 12" x 24" x .077"

MATRIX / FILAMENT: 6061 Al / 5.6 B

11 PLIES, UNIDIRECTIONAL

VOLUME FRACTION: 47.5% Fibers

Figure 18. Specimen cutting plan for B/Al panel 2.

COUPON SPECIMENS

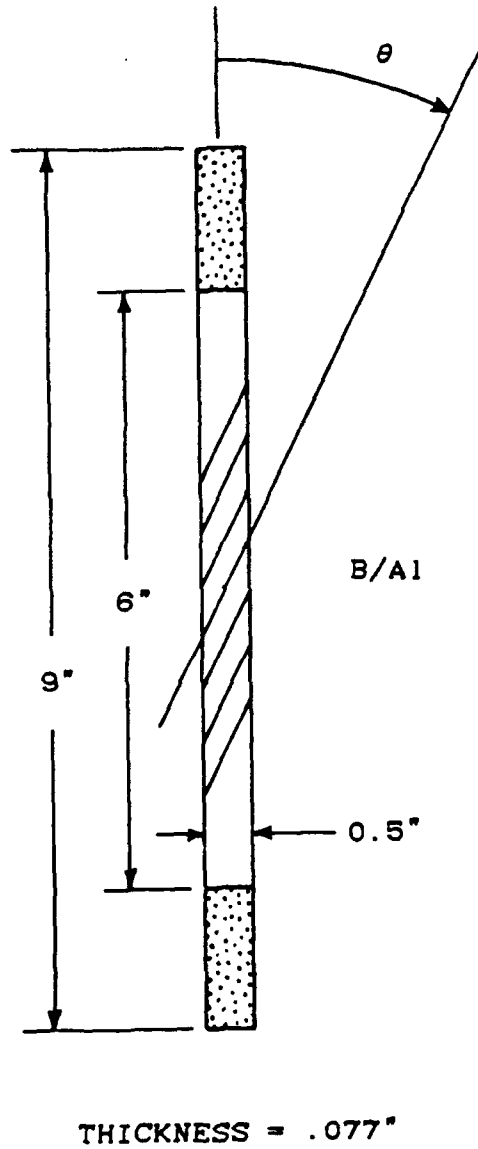


Figure 19. Illustration of a typical coupon specimen used in the tests outlined in Chapter 3

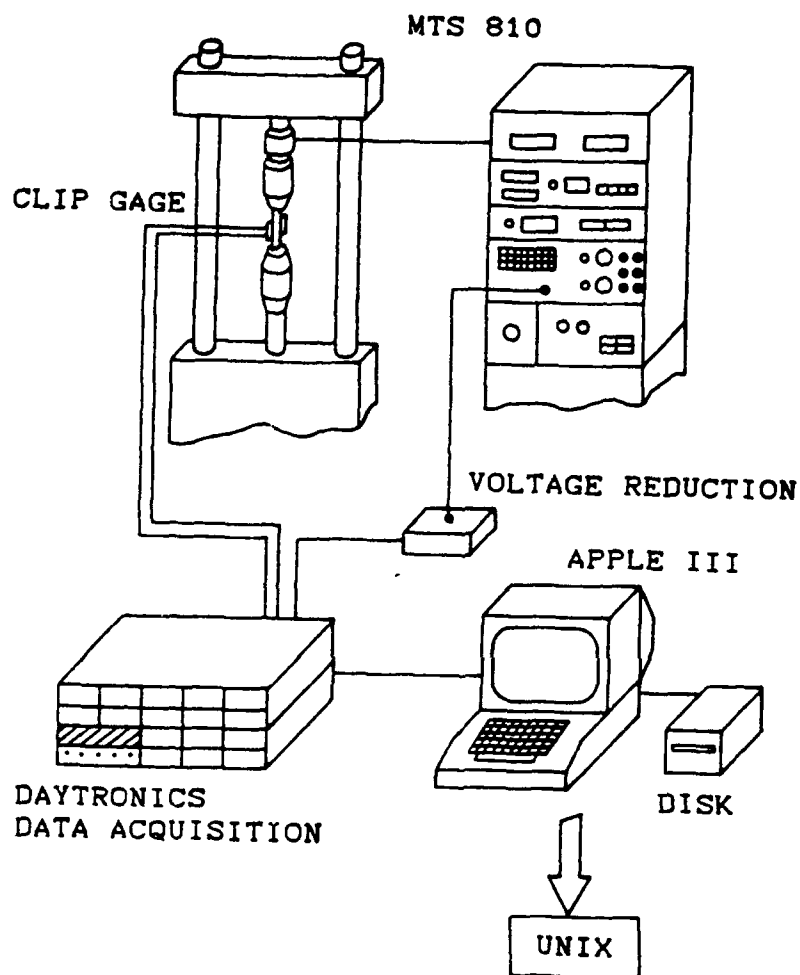


Figure 20. Schematic of the test setup with data acquisition system.

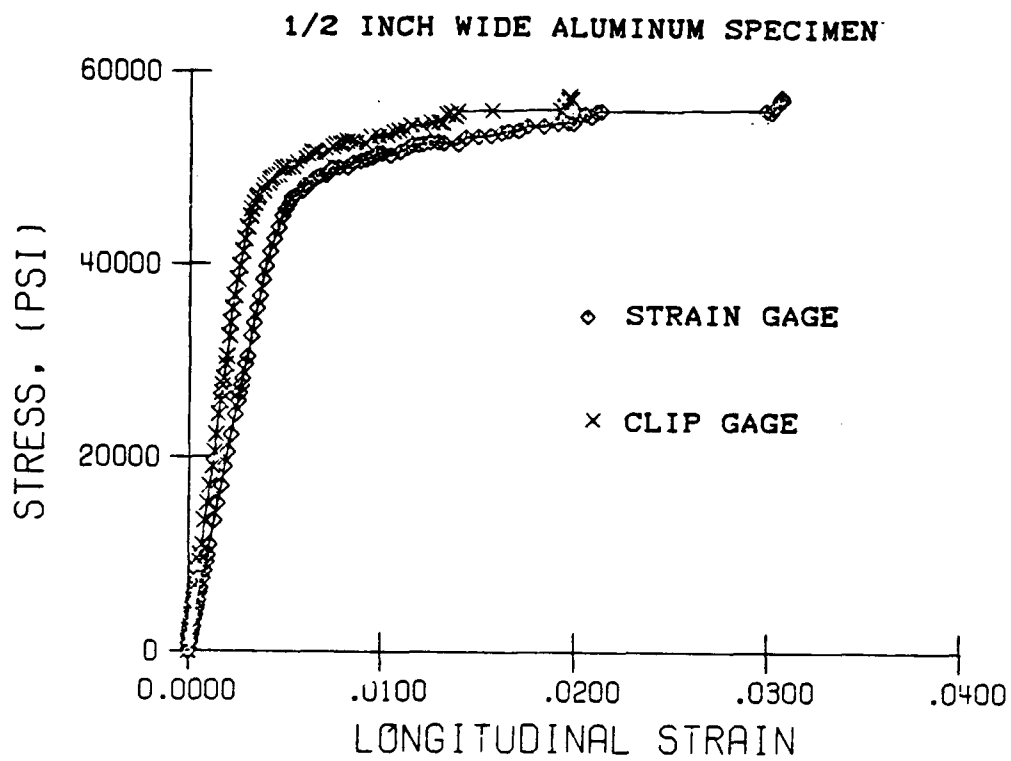


Figure 21. Stress versus strain data for clip gage calibration for half-inch wide specimens. Calibration was conducted on an aluminum specimen with known material properties.

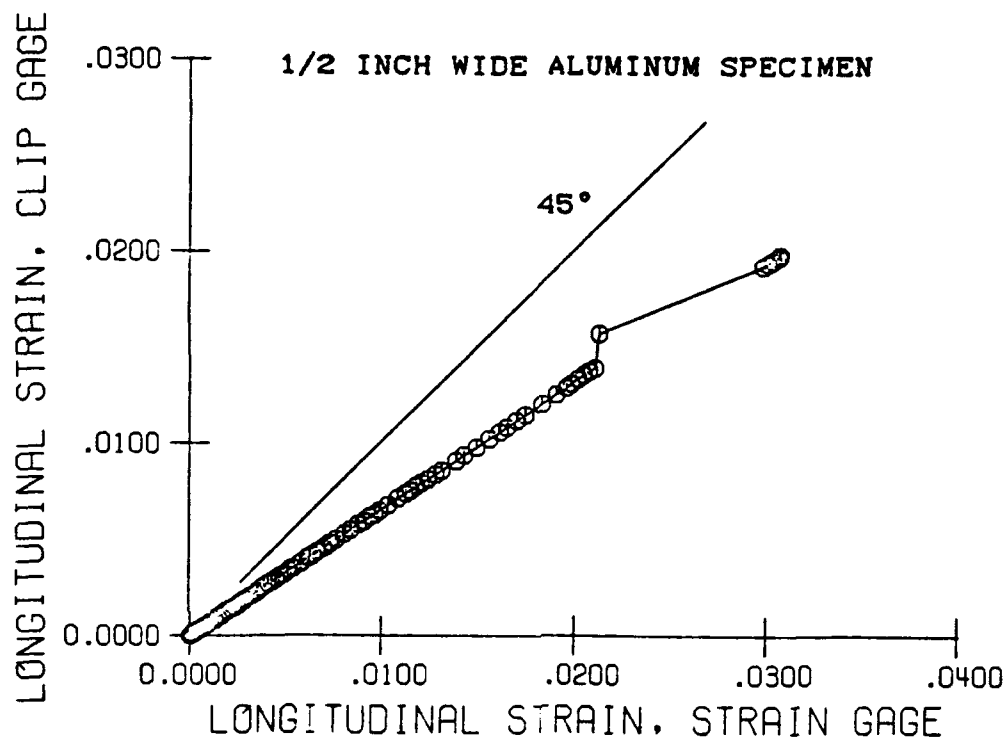


Figure 22. Clip gage strain versus strain gage strain data from Figure 21. This plot shows the linear relation between the two strains even in the post-yield region. The plot deviates from the expected 45° line, indicating that a calibration factor is required.

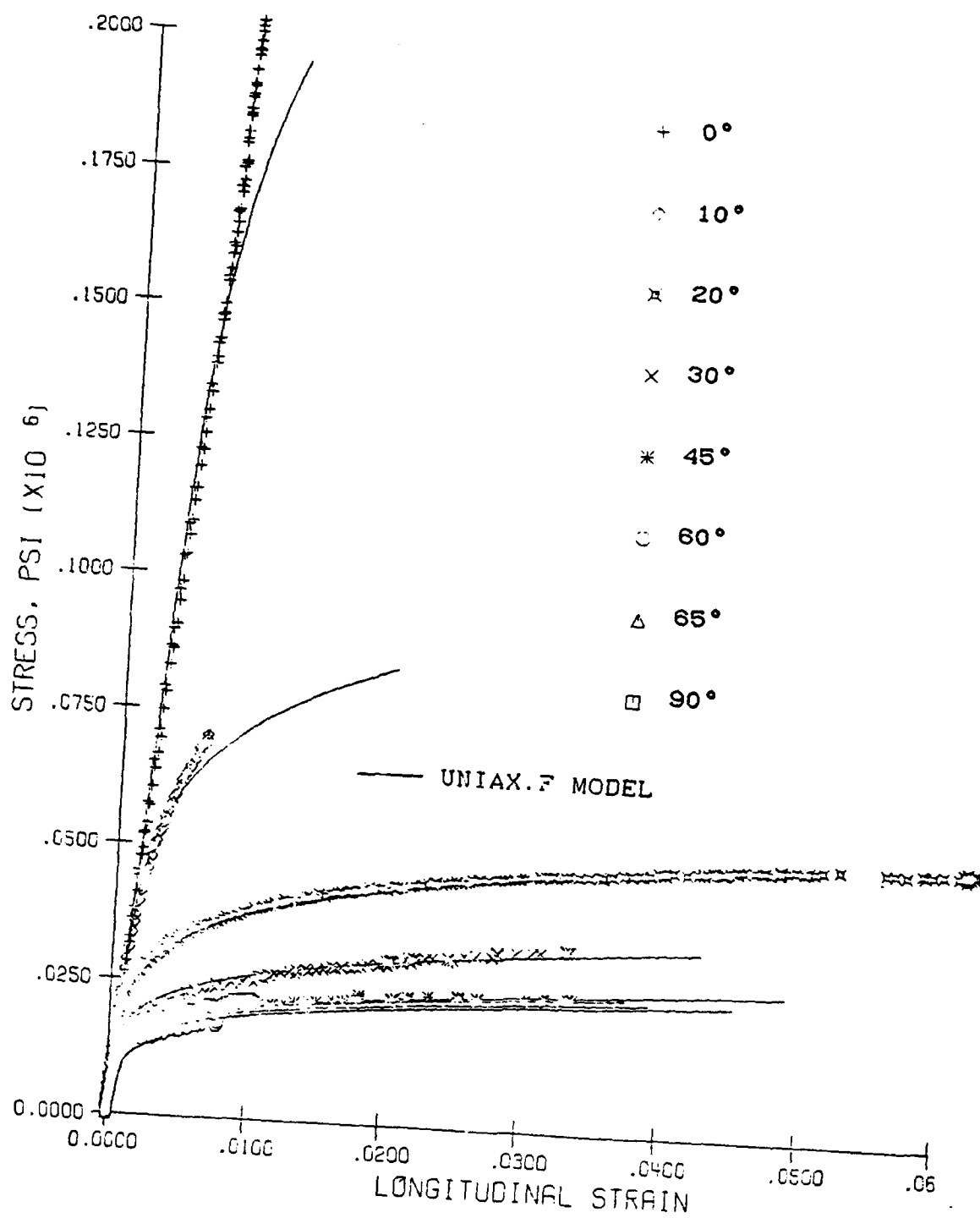


Figure 23. Stress versus longitudinal strain for various fiber orientations, B/A1. The solid lines indicate the computer modeling of the experimental data.

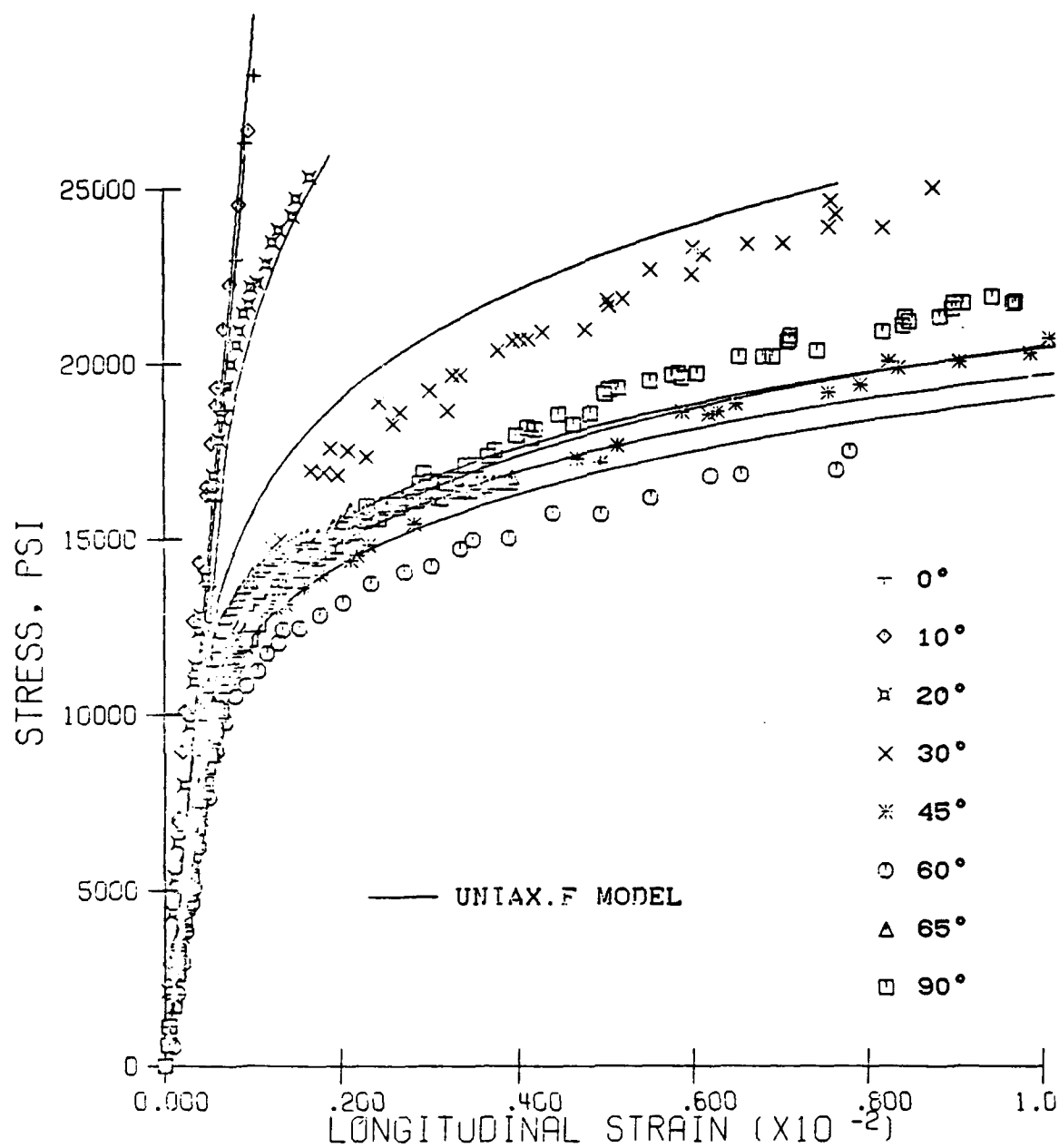


Figure 24. Stress versus longitudinal strain for various fiber orientations. (Same data as in Figure 23 shown on an expanded scale.)

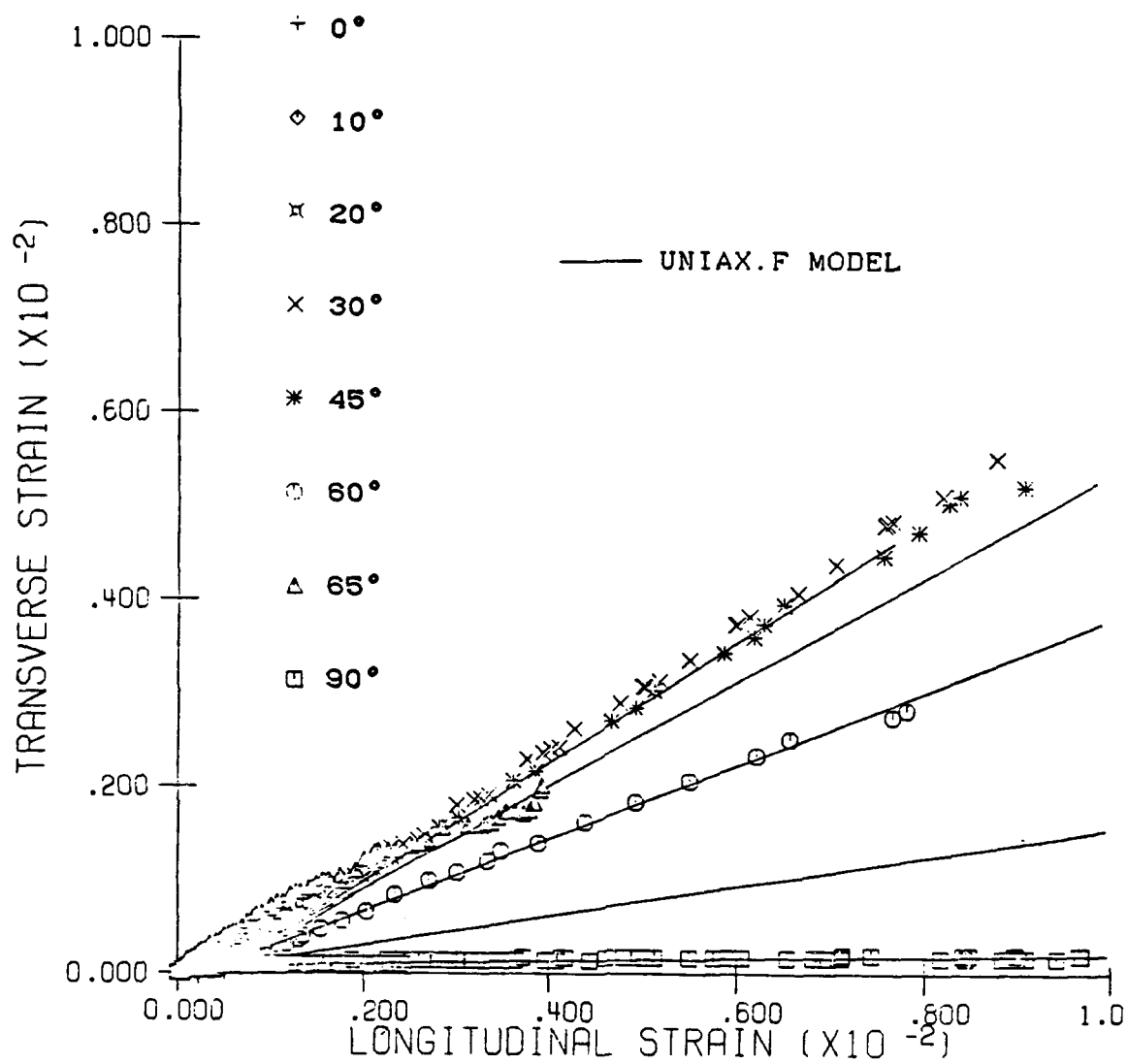


Figure 25. Transverse versus longitudinal strain for various fiber orientations. The solid lines indicate the computer modeling of the experimental data.



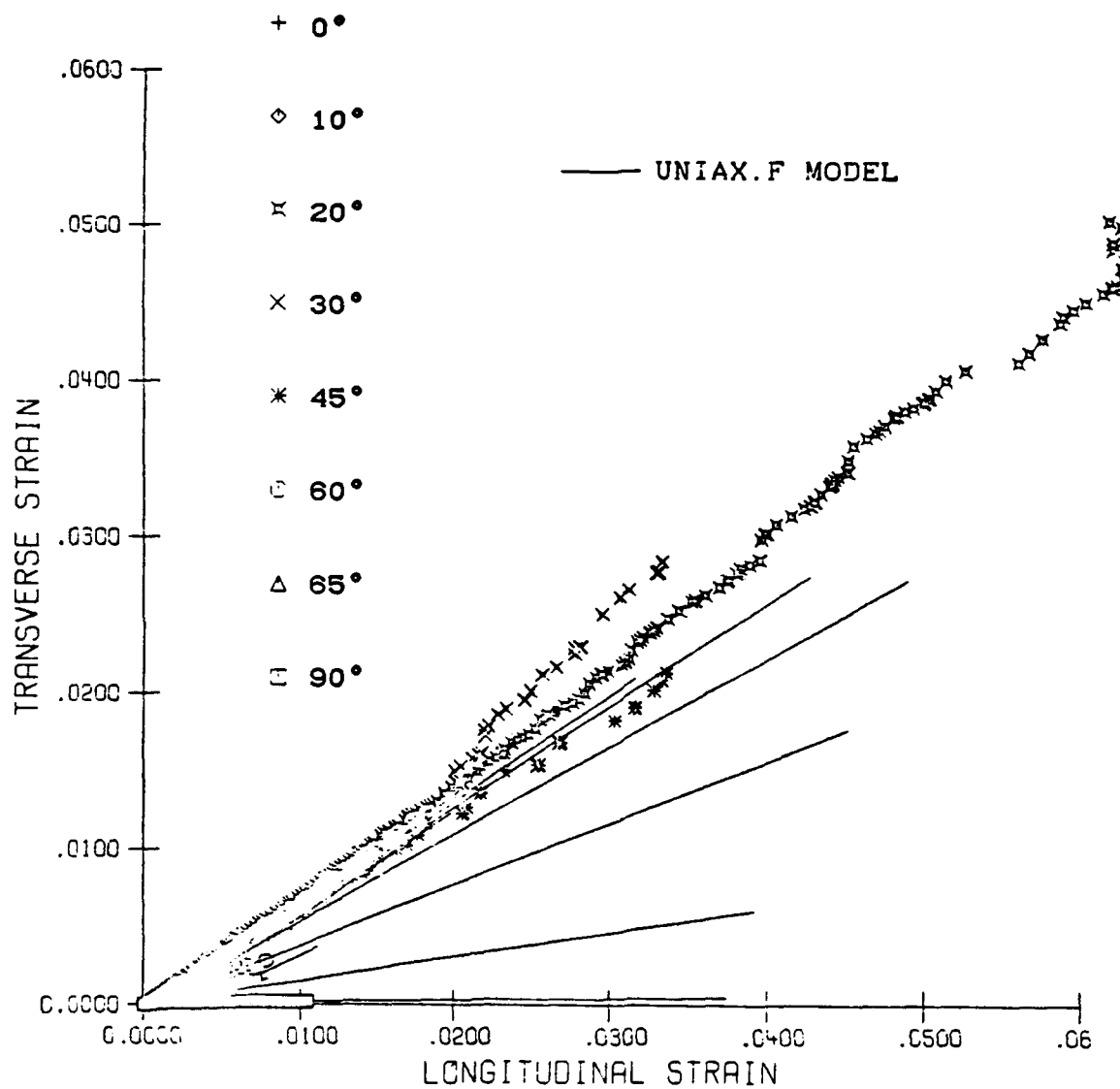


Figure 26. Transverse versus longitudinal strain for various fiber orientations. (Same data as in Figure 25 shown on an expanded scale.)

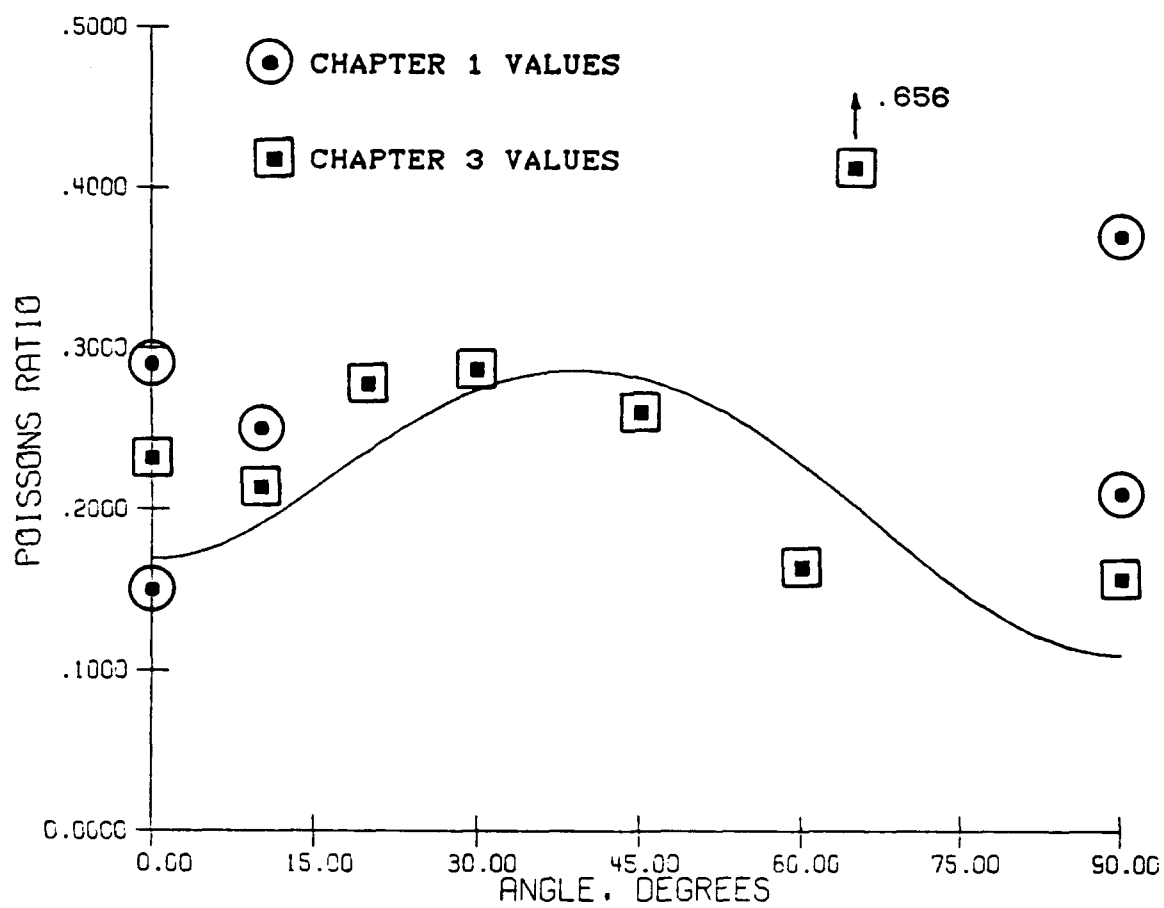


Figure 27. Elastic Poisson's ratio data versus fiber angle. The solid line is the curve-fit for determining the s-values.

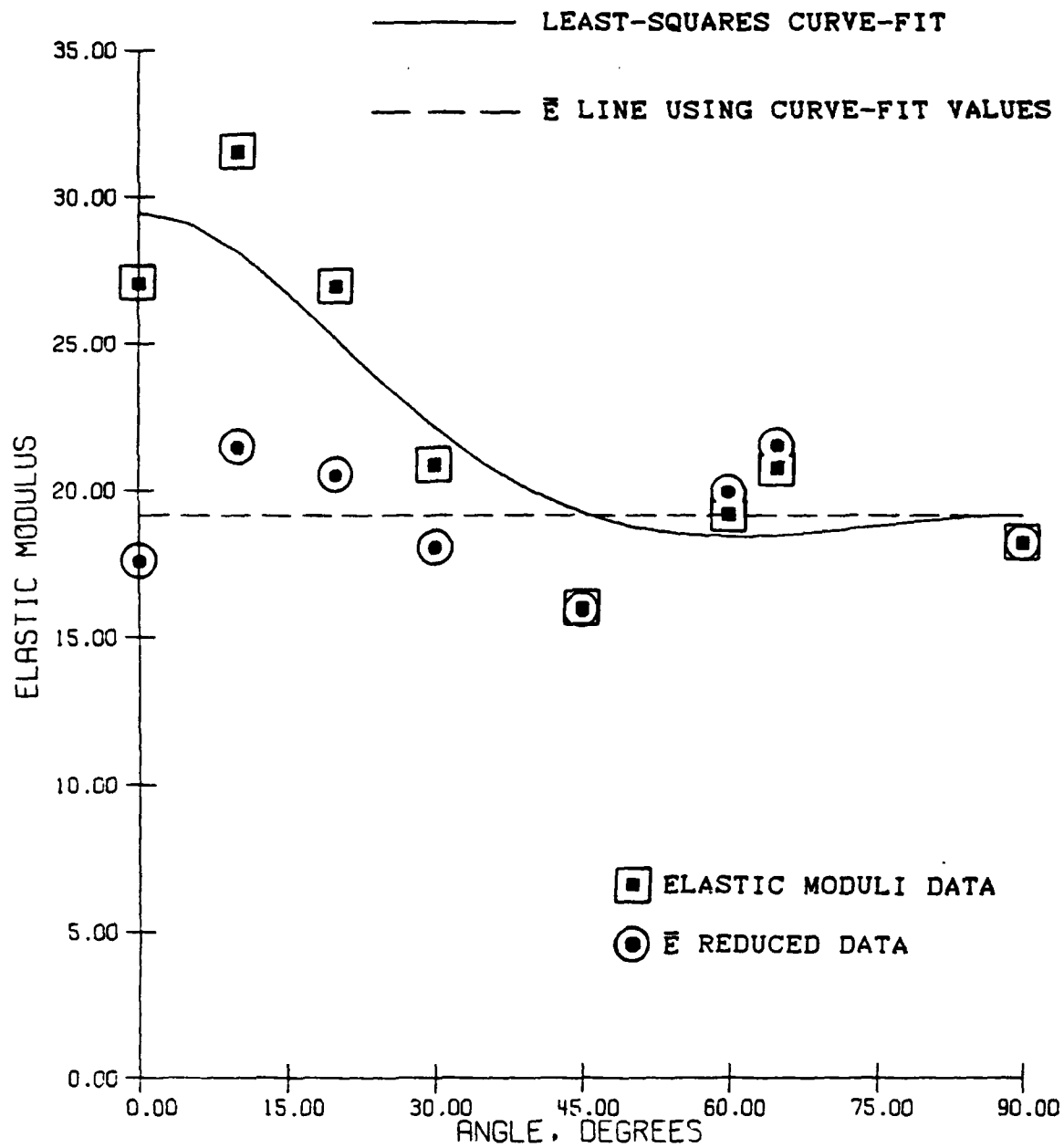


Figure 28. Elastic modulus versus fiber angle. The solid line is a least-squares curve-fit. The dashed line is the effective elastic modulus vs. fiber angle computed from the solid line curve-fit.

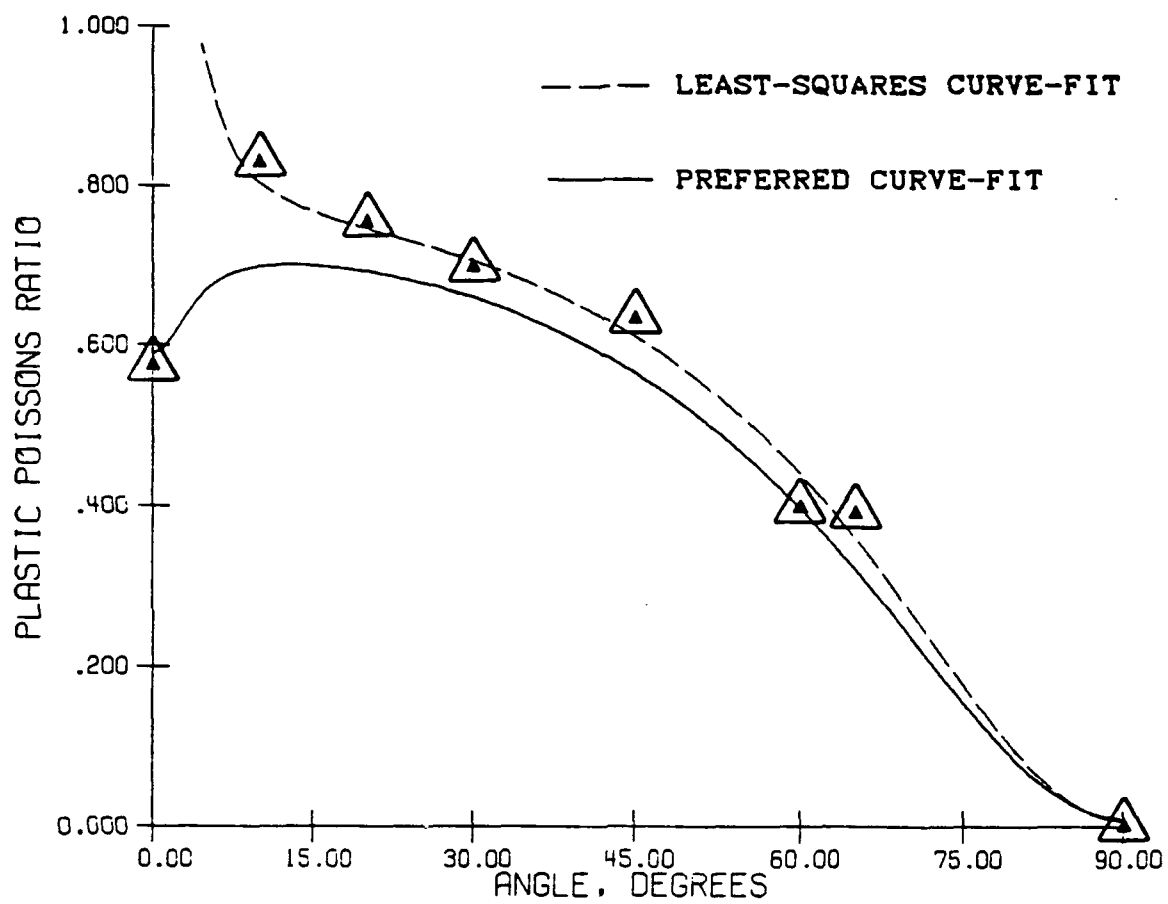


Figure 29. Plastic Poisson's ratio versus fiber angle. The dashed line is for the least-squares curve-fit. The solid line is the preferred curve-fit.

# EFFECTIVE STRESS-STRAIN FROM LEAST-SQUARES CURVE-FIT

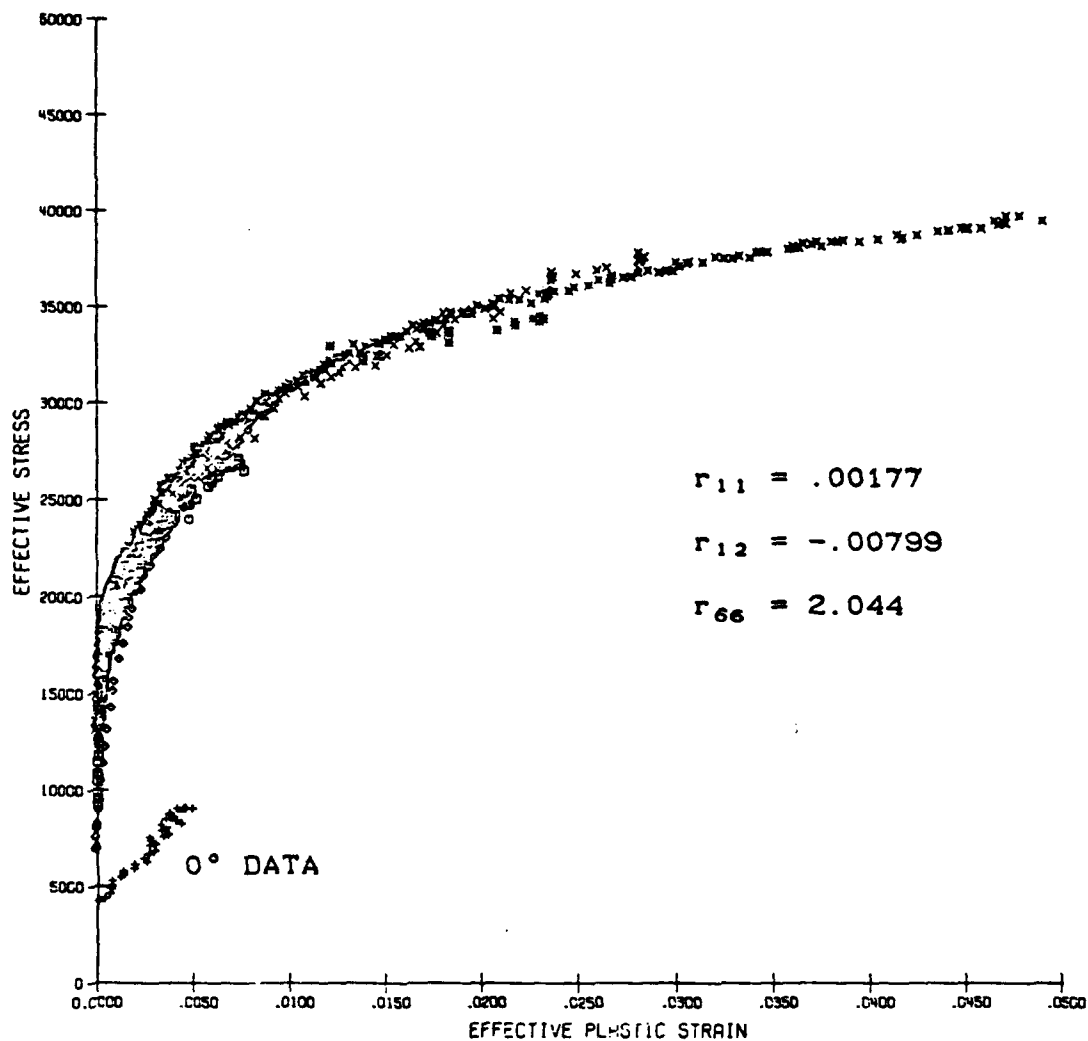


Figure 30. Effective stress versus effective plastic strain for the  $r$ -values found from the least-squares curve-fit. Note that the  $0^\circ$  data is not modeled well.

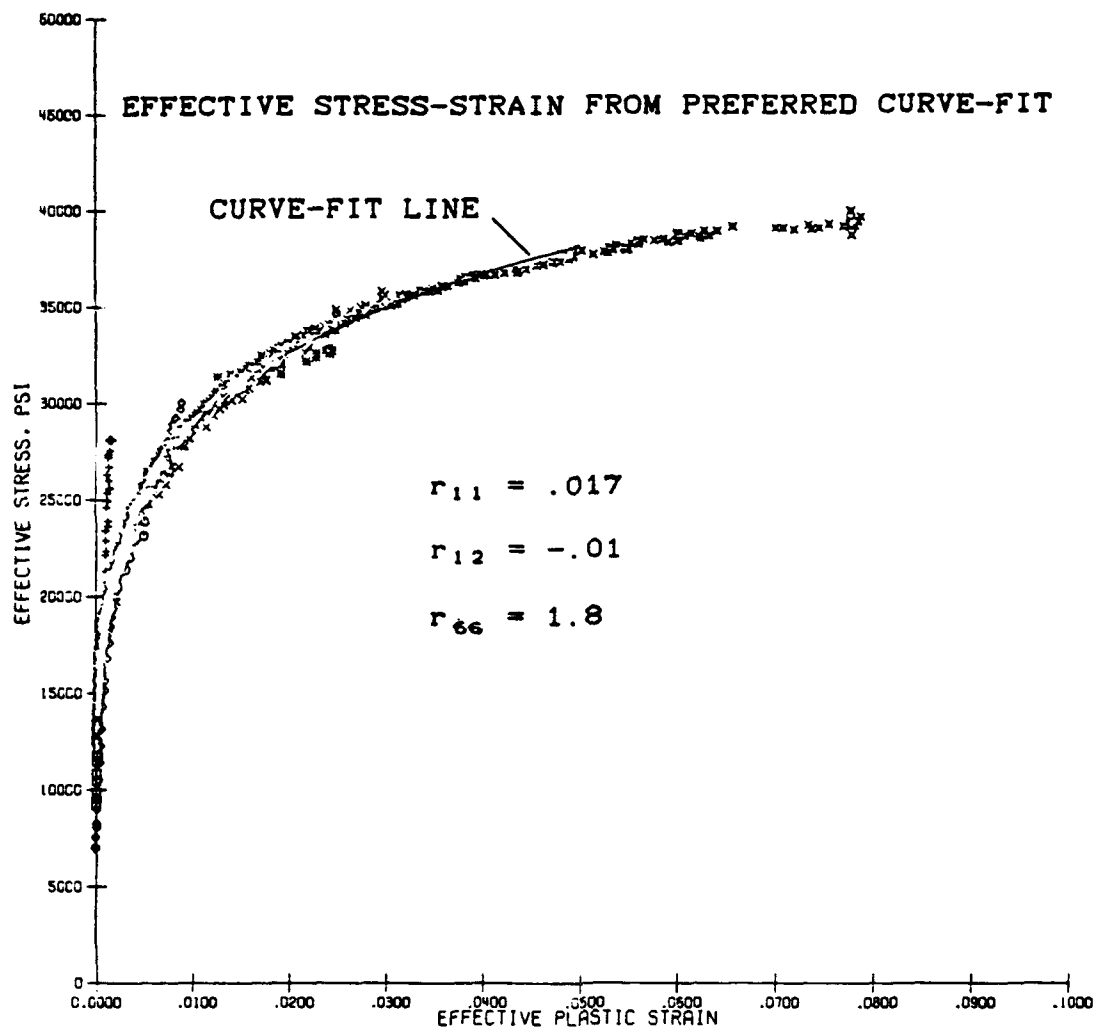


Figure 31. Effective stress versus effective plastic strain for the preferred curve-fit  $r$ -values. The solid line in the modeling curve.

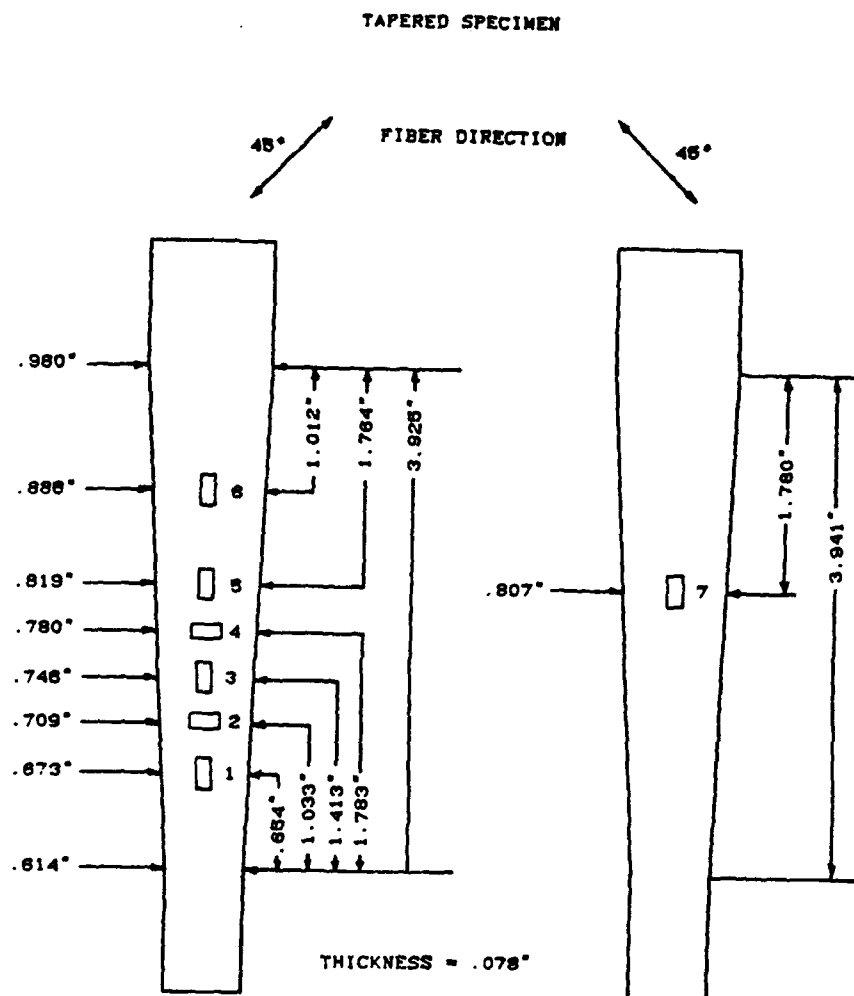


Figure 32. Schematic of the tapered specimen with dimensions and strain gage locations. The specimen was cut using electric discharge machining.

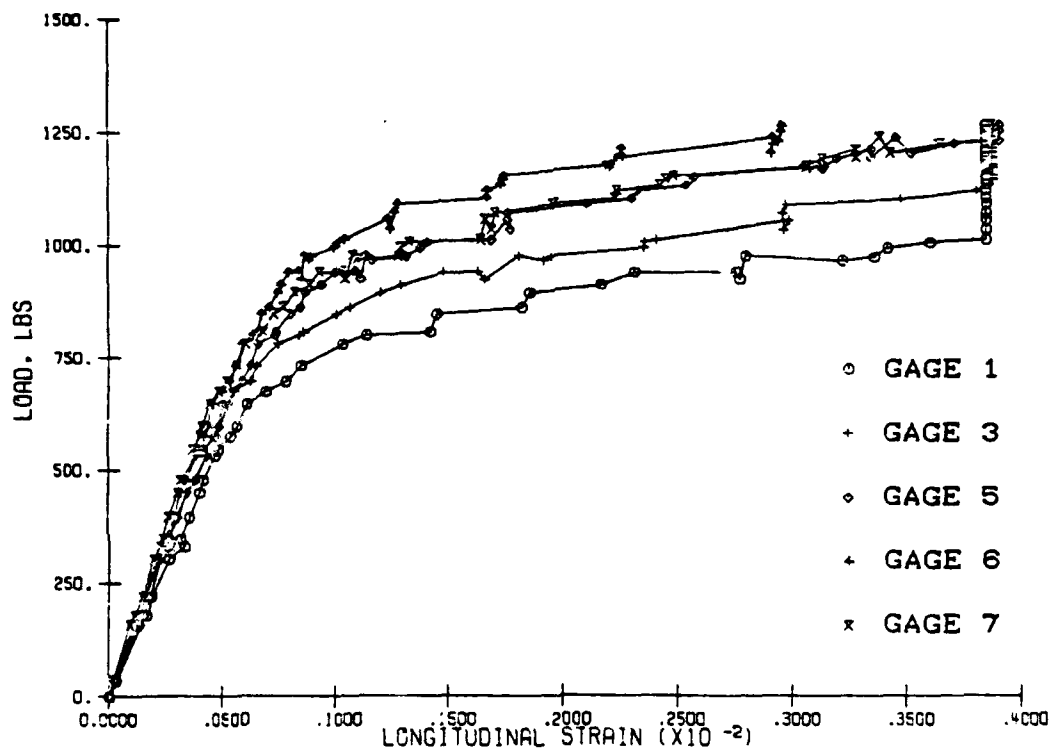


Figure 33. Load versus strain data from the five longitudinal gages of the tapered specimen. The data shows a progression of yielding along the specimen length as the load increases.



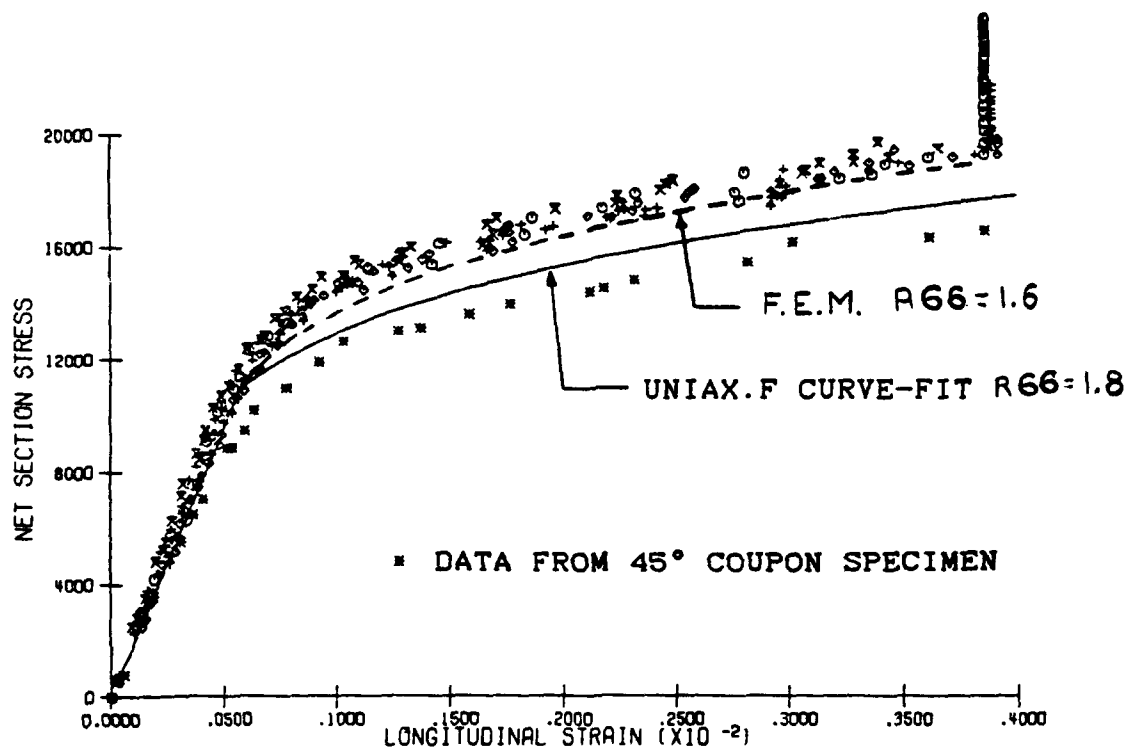


Figure 34. The data presented in Figure 33 is presented here as net section stress versus strain. The data falls nearly along the same line. Data from the 45° coupon specimen and finite element modeling is included for comparison.

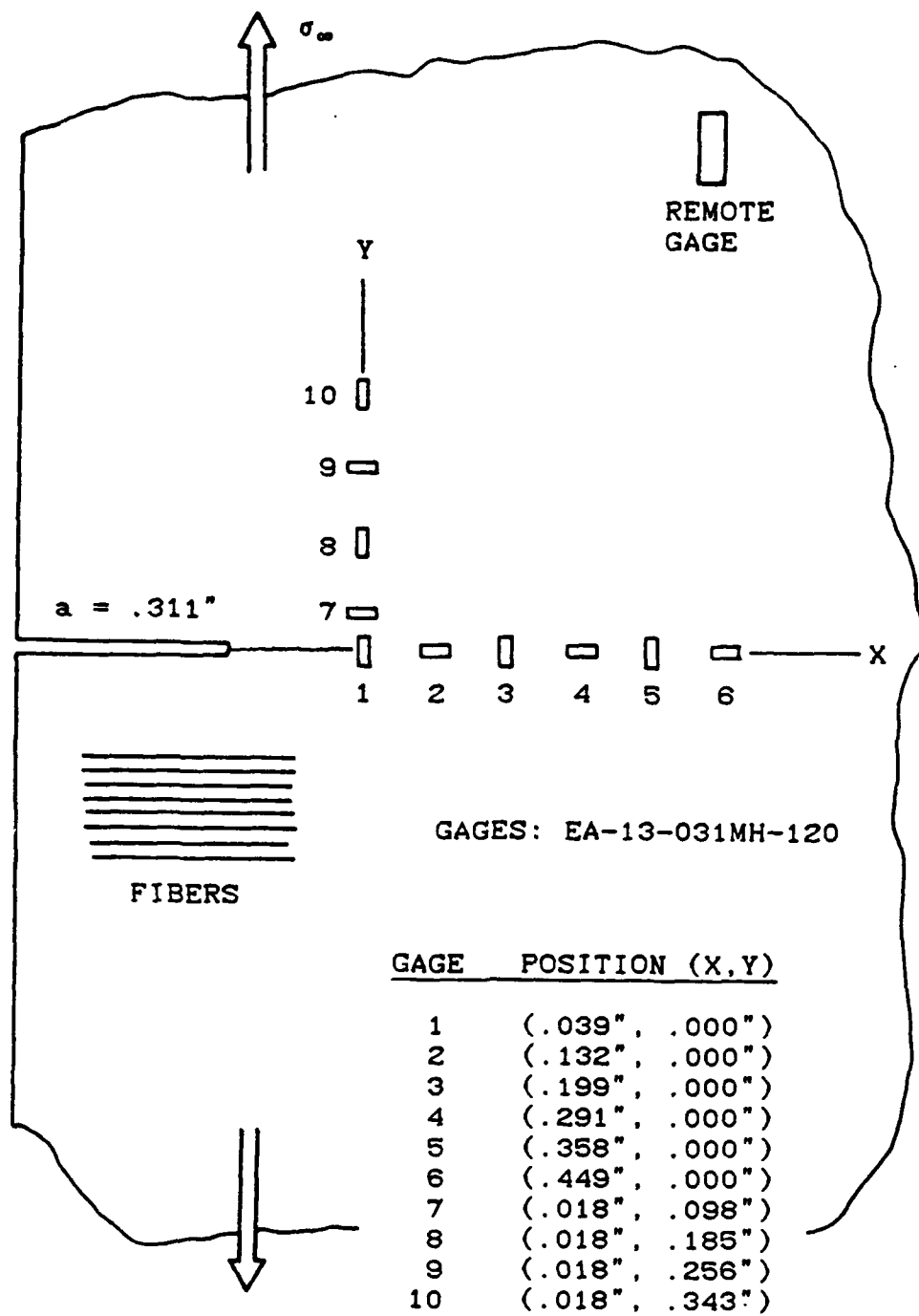


Figure 35. Schematic of specimen 26 for the transverse crack study. The strain gage strip was cut into two sections and positioned as shown.

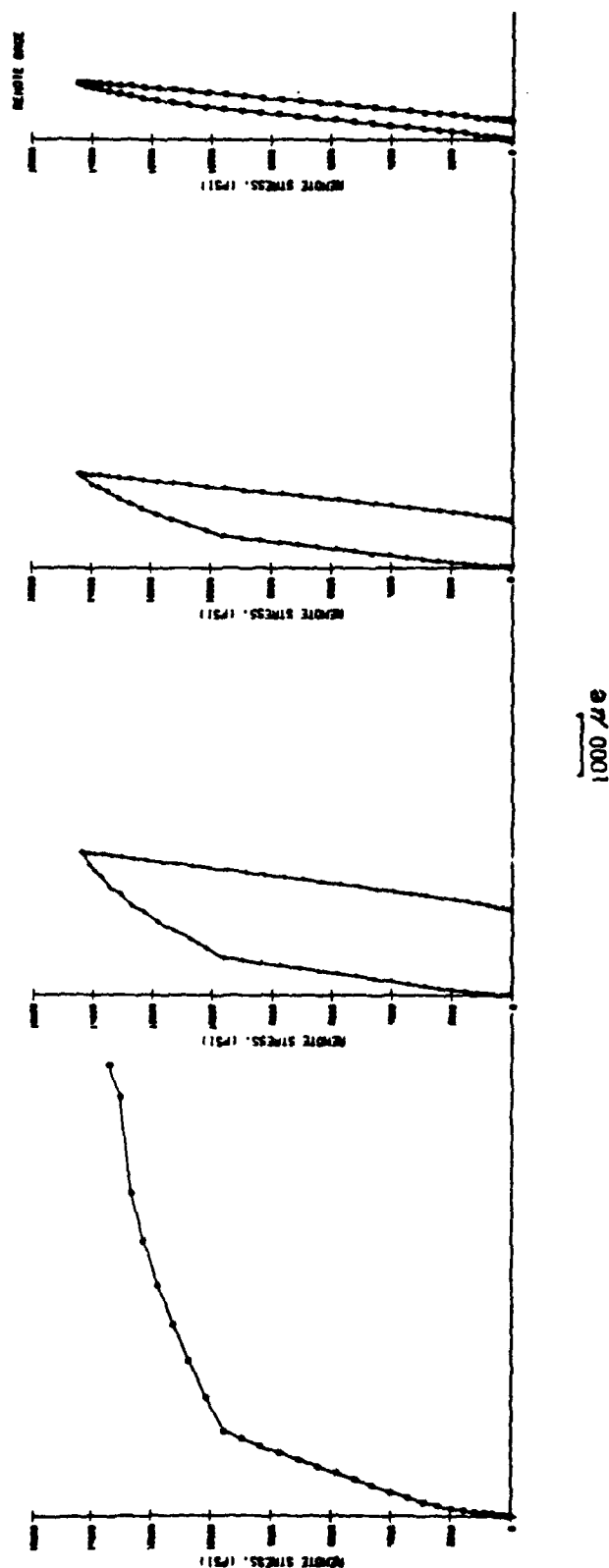


Figure 36. The data from gages 1, 3, 5, and the remote gage of specimen 26 is presented to emphasize the strain distribution at the crack tip. The data was taken during the 1.5 overload cycle. Note that gages 1, 3, and 5 appear to show yielding all at the same stress level. This indicates that the previous loading had yielded the material at each gage location.

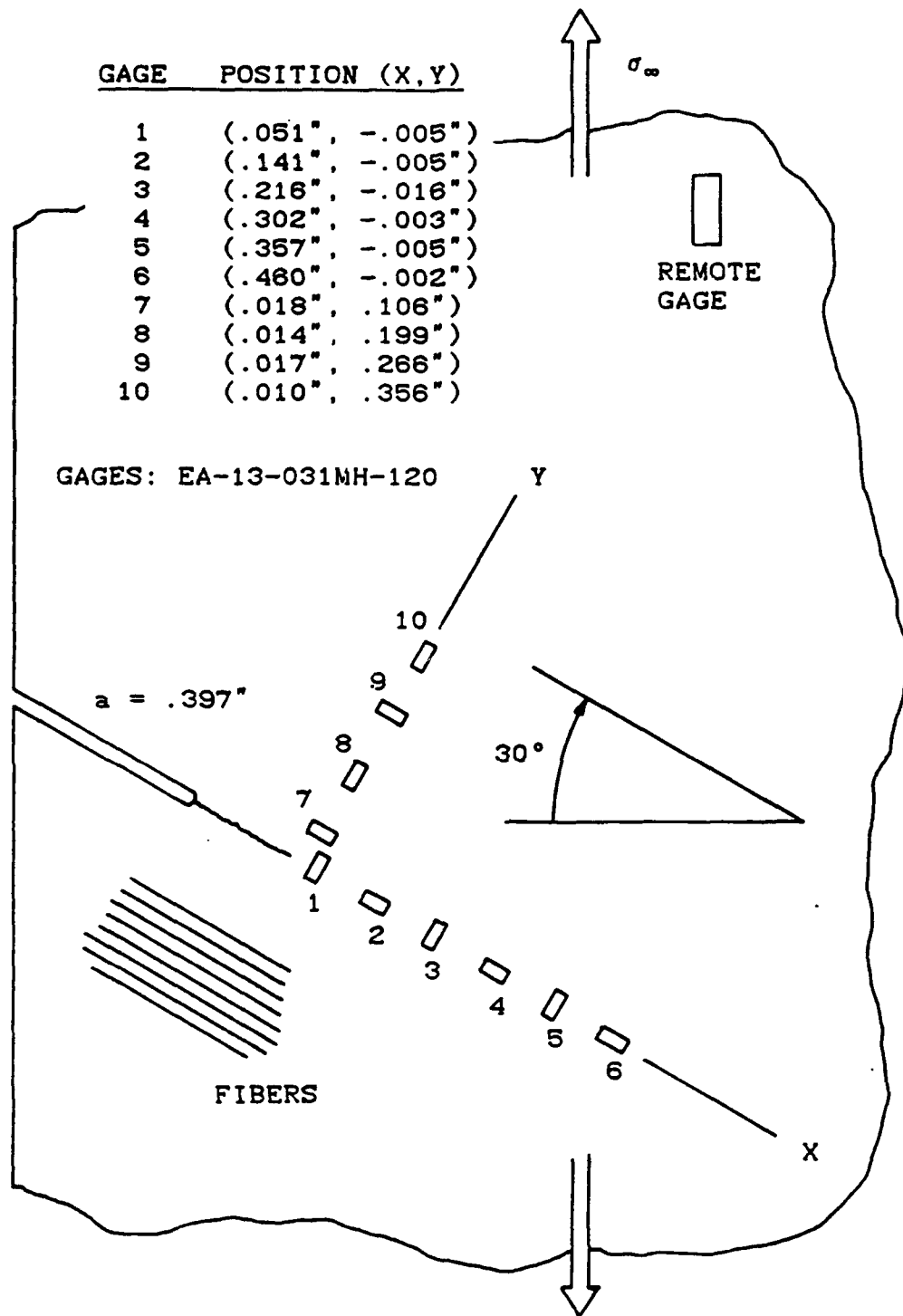


Figure 37. Schematic of specimen 27 for the oblique crack study. The strain gage strip was cut into two sections and positioned as shown

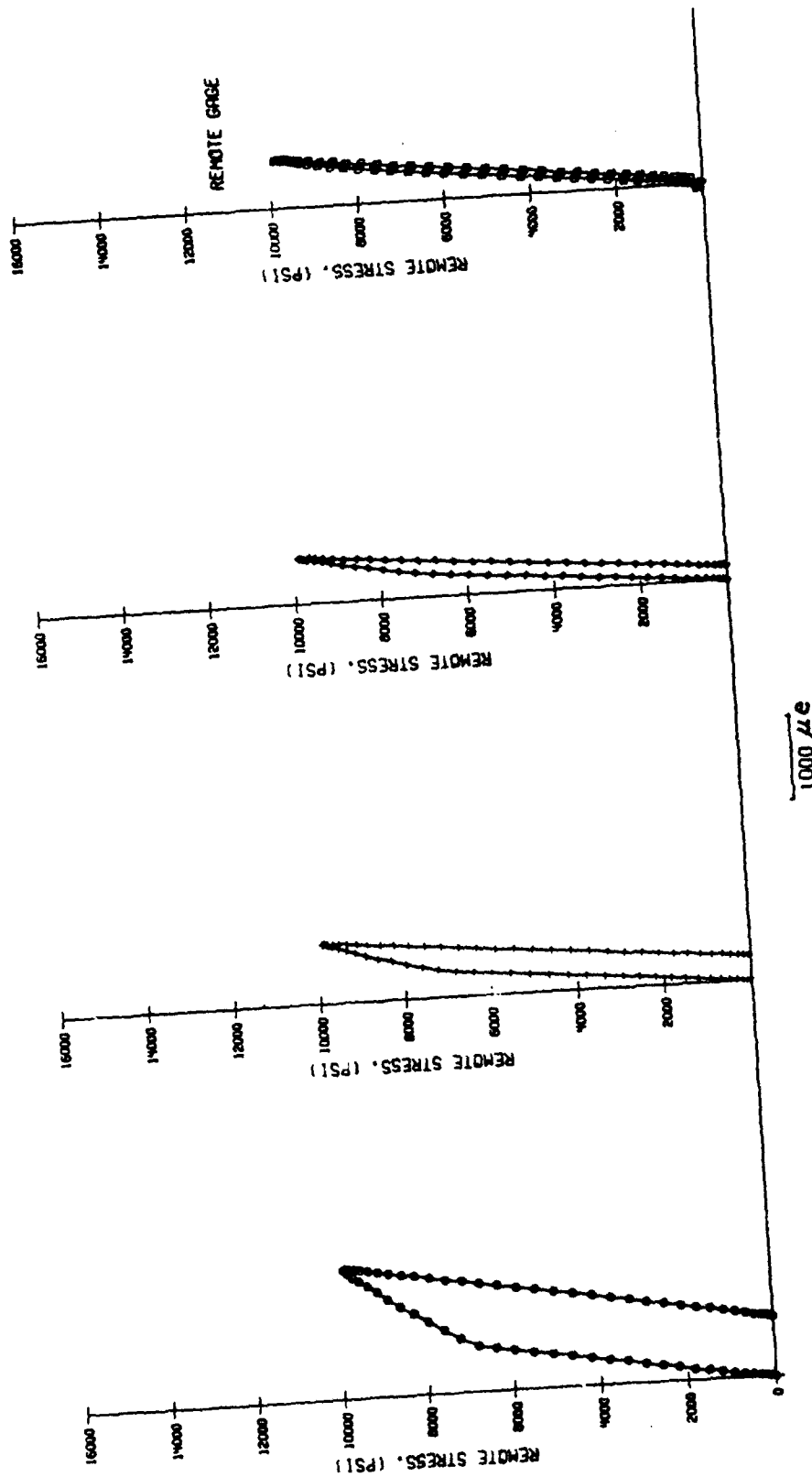
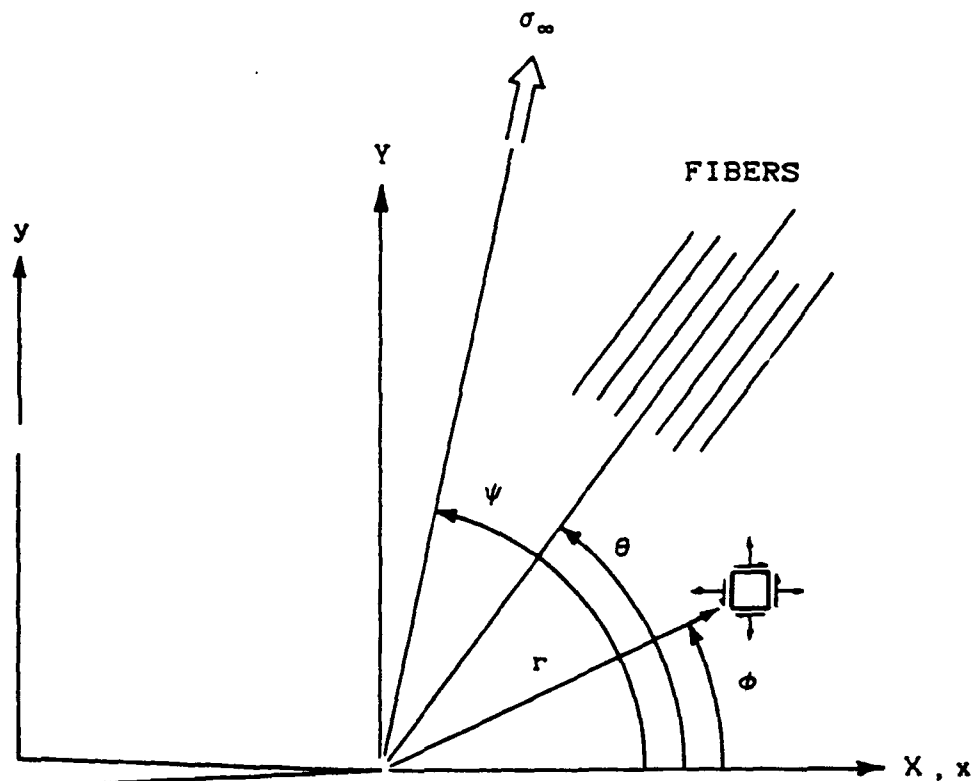


Figure 38. The data from gages 1, 3, 5, and the remote gage of specimen 27 is presented to emphasize the strain distribution at the crack tip. The data was taken during the 1.5 overload cycle. Note that the gages appear to show yielding at different load levels. This indicates that the gages have recorded an increase of the plastic zone size during the 1.5 overload.



$a$  = CRACK LENGTH

$\psi$  = LOAD ANGLE

$\theta$  =  $\parallel$  MATERIAL DIRECTION

$\phi$  = GAGE LOCATION ANGLE

$r$  = GAGE DISTANCE FROM CRACK

Figure 39. Global coordinates convention for the study of cracks in Chapter 4.

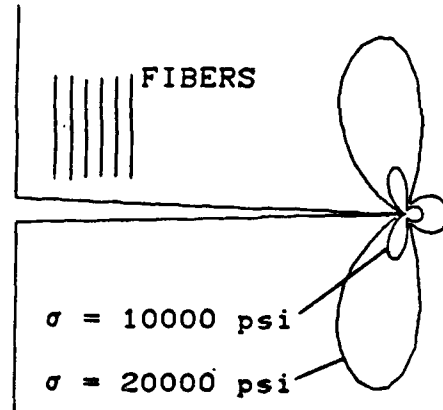


Figure 40. Plastic zone shape at the crack tip generated with ELLPLAS.F program. Fibers are perpendicular to the crack, and loading is as shown. The crack length is .31" (crack shown not to scale with plastic zones)

SCALE: 3x LIFE SIZE

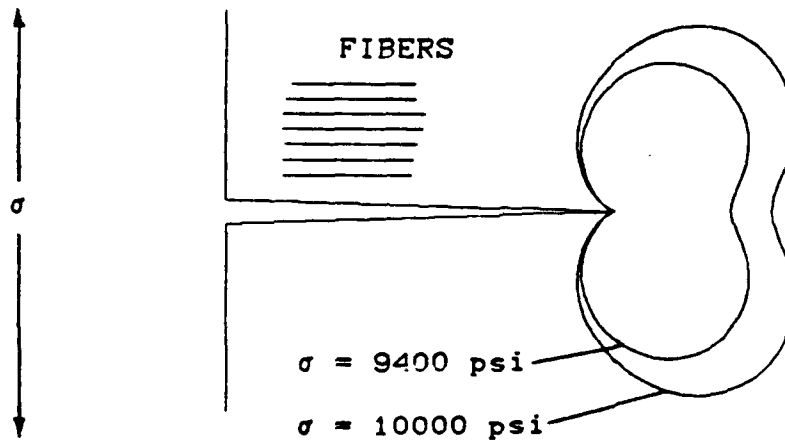


Figure 41. Plastic zone shape at the crack tip generated with ELLPLAS.F program. The fibers are parallel to the crack, and loading is as shown. The crack length is .31" (crack shown not to scale with plastic zones)

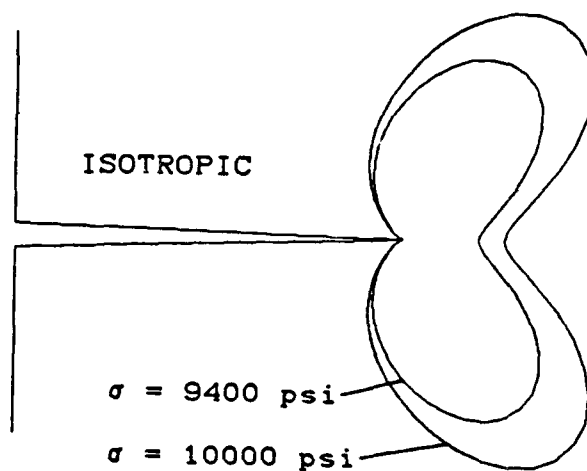


Figure 42. Plastic zone shape at the crack tip generated with ELLPLAS.F program for an isotropic material. The crack length is .31" (crack shown not to scale with plastic zones).



SCALE: 2x LIFE SIZE

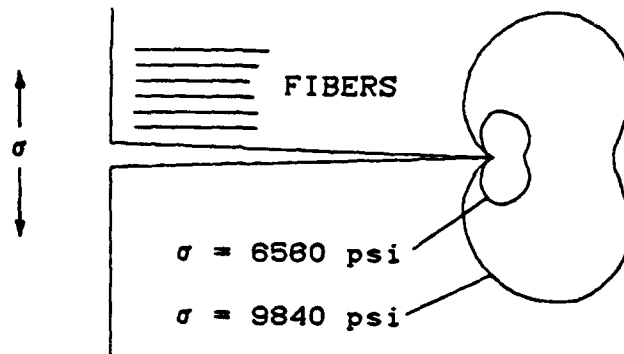


Figure 43. Plastic zone shape at the crack tip generated with ELLPLAS.F program for fibers parallel to the crack and load angle at  $90^\circ$ . This figure is similar in nature to Figure 41. The crack length is .39" (crack shown no to scale with plastic zones)

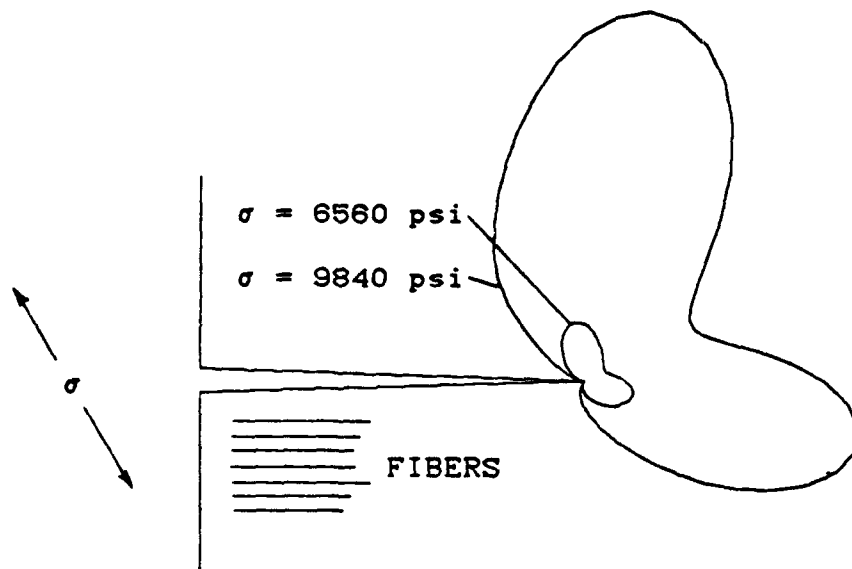


Figure 44. Plastic zone shape at the crack tip generated with ELLPLAS.F program. The fibers are parallel to the crack with the load angle at  $120^\circ$ . The crack length is .39" (crack shown not to scale with plastic zones). This crack geometry and loading is similar to that of specimen 27

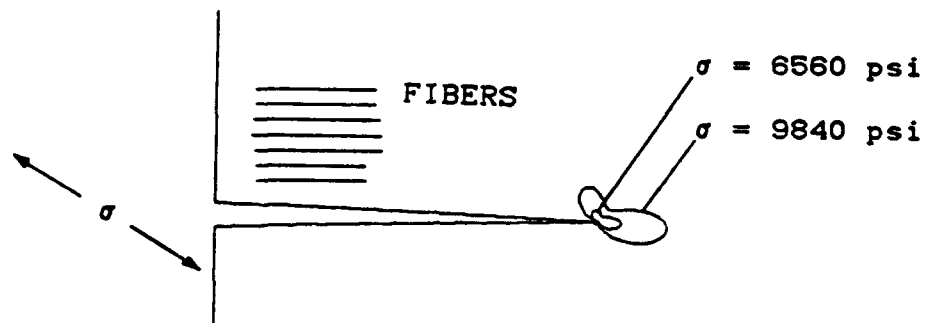


Figure 45. Plastic zone shape at the crack tip generated with ELLPLAS.F program. The fibers are parallel to the crack with the load angle at  $150^\circ$ . The crack length is .39" (crack shown not to scale with plastic zones).

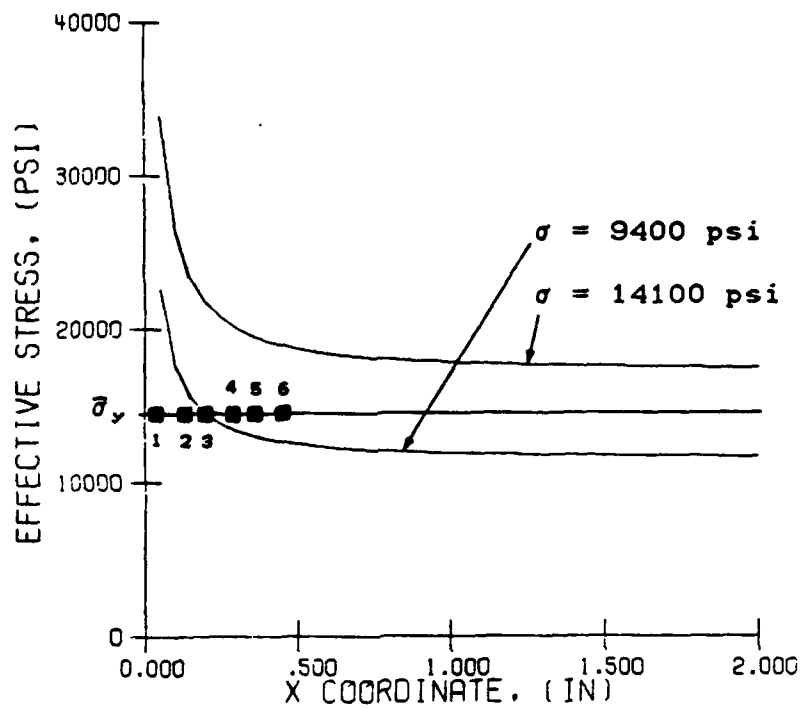


Figure 46. Effective stress along the X-axis for specimen 26. Note that the plastic zone boundary is determined by where the plot crosses the effective yield line. The gage locations along the axis are as shown.

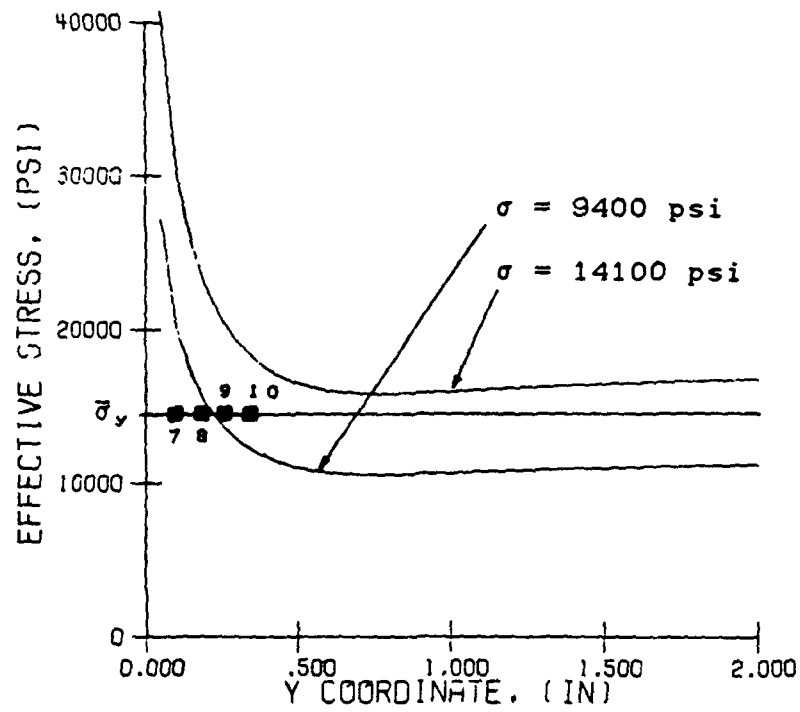


Figure 47. Effective stress along the Y-axis for specimen 26. Note that the plastic zone boundary is determined by where the plot crosses the effective yield line. The gage locations along the axis are as shown.

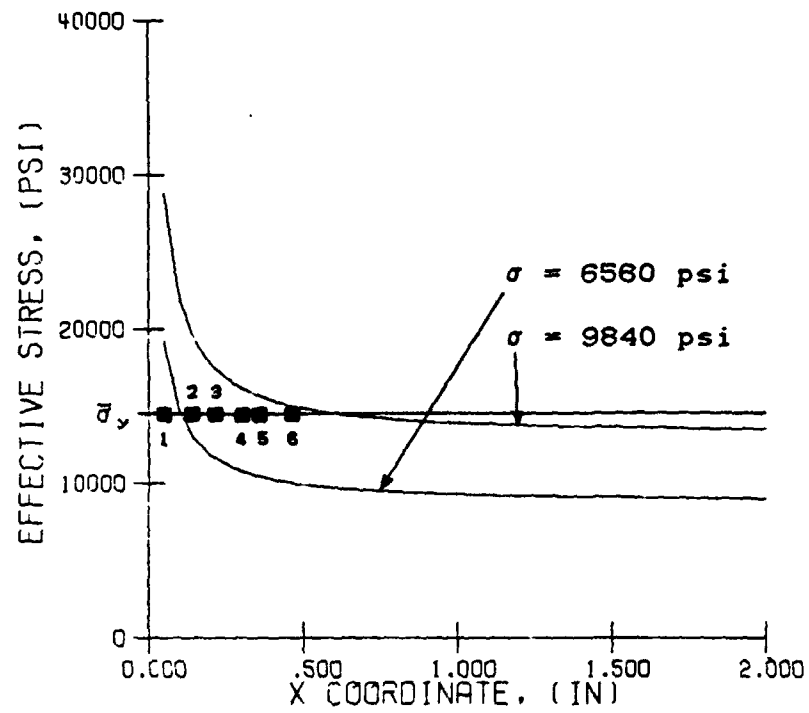


Figure 48. Effective stress along the X-axis for specimen 27. Note that the plastic zone boundary is determined by where the plot crosses the effective yield line. The gage locations along the axis are as shown.

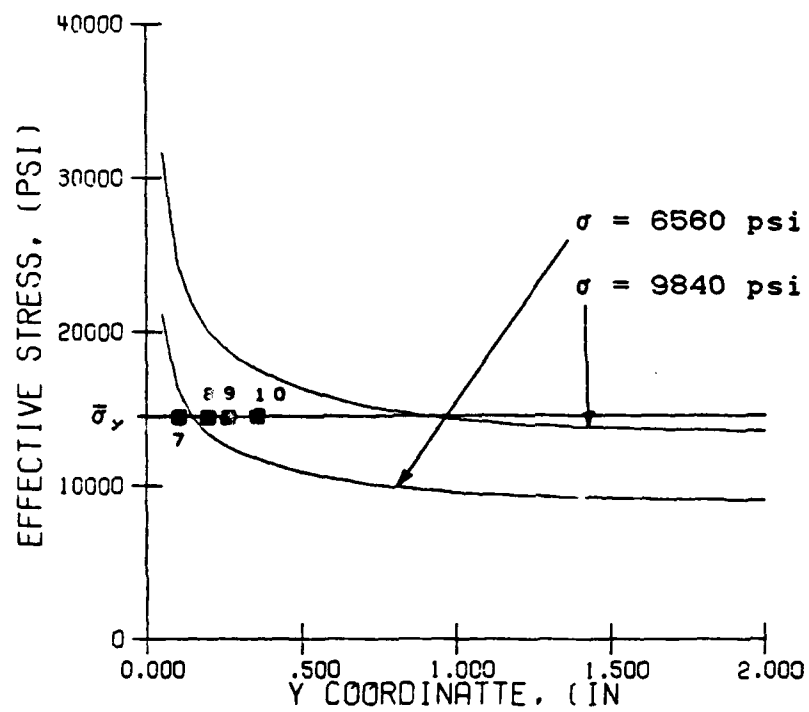


Figure 49. Effective stress along the Y-axis for specimen 27. Note that the plastic zone boundary is determined by where the plot crosses the effective yield line. The gage locations along the axis are as shown.